Atmospheric Trace Gases as Probes of Chemistry and Dynamics

Thesis by

King-Fai Li

In Partial Fulfillment of the Requirements for the
degree of
Doctor of Philosophy

CALIFORNIA INSTITUTE OF TECHNOLOGY
Pasadena, California
2013
(Defended August 2nd, 2012)

DEDICATION

To my parents,
who always give me their everything,

and

To my loving wife, Rachel,
who constantly supports me
in who I am and who I am becoming.

ACKNOWLEDGEMENTS

Coming from the last colony of the former British empire in the Far East, the cultural shock that I received from the very first day that I stepped onto the New World as a summer intern in 2003 was enormous, partly because Hong Kong was just out of the haze of the Severe Acute Respiratory Syndrome (SARS) and the economic crisis that followed (as well as the false threat of SARS on my flight to Los Angeles) and partly because that was my first time leaving home or even Hong Kong for more than 4 days. In addition, I arrived at Caltech on Sunday and the next Monday was the Memorial Day holiday, when there were no administrative staff to help me get settled. Luckily, my advisor, Prof. Yuk L. Yung, and his group worked hard enough during holidays and received me warmly in the office. (Thanks Dr. R.-L. Shia for opening the door for me that afternoon.) New faces, foreign language, different manner and etiquette… There was just too much for me to adapt to in a short time. Thanks Derek Kong, who was my high school classmate in Hong Kong and lived in Monterey Park then, for receiving me that evening and providing me some survival skills (although he went back to Hong Kong after the first week). I arrived one month ahead of the other two classmates from the Chinese University of Hong Kong (CUHK) coming to Caltech for summer internships, and was probably the one who suffered the most but learned and was rewarded the most from the internship. Without a personal laptop, my homesickness was so serious that I made phone calls to my former advisor, Prof. M.-C. Chu, in the first few days and begged for home very childishly. My homesickness was greatly relieved by hiking with Prof. Yung over weekends and with the help of Prof. Yung’s group, Joshua Cheng, Sonia Yan, Ting-Hei Liao, Pak-Ying Cheng (her laptop was brought to me by Steven, one of the CUHK students), and Rachel, my significant other, over the telephone. That summer I wrote my first academic paper, which was published in *Li et al.* [2005].

I came back as a graduate student in the summer of 2006 and continued my undergraduate work with Prof. Yung. I had never imagined how quickly six years could pass. The amount of work was tremendous and the schedule was insanely tight. Impacted by failures in examinations and paper publications, I started to learn how to compromise and grew up. I once wanted to give up after the first year of the graduate study, or even the first three months, when my mother suffered a stroke and was hospitalized. I am greatly indebted to Prof. Yung, who encouraged me to proceed by bravely facing the difficulties and developing mental hardness and improving my weaknesses over my study. Prof. Yung was not only my advisor, but he was also my greatest teacher for life. The fact that we both grew up in Hong Kong had provided us common ground for personal interactions.

These six years were also the fastest growing period of some Asian countries (e.g., China, Singapore, Vietnam, etc.) in history, despite the global economic crisis in late 2000s. Every time I went back to Hong Kong for vacation, I was stunned by how much the local economy and the lifestyle had been influenced, both positively and negatively. However, the hard lives of my parents and other family members, who seemingly had not benefited from the regional economic growth, always struck my mind and led me to blame myself for leaving home for abroad. Only the encouragement from Rachel and my colleagues as well as the joy of research provided me enough motivation to finish my long-awaited PhD thesis. There are too many people to acknowledge. Besides Prof. Yung, I especially want to give my heartiest thanks to Prof. Duane E. Waliser, Dr. Run-Lie Shia, Dr. Baijun Tian, Dr. Shuhui Wang, Dr. Sally Newman, and Prof. Kenneth Young (former advisor at CUHK), who gave advice on non-academic subjects or personal matters. I want to thank my collaborators, including Prof. Xun Jiang, Dr. Mao-Chang Liang, Dr. Stanley P. Sander, Dr. Jack Margolis, Prof. Joseph Kirschvink, and Dr. Xianan Jiang, who strengthened my research background and provided guidance on my research projects. I must thank Dr. Franklin P. Mills at the Australian National University for hosting me during a three-month visit there and Prof. Ka-Kit Tung for hosting my upcoming Jack Eddy Postdoctoral Fellowship. I also want to thank all group members, including Le Kuai, Xi Zhang, Michael R. Line, and Ross Cheung, as well as all of the summer students that I have worked with.

Six years may be just a short period of time in my life. But for my parents and beloved in Hong Kong, I selfishly asked them to invest these six long years in allowing me to fulfill my own aspirations. I have nothing and do not know how best to reward them for their most treasured trust in me. This glory will be shared with my parents and Rachel, my wife, who sacrificed greatly and helped take care of my parents in Hong Kong during my absence (and who also made a call to a phone-in radio program in Hong Kong and comforted me on the overseas airwaves).

ABSTRACT

This dissertation is a collection of empirical and modeling studies focusing on decadal and intraseasonal variabilities in atmospheric tracers. In Part I, a persistent discrepancy between the model and observed stratospheric O_3 solar response is revisited using the Whole-Atmosphere Community Chemistry Model (WACCM). The model O_3 simulated using UV irradiances measured from the latest spaceborne solar UV measurements by the Solar Radiation and Climate Experiment (SORCE) and that from the solar UV parametrization developed by the Naval Research Laboratory (NRL) are studied and compared with observations. None of the simulations using SORCE and NRL UV simultaneously agree with the observed O_3 solar response in both upper and lower stratospheres, thus presenting a dilemma to our current understanding of stratospheric O_3 response to UV perturbations. However, the simulation using the SORCE UV irradiance leads to a solar response in upper stratospheric/lower mesospheric OH column that agrees better than those derived from ground-based and satellite observations. Continuous long-term observations of solar UV, OH, $O_{3,}$ and other related chemical species through upcoming solar cycles are crucial for further investigations to solve the above puzzles. In Part II, intraseasonal variabilities in upper tropospheric/lower stratospheric (UTLS) O_3 and mid-tropospheric carbon dioxide (CO_2) related to the Madden-Julian oscillation (MJO) are studied using recent satellite observations. The UTLS O_3 at mid-latitudes is shown to be modulated by the MJO through dynamical motions of the tropopause layer, supporting the conjecture proposed in previous studies. It is further shown that the UTLS O_3 over the Arctic can be also modulated by the tropopause motions through MJO teleconnections. On the other hand, the distribution of tropical mid-tropospheric CO_2 is modulated by the MJO through upward transport of surface CO_2. The amplitude is of critical scale for identifying oceanic and land sources of CO_2. The detailed structures of these MJO impacts are useful for diagnosing chemical transport models. These findings may be useful for improving air quality forecasts to weekly/monthly timescales, which help warn the public in advance and help authorities to take efficient emergency control actions.

Table of Contents

PART II. INTRASEASANOL VARIABILITY

List of Figures

List of Tables

PREFACE

During my six years in Caltech's graduate school, I had broad interests in atmospheric chemistry, dynamics, and radiative transfer, as well as astrobiology. I was also involved in data analyses using advanced statistical methods and inversion theory. Most of my studies aim to better characterize multiscale atmospheric processes in time and space using observational datasets and chemistry/climate models. In this thesis, I chose five publications which illustrate two examples on the use of atmospheric tracers for climate studies, one on decadal time scales and the other on intraseasonal time scales.

Atmospheric Trace Gases as Probes

The general circulation of the atmosphere embraces the properties of atmospheric disturbances of every scale, which are integrated to provide a description of the atmospheric evolution, within the framework of a given spatial and temporal distribution of solar energy input. It is an enormous multidisciplinary problem of chemistry, physics, radiation, and, to some extent, biology and ecology. Tremendous progress has been made since the satellite era in the 1970s in obtaining a broad and detailed description of the atmosphere through temporally and spatially highly resolved observations. Theory has also advanced with these observations and can demonstrate the necessity of certain mean features arising from a field of multiscale processes and turbulence. However, we are still far from possessing a thorough empirical description of some of its more elusive features (e.g., convection), and much less an understanding or theory that is capable of demonstrating the necessity of its detailed structure and evolution.

The general circulation can be most directly derived from real-time observations or assimilations of global wind and temperature. However, to reveal the underlying mechanisms of how the atmosphere or part of it works, the paths of some atmospheric tracers and/or the changes of their physical and chemical properties are needed to fully unveil the interactions and/or feedbacks between one part and another or between one scale of motion and another [*Sheppard*, 1963]. Examples of tracers that have been used for monitoring atmospheric chemistry, atmospheric dynamics, and surface processes include H_2O, O_3, CH_4, CO, CO_2, N_2O, and SF_6. Because each tracer has its own characteristic sources/sinks and atmospheric lifetimes, information of its distribution in different parts of the atmosphere provides useful constraints for diagnosis of model shortcomings.

In this thesis, O_3 is a key species that will be used for studying two vastly different processes: decadal variability related to the solar forcing using the photochemical nature of stratospheric O_3 (Chapter 2) and intraseasonal variability related to the Madden-Julian oscillation in tropical convection using the dynamical nature of upper tropospheric/lower stratospheric O_3 (Chapter 5 and 6). Note that, depending on the processes being investigated, stratospheric O_3 can be short-lived if considered on the decadal time scales, but it can be long-lived, if considered on intraseasonal time scales. This fact greatly facilitates O_3 as an important species that can serve as a probe for both processes. Two other species, the stratospheric hydroxyl radical (OH) and mid-tropospheric CO_2, will also be studied, as described below.

The Solar Forcing

Following the restrictions of chlorofluorocarbons in the mid-1990s, the global stratospheric O_3 level is slowly recovering. The current estimate of the time for full recovery is expected in 50 years or more [*Newman et al.*, 2006], but an accurate forecast of the long-term trends critically depends on our knowledge of O_3 variability and its interactions with external forcings. Observationally, to quantify subtle secular trends in O_3, it is critical to understand natural variabilities that may have similar magnitudes and interfere with the trends [*Salby et al.*, 2011]. In this thesis, the influence of the 11-year solar cycle on stratospheric O_3 will be examined in a three-dimensional chemistry-dynamics-radiation coupled model. The model results will be compared with recent observations. Previous studies [e.g., *Kodera and Kuroda*, 2002] have shown that, besides the well-known O_3 photochemistry, nonlinear dynamical feedbacks in meridional stratospheric circulation must also be considered to qualitatively explain the observed vertical O_3 solar response. Nonetheless, there are still persistent discrepancies between the model and observed O_3 solar response, despite twenty years of effort (Chapter 1). One such discrepancy will be revisited in this thesis with updated exoatmospheric solar irradiance recently acquired from satellite observations (Chapter 2). This helps clarify the role of radiation in the O_3 solar response.

The persistent discrepancies may also be a combination of our incomplete knowledge in photochemistry and/or dynamical feedbacks. To simplify the problem, the upper stratosphere, where photochemical equilibrium dominates, will be specifically examined. The solar response of OH, a key O_3-destroying catalyst in that region, will be studied using state-of-the-art ground-based/satellite measurements and chemistry models (Chapter 3).

The Madden-Julian Oscillation

Tropical convection is one of the key variables in weather prediction. Recent satellite observations and modeling studies have advanced our knowledge of tropical convection, which has greatly improved our ability to forecast extreme weather events (e.g., hurricanes and flooding) on weekly time scales and develop warning systems to reduce economic loss. The Madden-Julian oscillation (MJO) is the dominant mode of the intraseasonal variability in tropical convection. The MJO interacts with a wide range of weather and climate phenomena and represents an important source of predictability at the subseasonal time scale [*Lau and Waliser,* 2011]. However, the MJO is still not well understood or well represented in the global circulation model. Daily space-borne observations allow us to monitor the MJO globally. Influences of the MJO on the physical components of global climate systems are significant and have been well recognized (e.g., monsoons, ENSO, hurricanes, extratropical weather). Nonetheless, the impacts of the MJO on the chemical components of the climate system have only been realized recently and have not been well documented or understood. Observational analyses of the large-scale three-dimensional structure and spatial–temporal evolution of the MJO have proven valuable in addressing this challenge. The goal is to conduct an in-depth study of the modulation by the use of two important greenhouse gases, CO_2 and $O_{3,}$ using global space-borne measurements. This will connect the intraseasonal variability to climate issues and should be of interest to a large group of Earth scientists. Because CO_2 and O_3 have distinctly different distributions in the atmosphere, space-borne measurements are sensitive to these gases at different altitudes. Analyses on these trace gases help reveal the mechanisms of MJO at different levels of the atmosphere, as will be shown in this thesis (Chapters 5, 6, and 7). Furthermore, these findings are useful for improving air quality forecasts on weekly/monthly timescales, helping authorites to issue warnings to the public and to take emergency-control actions in a timely manner.

Thesis Overview

This thesis is divided into two parts: The first part focuses on the solar cycle forcing in stratospheric O_3 and lower mesospheric/upper stratospheric OH; the second part focuses on the impact of the MJO on O_3 and CO_2.

Chapter 1 reviews sun–climate interactions through stratospheric O_3 and describes the model–observation discrepancy, which is the main focus of Part I.

Chapter 2 presents a sensitivity test of model O_3 to exoatmospheric solar irradiance. Using the latest spaceborne measurements of exoatmospheric solar irradiance acquired by the Solar Radiation and Climate Experiment (SORCE), the model total column O_3

response to the 11-year solar cycle is 5.4 Dobson units (DU) per 100 units of 10.7 cm solar radio flux $F_{10.7}$ [*Tapping and Detracey*, 1990] (DU/100$F_{10.7}$) in the tropics, which agrees with the long-term measurements made by the Total Ozone Mapping Spectrometer (TOMS). The vertical O_3 response agrees with previous satellite measurements in the lower stratosphere but disagrees in the upper stratosphere. In contrast, using a well-accepted solar UV irradiance parametrization developed by the Naval Research Laboratory (NRL), the total O_3 column response is 3 DU/100$F_{10.7}$, which agrees better with the SAGE and ground-based observations. The resulting vertical O_3 response agrees with previous satellite measurements in the upper stratosphere, but the lower stratospheric response is much weaker than the observed. This presents a dilemma to our current understanding of stratospheric O_3 response to UV perturbations.

To further elucidate the role of chemistry in the middle atmospheric solar responses, Chapter 3 investigates the solar forcing in lower mesospheric/upper stratospheric OH using ground-based and satellite observations and model simulations. Observations suggest a ~ 7–10% decrease in OH column abundance from solar maximum to solar minimum. However, model simulations using the well-accepted solar irradiance model give much smaller OH variability (~ 3%) whereas the model OH variability derived using the latest spaceborne solar irradiance is ~ 6–7%, which agrees better with observations. Model simulations also reveal the detailed chemical mechanisms, suggesting that such OH variability and the corresponding catalytic chemistry may dominate the O_3 response to solar cycle (SC) in the upper stratosphere.

Chapter 4 reviews the current knowledge of the Madden-Julian oscillation (MJO), which is the main focus of Part II. The mechanism of the MJO is briefly discussed and an index which categorizes the MJO lifecycle into eight phases is introduced.

Chapter 5 examines the vertical structure of MJO-related subtropical O_3 variations using satellite and *in situ* measurements. The spatial-temporal patterns of the subtropical O_3 anomalies throughout the eight MJO phases are presented. The MJO-related O_3 variability are dominant in the lower stratosphere, and are dynamically driven by the vertical movement of subtropical tropopause, supporting the hypothesis of *Tian et al.* [2007]. The strong connection between the intraseasonal subtropical stratospheric O_3 variations and the

MJO implies that the stratospheric O_3 variations may be predictable with similar lead times over the subtropics.

Chapter 6 extends the findings in Chapter 5 from the tropics to the Arctic region. MJO-induced teleconnection is found to moderate O_3 in the Arctic in the upper troposphere/lower stratosphere. The O_3 anomalies are anti-correlated with the geopotential height (GPH) anomalies at 250 hPa, indicating that the O_3 anomalies are associated with dynamical motions near the tropopause, similar to those found in the tropics. This study therefore implies that air quality over the Arctic can also be affected by tropical dynamics through teleconnection.

Chapter 7 reports a large-scale intraseasonal variation in tropical CO_2 associated with the MJO. The peak-to-peak amplitude of the composite MJO modulation is ~ 1 ppmv. The correlation structure between CO_2 and rainfall and vertical velocity indicate positive (negative) anomalies in CO_2 that arise due to upward (downward) large-scale vertical motions in the lower troposphere associated with the MJO. These observations can help elucidate how faster processes can organize, transport, and mix CO_2 and provide a robustness test for coupled carbon-climate models.

PART I.

SUN-CLIMATE INTERACTIONS

Chapter 1.
Review of Sun-Climate Relation

Summary

Satellite observations have persistently shown that the observed tropical O_3 solar response is very different from what has been predicted by photochemical models. In the upper and lower stratosphere, the observed O_3 response is greater than the modeled response, whereas in the middle stratosphere, the observed O_3 response is insignificant while the model response is significant and positive. This problem seems to remain despite twenty years of efforts.

1.1. Solar Variability and Climate

Although present climate change is largely attributable to greenhouse gases, mounting evidence points to the role of solar variability in modulating the climate over decadal time scales and longer [*Hoyt and Schatten*, 1997; *van Loon and Labitzke*, 1999; *Bond et al.*, 2001; *Lean and Rind*, 2001; *Hu et al.*, 2003]. During the 12th century, extratropical northern hemisphere temperatures [e.g., *Esper et al.*, 2002] and solar activity [*Yau*, 1988; *Jirikowic and Damon*, 1994] were unusually elevated, contributing to the Medieval Warm Period. On the other hand, during the Spoerer Minimum (1450–1550), the Maunder Minimum (1645–1715), and the Dalton Minimum (around 1800), solar activity was suppressed. During the Maunder Minimum, regional mean winter temperatures in North America and Northern Europe declined by 1–1.5°C. Cooling over Europe manifested itself in winter but not in summer [*Pfister*, 1995]. The total irradiance change between current solar maxima and minima (~ 0.1%) extrapolated to the Maunder Minimum is ~ 0.25% [*Lean and Rind*, 2001]. *Lean et al*. [2005] suggested an even lower total irradiance change at Maunder Minimum. Model results predict that such irradiance decline caused a decrease in global mean temperature of less than 0.5°C at that time [e.g., *Rind and Overpeck*, 1993]. However, the occurrence of cooling only in winter (as suggested by proxy records) cannot be explained.

The solar-cycle variability has long been believed to have impact on Earth's climate [*Herschel*, 1801]. Of only ~ 0.1% peak-to-trough variations in the total solar irradiance, the 11 yr solar-cycle variability is most noticeable in the ultraviolet (UV) regions [*Lean and Rind*, 2001]. The variability ranges from ~ 70% at the hydrogen Lyman-α transition line (121.57 nm) to ~ 10% in 200–300 nm [*Marsh et al.*, 2007]. Therefore, any impacts on Earth's climate are likely to be linked through upper atmospheric regions where UV is absorbed. For example, *Meehl et al.* [2009] suggests a top-down mechanism, wherein the production of tropical stratospheric ozone (O_3) is enhanced during a solar-cycle maximum through the absorption of enhanced UV radiation by the oxygen molecule in the Schumann-Runge band (150–240 nm), which in turn leads to an enhanced UV absorption by ozone in the Hartley and Huggins bands (240–330 nm) [*Herzberg*, 1965; *Brasseur and Solomon*, 1984]. The different heating of the stratosphere as a function of latitude due to these absorption processes may modify the tropospheric circulation, leading to changes in the hydrological cycle [*van Loon et al.*, 2007; *Meehl et al.*, 2009]. Since the solar irradiance is strongest over the equatorial region and the stratospheric O_3 is produced mainly in the tropical area, we expect maximum solar-cycle modulation in the tropical O_3 [*Camp et al.*, 2003]. Such solar-cycle modulation can also be transported to higher latitudes by the Brewer-Dobson circulation in the middle atmosphere [*Brasseur*, 1993; *Ineson et al.*, 2011].

1.2. Stratospheric O_3 Response

Stratospheric O_3 is an important atmospheric tracer in Earth's atmosphere. It shields the solar ultraviolet below 315 nm from reaching layers below such that Earth's surface becomes habitable. Therefore, O_3 may be regarded as a signature of life and it is one of the atmospheric tracers that have been targeted in searching for extraterrestrial intelligence. It is formed from recombination of an oxygen molecule (O_2) with an oxygen atom (O), resulting from O_2 photolysis in the Schumann-Runge bands (170−200 nm):

$$\mathrm{O_2} + h\nu\left(170 - 200\ \mathrm{nm}\right) \rightarrow \mathrm{O} + \mathrm{O} \tag{R1}$$

$$\mathrm{O_2} + \mathrm{O} + \mathrm{M} \rightarrow \mathrm{O_3} + \mathrm{M} \tag{R2}$$

The destruction process involves photolysis of O_3 in the Hartley and Huggins bands (240−330 nm) into an excited oxygen molecule [$O_2(^1\Delta)$] and an excited oxygen atom [$O(^1D)$], which is then quenched to O and recombines with O_3 to form two O_2 molecules:

$$\mathrm{O_3} + h\nu\left(240 - 320\ \mathrm{nm}\right) \rightarrow \mathrm{O}\left(^1D\right) + \mathrm{O_2}\left(^1\Delta\right) \tag{R3}$$

$$\mathrm{O}\left(^1D\right) + \mathrm{M} \rightarrow \mathrm{O} + \mathrm{M} \tag{R4}$$

$$\mathrm{O_3} + \mathrm{O} \rightarrow \mathrm{O_2} + \mathrm{O_2} \tag{R5}$$

Reactions R1−–R5 form a complete cycle and were introduced by Sydney Chapman in the 1930s [*Chapman*, 1930]. However, the Chapman cycle alone predicts a factor of ~ 2 times more stratospheric O_3 than observed over the tropics. An additional set of O_3-destroying catalytic cycles, such as those involving odd nitrogen (NO_x) [*Crutzen*, 1970], and odd hydrogen (HO_x) [*Bates and Nicolet*, 1950] are responsible for the missing sinks in the Chapman cycle. In the late 20th century, the global O_3 level was further reduced because of the increased level of odd chlorine radicals released from man-made chlorofluorocarbons

(CFCs) [*WMO*, 2007]. Since 1990s, the atmospheric abundances of CFCs and other ozone-depleting chemicals have been gradually reduced after international regulations on their use and the stratospheric O_3 level has been recovering. However, the recovery is slow due to the long (decadal to centennial) lifetimes of the odd chlorine species. To monitor the O_3 changes and accurately characterize the recovery rate, it is necessary to separate the secular trend from other long-term natural variability. A number of observational studies have indicated that stratospheric O_3 can be modulated by the 11-year solar cycle at all latitudes [*Hood and Soukharev*, 2006; *Gray et al.*, 2010]. The modulation is primarily through photochemical reactions R1 and R3 over low latitudes. The induced O_3 changes are then transported globally by atmospheric circulations [*Kodera and Kuroda*, 2002].

1.3. Model Discrepancies

In photochemical models, the expected O_3 solar response is dominated by net O_3 production due to O_2 photolysis in the mid-stratosphere at 40 km, creating a single-peak maximum of ~ 2–3 %/100$F_{10.7}$ (% change in O_3 concentration per 100 units change in the 10.7- cm solar radio flux) in the stratosphere. Analyses of satellite data, however, reveal a double-maximum vertical structure having a peak of ~ 2%/100$F_{10.7}$ in the upper stratosphere at ~ 45 km (1–2 hPa) and another peak of ~ 3%/100$F_{10.7}$ in the lower stratosphere at ~ 25 km (50–70 hPa) over the tropical region (latitude $\leq 25°$); in the mid-stratosphere, the observed solar-cycle response is insignificant. In these observational studies, multiple linear regression was employed to extract the solar response. Regression analysis requires that all forcings (including, e.g., QBO, ENSO, and solar forcing represented by some training indices) are independent of each other and the responses are linear [*Stolarski et al.*, 1991; *Hood and McCormack*, 1992; *Hood et al.*, 1993; *Reinsel et al.*, 2005]. Consequently, some studies questioned whether such double-maximum structure is a statistical aliasing with nonlinear processes, such as major volcanic eruptions (in the early 1980s and 1990s), ENSO, and QBO. To this end, *Soukharev and Hood* [2006] took the advantage of the period 1992−2003, when there was no major volcanic eruption, and analyzed the O_3 vertical response to the solar cycle modulation using the most recent satellite observations. Their results suggested that the double-maximum structure was robust against volcanic eruptions. *Hood and Soukharev* [2010] revised the regression model to include a potential time-lag dependence of the ENSO effect [*Marsh and Garcia*, 2007] and showed that the vertical response remains the same whether or not the ENSO term is considered in their statistical model. Lastly, *Soukharev and Hood* [2006] also regressed the QBO signal using the 30 hPa zonal wind as the QBO index. They asserted that the double-peak solar response in O_3 was not interfered with by the presence of QBO. Based on a regression model similar to that in *Soukharev and Hood* [2006] (i.e., defining a QBO index using zonal winds), *McCormack et al.* [2007] employed a two-dimensional radiative-dynamics-chemistry model and found that a mid-stratospheric minimum in the O_3 response can be reproduced if a model QBO was imposed. However, *Lee and Smith* [2003] carried out synthetic transient experiments and indicated that using the tropopause momentum forcing as the QBO index would remove the artificial double-peak structure and recover the single-peak profile. Unfortunately, there is no direct measurement of the tropopause momentum forcing and the assertion by *Lee and Smith* [2003] has not been verified observationally to date.

A number of modeling studies have tried to simulate the O_3 response to the 11-year solar forcing in the middle atmosphere using multidimensional models with different levels of complexities in chemistry and dynamics [e.g., *Brasseur*, 1993; *Shindell et al.*, 1999; *Lee and Smith*, 2003; *Marsh et al.*, 2007; *McCormack et al.*, 2007; *Haigh et al.*, 2010; *Kyrölä et al.*, 2010; *Schmidt et al.*, 2010; *Dhomse et al.*, 2011; *Merkel et al.*, 2011; *Beig et al.*, 2012; *Swartz et al.*, 2012]. *Austin et al.* [2008] summarized the O_3 response to the 11-year solar forcing in seven three-dimensional (3-D) coupled radiation-dynamics-chemistry models. They performed transient simulations with anthropogenic forcings, observed sea surface temperature and atmospheric aerosol concentration. The averaged O_3 solar responses from the seven models show positive peaks in the upper and lower stratosphere. The upper stratospheric peak is related to direct photolysis of molecular oxygen at wavelengths less than 240 nm (Reaction R1); the lower stratospheric peak may be a combination of photolysis and weakened Brewer-Dobson circulation [*Kodera and*

Kuroda, 2002] resulting from stratospheric temperature changes. There is a significant spread in the vertical O_3 solar responses among the models, especially in the lower stratosphere (20–30 km). The spread may be a result of aliasing with volcanic aerosol emissions and/or effects of El Niño/Southern oscillation (ENSO) [*Marsh and Garcia*, 2007; *Dhomse et al.*, 2011]. *Schmidt et al.* [2010] and *Dhomse et al.* [2011] also found that the simulated vertical O_3 solar response is insensitive to the presence of QBO. The simulated double-peak structure qualitatively agrees with those observed from satellite observations derived from Halogen Occultation Experiment (HALOE), Stratospheric Aerosol and Gas Experiment (SAGE), and Solar Backscatter Ultraviolet (SBUV) [*Soukharev and Hood*, 2006].

1.4. Strategic Plan

For an accurate simulation of the solar cycle modulations in stratospheric O_3, at least three elements are essential: (1) the UV variability over a typical 11-year solar cycle, (2) a comprehensive list of O_3 photochemical reactions and the catalytic cycles related to O_3 destructions, and (3) dynamical changes induced by solar heating. As discussed above, there have already been a number of studies on the solar-induced dynamical changes. In the upper stratosphere, photochemical equilibrium dominates. Therefore, in this thesis, sensitivity of the upper stratospheric O_3 response to uncertainties in the UV variability will be examined. The solar response of OH, a key O_3-destroying catalyst in that region, will be studied using state-of-the-art ground-based/satellite measurements and chemistry models

Statistical aliasing problems may also be important when interpreting the observations, which is beyond the scope of this thesis.

Chapter 2.

Simulation of Solar-Cycle Response in Tropical Total Column Ozone using SORCE Irradiance*

Summary

The solar responses in tropical O_3 column in the Whole Atmosphere Community Climate Model (WACCM) model will be examined using solar spectral irradiance (SSI) estimated from the Naval Research Laboratory (NRL) solar model and that from recent satellite measurements observed by the Solar Radiation and Climate Experiment (SORCE). Four experiments have been conducted with NRL/SORCE SSI and climatological/observed sea surface temperatures and ice, and all other variability is fixed to test the robustness of the simulated solar response in O_3 against the presence of El Niño/Southern Oscillation (ENSO). Potential aliasing effects from ENSO occur below 20 km, where tropical O_3 concentration is low and has little impact (less than 0.6 DU/100$F_{10.7}$) on the regressed O_3 column response. In the tropical region 24°S–24°N, using the SORCE SSI as a model input leads to a solar response of 5.4 DU/100$F_{10.7}$, which agrees with those obtained from the merged TOMS/SBUV satellite observations. The resultant vertical O_3 response agrees with previous satellite measurements in the

---

* Appeared as Li, K.-F., X. Jiang, M.-C. Liang, and Y. L. Yung (2012), Impacts of SORCE Irradiance on the Simulation of 11-year Solar-Cycle in Total Column Ozone, *Atmos. Chem. Phys. Discuss.*, *12*, 1867−1893, doi: 10.5194/acpd-12-1867-2012.

lower stratosphere but the negative response in the upper stratosphere disagrees with the observed. In contrast, the total O_3 column response is 3 DU/100$F_{10.7}$, which is ~ half of that obtained using SORCE SSI but agrees better with the SAGE and ground-based observations. The resultant vertical O_3 response agrees with previous satellite measurements in the upper stratosphere but the lower stratospheric response is much weaker than observed. This presents a dilemma to our current understanding of stratospheric O_3 response to UV perturbations.

2.1. Motivation

In Chapter 1, the discrepancy between the model and observed O_3 solar response in the stratosphere has been reviewed. An accurate simulation of the solar response relies on three components: changes in top-of-the-atmosphere solar irradiance, changes in O_3 implied from photochemistry, and changes in thermal structures as a result of O_3 changes and dynamical feedbacks. This chapter focuses on the first component.

In most of the previous modeling studies [*Marsh and Garcia*, 2007; *Austin et al.*, 2008; *Dhomse et al.*, 2011], the 11-year solar forcings in UV are reconstructed by the Naval Research Laboratory (NRL) [*Lean et al.*, 1997; *Lean*, 2000]. In the NRL reconstruction, the solar UV variability over a solar cycle is derived based on the correlation of satellite observations with historical sunspot and faculae records. Recent observations over the declining phase of Solar Cycle 23 by the SoLar Stellar Irradiance Comparison Experiment (SOLSTICE) [*Snow et al.*, 2005a] and the Spectral Irradiance Monitor (SIM) [*Harder et al.*, 2010] instruments aboard SORCE satellite suggest an unexpectedly large decrease in solar UV irradiance, which has important implications for O_3 [*Haigh et al.*, 2010]. These observations disagree with previous satellite observations and the NRL reconstruction, adding UV variability as another dimension of uncertainty for upper atmospheric modeling. It has been shown that SORCE SSI may lead to solar-cycle responses in the middle atmospheric O_3 and temperatures that are significantly different from those obtained using NRL SSI [*Cahalan et al.*, 2010; *Haigh et al.*, 2010; *Merkel et* *al.*, 2011]. For example, *Haigh et al.* [2010] showed that the simulated O_3 trend between 2004–2007 becomes negative in the tropical upper stratosphere above 45 km if the SORCE SSI is used. This is in contrast to the model simulation if the NRL SSI is used, which predicts positive O_3 trends in the whole tropical stratosphere. Their simulation seems to be supported by the recent observations by the Microwave Limb Sounder (MLS), where a negative trend in O_3 has also been observed during 2004–2007. Meanwhile, using the three-dimensional Whole Atmosphere Community Climate Model (WACCM), *Merkel et al.* [2011] showed that the simulated negative O_3 trend in the tropical mesosphere is much larger when SORCE SSI is used and agrees better with SABER observations during 2002–2009. But they also noticed that the model response in the middle stratospheric O_3 does not agree with the observations. In addition, SORCE, MLS, and SABER data only cover part of the declining Solar Cycle 23 and great care must be taken when interpreting these trend comparisons. Continuous investigations are required to resolve the discrepancies between models and observations.

Besides the vertical O_3 profiles, there have also been long-term spaceborne measurements of total column O_3 (hereafter denoted by X_{O3}) during 1978–2004 by the Total Ozone Mapping Spectrometer (TOMS) and SBUV [*Stolarski et al.*, 2006]. X_{O3} after 2004 has been measured by Ozone Monitoring Instrument aboard Aura, which is the successor of TOMS. These observations merged together provide the longest satellite record of X_{O3} for exploring interannual and decadal variabilities. These X_{O3} measurements use UV bands that are different from those used for profile O_3 retrievals. In addition, since the lower stratospheric response to the 11-year solar forcing is the main contributor to the X_{O3} response, comparing the observed and model X_{O3} responses may serve as an independent test for model sensitivity to the 11-year solar forcing in the lower stratosphere. There are also long-term ground-based measurements of total column O_3 which are sparse in both space and time [*Fioletov et al.*, 2002].

Randel and Wu (2007) derived the meridional pattern of the 11 yr solar-cycle sensitivity in X_{O3} (in Dobson units per 100 units of 10.7 cm solar radio flux $F_{10.7}$ [*Tapping and Detracey*, 1990] or DU/100$F_{10.7}$) from the merged TOMS/SBUV data using multiple linear regression. In the equatorial region, the derived sensitivity from

TOMS/SBUV data was 5–6 DU/100$F_{10.7}$. They compared this sensitivity to that of the partial column O_3 between 20–50 km integrated from the SAGE measurements during 1979–2005. The resultant sensitivity from SAGE was 2–3 DU/100$F_{10.7}$ only, which agrees with those derived from the ground-based X_{O3} measurements. There has been concern whether an erroneous treatment of an instrumental toggling of TOMS in 1983 might have created the apparently large X_{O3} solar response [*WMO*, 2003, Appendix 4A.2]. However, this error has been corrected in the latest TOMS retrieval algorithm (version 8) and [*Randel and Wu*, 2007] used version 8 retrievals for their analysis. Therefore, the discrepancy among TOMS/SBUV, SAGE, and ground-based X_{O3} solar responses are unlikely to be due to the toggling problem.

This work aims to explore how a coupled dynamics-radiation-chemistry model may simulate the observed solar responses in X_{O3}. The impacts of SORCE and NRL SSIs on the solar-cycle response of tropical X_{O3} in WACCM will be studied. Recent analyses of SORCE data [*DeLand and Cebula*, 2012; *Lean and DeLand*, 2012] reveal that uncorrected instrumental drifts may have resulted in an overestimated UV variations during 2004–2007 as reported in *Haigh et al.* [2010]. The work here thus presents an upper limit of the impact associated with the difference of UV changes suggested by these two measurements. Lastly, since the solar-cycle modulation is stronger in the equatorial region than that in the global averages (see, e.g., Fig. 6 of *Austin et al.* [2008]) and photochemical production of O_3 decreases with increasing latitude, atmospheric dynamics may interact with the solar-cycle modulations and make the interpretation difficult in the extratropics for both model and observational results (see, e.g., [*Jiang et al.*, 2008c; b]), which is out of the scope of this work. Thus latitudes away from tropics will be avoided in this study.

2.2. Model Setup

WACCM is a global atmospheric model with fully coupled chemistry, radiation, and dynamics extending from the surface to the thermosphere based on version 3 of the

Community Atmosphere Model (CAM3) [*Marsh et al.*, 2007]. It has a horizontal resolution of 5° longitude × 4° latitude. There is a resolved stratosphere with fully interactive ozone chemistry that can respond to the UV part of the solar forcing. This model is one of the participants of the Chemistry-Climate Model Validation (CCMVal) activity and has been employed to project the ozone trend in the 21st century [*Morgenstern et al.,* 2010; *Oman et al.*, 2010]. The version used in this work does not have an internal mechanism for generating quasi-biennial oscillations (QBOs), although there have been efforts where relaxation methods have been employed to externally impose the QBO in the simulations [*Matthes et al.*, 2010]. A parametrized gravity wave drag has been used to drive the Brewer-Dobson circulation [*Richter et al.*, 2010]. No volcanic aerosol emissions have been included in our simulations.

We shall explore the impact of two sets of SSI inputs derived from the NRL solar model and from the recent SORCE measurements on the model X_{O3}. The spectral variability between 115–400 nm for 2004–2007 depicted by these two spectral datasets as well as their implications for stratospheric chemistry have been studied in detail by several groups [*Cahalan et al.*, 2010; *Haigh et al.*, 2010; *Merkel et al.*, 2011]. Their model results have also been compared against vertically resolved satellite data that are available during the same period. However, these studies did not cover a full solar cycle due to the limitations of observations.

To mimic a full solar cycle, the SORCE measurements are extrapolated back to the last solar maximum in 2002 using the magnesium-II core-to-wing ratio (Mg-II c/w) index [*Heath and Schlesinger*, 1986]. The Mg-II c/w index describes the variability of radiation from the solar chromosphere and is a good proxy for EUV wavelengths, especially at ~ 205 nm that is important for ozone chemistry. This index is defined as the ratio of the Mg-II H and K lines at ~ 280 nm to the wings of the absorption at ~ 276 and ~ 283 nm, which is less susceptible for instrument degradations. The long-term Mg-II c/w record has been constructed using different satellite measurements of exoatmospheric solar radiation since 1978, including SORCE after 2004 [*Viereck et al.*, 2004; *Snow et al.*, 2005b]. The records from different measurements have been validated against each other and adjusted to composite a single continuous Mg-II c/w index [*Viereck et al.*, 2004].

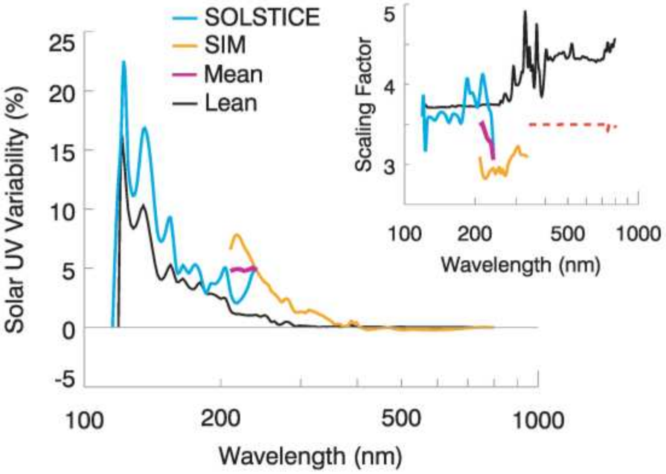

Fig. 2.1. Solar UV spectral variability derived from SORCE SSI. The blue and orange lines correspond to SSI data from SOLSTICE and SIM, respectively. The purple line shows the mean of the two at 210–240 nm. The black line is the NRL SSI variation. All spectra have been convolved to the model grid. The inset shows the spectral scaling factors for extrapolating the observed SSI (April 2004–November 2007) to the solar max in January 2002. For above 340 nm (not important for OH chemistry), an arbitrary factor of 3.5 is applied (dashed).

Thus, for period during January 1, 2004−November 30, 2007, correlation coefficients between the spectral variations observed by SORCE and the composite Mg-II c/w index are obtained for wavelengths between 115 and 400 nm. Using these correlation coefficients, the SORCE measurements are extrapolated back to January, 2002. The extrapolated coefficients are shown in Fig. 2.1. The SORCE UV variability is generally larger than that from the NRL model. The relative difference is ~ 30% at Lyman-α and much larger (factor of 2–6) at 200–280 nm.

The 10 cm solar radio flux, sunspot number and daily planetary K and a indices used in this study were obtained from ftp://ftp.ngdc.noaa.gov/STP/GEOMAGNETIC_DATA/INDICES/KP_AP/. The Multivariate ENSO Index was obtained from http://www.esrl.noaa.gov/psd/enso/mei/. The merged TOMS/SBUV data were obtained from http://acdb-ext.gsfc.nasa.gov/Data_services/merged/data/.

Table 2.1. Model simulations in this study and their identities. The color codes are assigned in accordance with the average contour colors shown in Fig. 2.4. Experiment A is run with solar spectral irradiance (SSI) from the Naval Research Laboratory (NRL) solar model and climatological sea surface temperature and ice (SST/ice). Experiment B is similar to experiment A except that the observed SST/ice is used from 1960 to 2009. Similarly, experiment C is run with exoatmospheric SSI observed by the Solar Radiation and Climate Experiment (SORCE) and climatological SST/ice. Experiment D is similar to experiment C except that the observed SST/ice is used. Experiment E is run with no solar-cycle variability in SSI and the observed SST/ice is used.

Experiment	SSI			SST/ice	
ID	NRL	SORCE	fixed	Climatological	Realistic
A	🟢			🟢	
B	🔵				🔵
C		🟡		🟡	
D		🔴			🔴
E			⚫		⚫

In this work, wavelengths below 240 nm are derived from the spectral measurements by the Solar Stellar Irradiance Comparison Experiment (SOLSTICE) aboard SORCE, whereas wavelengths above 240 nm are derived from the measurements by the Spectral Irradiance Monitor (SIM) aboard SORCE. To drive a solar cycle variation in WACCM, the solar variability in the UV region is characterized by the fractional changes from the (extrapolated) solar maximum of Solar Cycle 23 in 2002 to the solar minimum in 2007. Then for all wavelengths, the evolution from a solar maximum to a solar minimum is assumed to follow that of $F_{10.7}$. The stratospheric chlorine has been fixed in the simulations.

The WACCM model is run with the atmospheric module only so that there is no dynamical coupling between the atmosphere and the ocean. The oceanic variability is prescribed by putting in the sea surface temperatures and ice (SST/ice) as boundary conditions. In order to isolate the effects due to the solar cycle, the model is run with monthly climatological SST/ice (experiments A & C). This reduces the interaction or aliasing with oceanic long-term modes such as the ENSO. To evaluate the effects due to natural oceanic modes, another set of simulations with observed SST/ice is conducted [*Hurrell et al.*, 2008] (experiments B & D). Besides the ENSO, the observed SST/ice also includes a tiny solar-cycle variability of ~ 0.1 K peak-to-trough [*Zhou and Tung*, 2010]. Therefore, such prescription may mimic a coupled atmosphere-ocean system and provide an estimate of the bottom-up effect on the ozone column abundance due to the solar cycle [*Meehl et al.*, 2009]. Lastly, in order to estimate the relative contribution of the simulated solar response due to that tiny solar-cycle variability in the SST/ice, a control run is performed with observed SST/ice and a time-independent solar constant (experiment E).

The presence of enhanced aerosol loading due to major volcanic eruptions (e.g., El Chichon in 1982 and Pinatubo in 1992) may reduce O_3 concentrations in the lower stratosphere due to enhanced chlorine activation. In a model study, *Dhomse et al.* [2011] showed that the estimation of the lower stratospheric O_3 responses can be amplified through the aliasing with volcanic aerosol emissions. They demonstrated that running the model with fixed dynamics or constant aerosols will help minimize the aliasing effect. Thus, in our simulations, a constant background aerosol loading is adopted.

The model was run from January 1960 to November 2009. To avoid analyzing transient signals, the first 10 yr of simulations will be omitted and data will be analyzed only from January 1970 to the end of the simulations. Table 2.1 summarizes and defines the assumptions for these experimental setups.

2.3. Multiple Linear Regression

We follow the procedure for multiple linear regression as described in *Randel and Cobb* [1994]. The simulated X_{O3} time series are first deseasonalized to obtain monthly anomalies, to which a smoothing 1-2-1 filter is then applied. Subsequently, the solar-cycle modulation is retrieved using a simplified regression model delineated in *Li et al.* [2008]:

$$\mathrm{X}_{O_3}(t) = \alpha(t)\cdot t + \beta(t)\cdot F_{10.7}(t) + \gamma(t)\cdot ENSO(t) + \text{residual} \tag{2.1}$$

where X_{O3} represents the monthly anomaly of total column O_3, and $F_{10.7}(t)$ is the 10.7 cm solar radio flux. Since QBO is not simulated in WACCM and atmospheric aerosol is fixed, these terms have been omitted in the regression model. ENSO(t) is the ENSO index described by the Multivariate ENSO Index (MEI) [*Wolter and Timlin*, 2011]. The time-varying coefficients α, β, and γ are the sum of a constant term and annual harmonics:

$$\alpha(t) = A_1 + A_2 \cos \omega t + A_3 \sin \omega t \tag{2.2}$$

where $\omega = 2\pi/12$ months. Therefore a total of 9 parameters are retrieved from the analysis. The uncertainties of the above 3 coefficients are related to the 9 retrieved parameters via the following relation [*Bevington and Robinson*, 1992]:

$$\begin{aligned} \operatorname{var}\{\alpha(t)\} = {} & \operatorname{var}\{A_1\} + \operatorname{var}\{A_2\}\cos^2 \omega t + \operatorname{var}\{A_3\}\sin^2 \omega t \\ & +2\operatorname{cov}\{A_1, A_2\}\cos \omega t + 2\operatorname{cov}\{A_1, A_3\}\sin \omega t \\ & +2\operatorname{cov}\{A_2, A_3\}\cos \omega t \sin \omega t \ . \end{aligned} \tag{2.3}$$

The time-averaged coefficients and the corresponding uncertainties are thus given by

$$\overline{\alpha(t)} = A_1 \tag{2.4}$$

$$\operatorname{var}\{\alpha(t)\} = \operatorname{var}\{A_1\} + \frac{1}{2}\left(\operatorname{var}\{A_2\} + \operatorname{var}\{A_3\}\right) \tag{2.5}$$

where the overbar denotes temporal averages.

Note that *Randel and Wu* [2007] omitted about two years of O_3 observations after the volcanic eruption in 1982 (El Chichon) and 1992 (Pinatubo) to reduce aliasing effects with aerosol loadings. Since the background aerosol level is fixed, these years will be retained in the regression analysis.

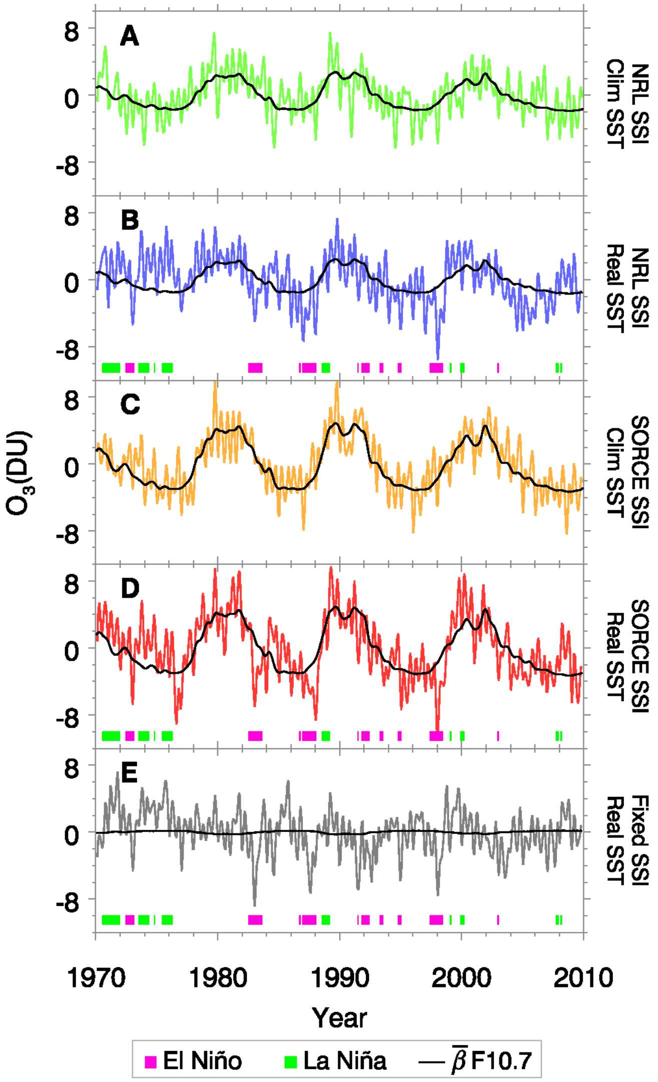

Fig. 2.2. Tropical averages of total column ozone X_{O3} between 24°N and 24°S simulated by WACCM for four experimental setups identified in Table 2.1. The color codes are assigned in accordance with the average contour colors shown in Fig. 2.4. Overlaid black line is the regressed time series related to the solar variability described by the product $\bar{\beta}F_{10.7}$, where $\bar{\beta}$ is the time-averaged regression coefficient and $F_{10.7}$ is the 10.7 cm solar radio flux. Also shown by pink and green strokes are strong El Niño/La Niño events when the absolute values of the Multivariate El Niño/Southern Oscillation Index (MEI) are greater than 1.

2.4. Results

In this section, the solar-cycle responses in the tropical averages will be first established. The relative importance of the modulations due to the solar cycle and the ENSO are studied through the regression coefficients and their uncertainties. Then the latitudinal patterns are presented and are compared with observations derived in previous studies. Finally, the spatial patterns in the tropical area are also discussed.

Tropical averages and regression coefficients

Fig. 2.2 shows the simulated monthly mean of tropical X_{O3} averaged over 24°S–24°N. Latitudinal area weighting has been applied. The color code for the time series corresponds to those of the average contour shown in Fig. 2.4; see below and Table 2.1. Regression is then applied to the equatorial average using Eq. (2.1). The $F_{10.7}$ index multiplied by the time-averaged fitting coefficients, $\bar{\beta}F_{10.7}(t)$, of the respective experiments are shown as black lines.

In all experiments, the regression uncertainties (2σ) of $\bar{\beta}$ are ~ 0.6–0.7 DU/100$F_{10.7}$ (Table 2.2). The regressed coefficients $\bar{\alpha}$ for the trends are insignificant for those runs with climatological SST/ice (experiments A & C). On the other hand, there are nonzero trends for experiments B, D and E with observed SST/ice inputs. Part of them may be due to the trends in the observed SST/ice in the last three decades (~ 0.3–0.6 K) over the tropics [*Keihm et al.*, 2009]. Note that the regressed coefficients remain statistically the same when the linear trend is absent in Eq. (2.1). Therefore, $\bar{\alpha}$ shall not be discussed further. Finally, the regressed coefficients $\bar{\gamma}$ for ENSO are –1.15 ± 0.33DU/MEI, –1.39 ± 0.36 DU/MEI, and –1.41 ± 0.33 DU/MEI for experiments B, D, and E, respectively, and these values are mutually consistent within uncertainties. The anti-correlation implies that X_{O3} is primarily controlled by the vertical motion of the tropopause related to the ENSO modulations, likely through the strengthening/weakening of Brewer-Dobson circulation over the anomalously warm/cool sea surface [*Camp et al.*, 2003].

Table 2.2. Regression coefficients and corresponding uncertainties (±2σ) described in Eqs. (2.1), (2.2), and (2.5). They are temporally averaged according to Eqs. (2.3) and (2.4).

Experiment ID	$\bar{\alpha}$ (DU/yr)	$\bar{\beta}$ (DU/100$F_{10.7}$)	$\bar{\gamma}$ (DU/MEI)
A	-0.01 ± 0.03	3.17 ± 0.69	0.02 ± 0.32
B	-0.05 ± 0.03	2.77 ± 0.71	-1.15 ± 0.33
C	0.00 ± 0.02	5.53 ± 0.66	0.08 ± 0.31
D	-0.03 ± 0.03	5.56 ± 0.77	-1.39 ± 0.36
E	-0.04 ± 0.03	-0.34 ± 0.71	-1.41 ± 0.33

In experiments A and B where NRL SSI is used, the regressed solar-cycle responses $\bar{\beta}$ are 3.17 DU/100$F_{10.7}$ and 2.77 DU/100$F_{10.7}$, respectively, but these values are again mutually consistent within uncertainties. The decrease in the regressed response in experiment B is likely due to modulations by the ENSO signal. Such modulation is most notable during the simulation years 1973–1976, when there were strong and prolonged La Niña events (indicated in Fig. 2.2 by the green bars) which enhances X_{O3} during the solar minimum. Similarly, in experiments C and D, where SORCE SSI is used, the fitted solar-cycle responses $\bar{\beta}$ are 5.53 DU/100$F_{10.7}$ and 5.56 DU/100$F_{10.7}$ respectively, and they are mutually consistent within uncertainties (~ 0.7 DU/100$F_{10.7}$). Therefore, the solar-cycle response in X_{O3} obtained using SORCE SSI is almost two times that obtained using NRL SSI. Furthermore, the difference in the solar-cycle responses obtained using two different SSI settings is statistically significant. The solar-cycle response obtained using SORCE SSI is close to the observed value over 24°S−24°N, which is 5.54 DU/100$F_{10.7}$ [*Randel and Wu*, 2007].

When the solar constant is fixed but the observed SST/ice is employed in experiment E, the regressed solar response $\bar{\beta}$ is only –0.34 DU/100$F_{10.7}$ and is much smaller than the regression uncertainty 0.71 DU/100$F_{10.7}$. Therefore even if there is a tiny modulation due to the solar-cycle signal in the observed SST/ice, the simulated response would not be discernible against the natural variability through our regression model.

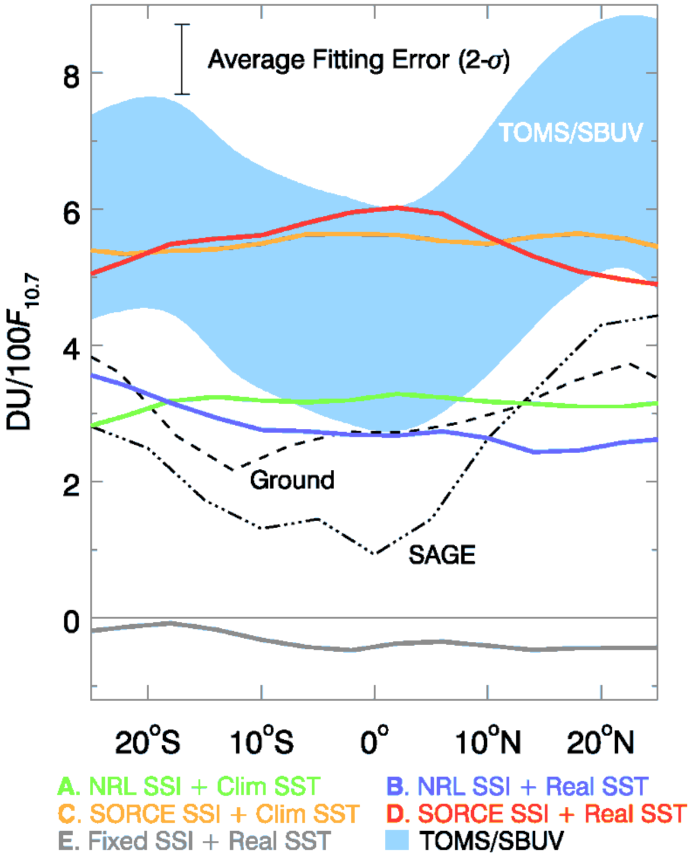

Fig. 2.3. Values of $\bar{\beta}$ as a function of latitudes for four experiments identified in Table 2.1. The color codes are assigned in accordance with the average contour colors shown in Fig. 2.4. Also shown in gray shade is the solar-cycle sensitivity of X_{O3} derived from satellite measurements by the Total Ozone Mapping Spectrometer (TOMS) merged with the Solar Backscatter Ultraviolet (SBUV). The dashed line is the corresponding sensitivity derived from ground-based measurements. Both data of TOMS/SBUV and ground-based measurements are extracted from Fig. 12 of Randel and Wu [2007]. The error bar shows the average regression error, which is 0.6 DU/100$F_{10.7}$ (2σ).

Latitudinal patterns and the equatorial paradox

Fig. 2.3 shows the latitudinal patterns of the time-averaged solar-cycle response between 24°S–24°N. To obtain these results, the regression analysis has been applied to individual zonal averages at different latitudes. The regression uncertainty (2σ) is roughly equal to the error bar shown in Fig. 2.3, which is ~ 0.6 DU/100$F_{10.7}$. Also shown are the solar-cycle response derived from the TOMS/SBUV data (light blue shade), the ground-based measurements made using Dobson and Brewer spectrophotometer, and the filter ozonometer (dashed line) [*Fioletov et al.*, 2002]. These data are extracted from Fig. 6 of *Randel and Wu* [2007].

For experiments A and B with NRL SSI input, the solar-cycle responses are ~ 3 DU/100$F_{10.7}$. This agrees with those derived from the ground-based measurements [*Austin et al.*, 2008]. In contrast, experiments C and D with SORCE SSI input produce solar-cycle responses of ~ 5.4 DU/100$F_{10.7}$, about a factor of 2 larger than those in experiments A and B, and they agree with those derived from TOMS/SBUV.

In all experiments with solar-cycle forcings, the values of $\bar{\beta}$ corresponding to the WACCM runs are relatively constant over the tropics, consistent with previous modeling studies [*Brasseur*, 1993; *Lee and Smith*, 2003; *Tourpali et al.*, 2003; *Egorova et al.*, 2004; *Austin et al.*, 2008]. In contrast, the latitudinal patterns in TOMS/SBUV and ground-based measurements are slightly lower at the equatorial region below 20° N/S. Previous simulations by *Lee and Smith* [2003] and *McCormack et al.* [2007] using 2-D chemical transport models with solar-cycle forcings only predict a constant response in the equatorial region. When QBO is included in the simulations, they both found that the solar-cycle response near the equator becomes lower than that in the mid-latitudes. Nonetheless, they drew totally different conclusions: *Lee and Smith* [2003] assert that such decrease in the response could be statistical interferences between the solar-cycle modulation and QBO in the regression analysis while *McCormack et al.* [2007] assert that it is caused by genuine dynamical interactions. *Hood and Soukharev* [2003] arrive at the same assertion proposed by *McCormack et al.* [2007]. However, *Camp et al.* [2003], who apply a different statistical technique (the empirical orthogonal functions) to the merged TOMS/SBUV data, seem to support the assertions by *Lee and Smith* [2003]. Moreover, an examination of the CCMVal 3-D models by *Austin et al.* [2008] does not reveal such a decrease in the solar-cycle response near the equatorial region. However, given that the implementation of a realistic QBO in 3-D models has not matured, it is hard to conclude which assertion is more plausible. Therefore more definitive 3-D simulations of X_{O3} with more realistic components of solar-cycle variability and QBO mechanisms will be required to discern their individual effects. There is no significant solar response simulated in experiment E. The regression coefficient $\bar{\beta}$ is about –0.3 DU/100$F_{10.7}$ in the tropics but is smaller than the regression uncertainty.

Tropical spatial patterns

Finally, the regression analysis has also been applied to the time series at individual model grid points. Fig. 2.4 shows the equatorial spatial patterns of $\bar{\beta}$ between 24°N–24°S. The corresponding regression errors (2σ) are shown in Fig. 2.5.

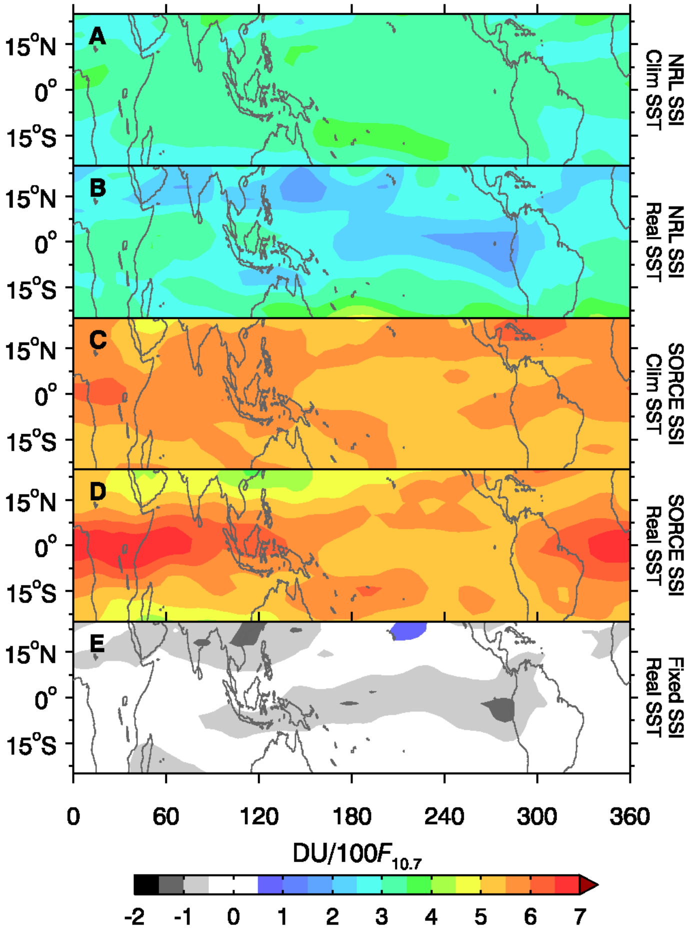

Fig. 2.4. Time-averaged regressed coefficients $\bar{\beta}$ for all experiments in the tropics. The multiple linear regression is applied to all individual grid points.

Overall, the solar-cycle responses are close to the respective equatorial averages and are relatively constant over the tropics within ±0.5 DU/100$F_{10.7}$, which is of the same order as the regression uncertainties. For experiments B and D, when observed SST/ice are used, the solar-cycle responses are anomalously low in the equatorial Pacific. As in the case as QBO, this is likely due to the statistical interference from the ENSO modulation. This can be seen by noticing that the spatial patterns of the regression uncertainties have a lot more structures when the observed SST/ice are included, especially over the Cold Tongue and the Warm Pool regions (Fig. 2.5). In the subtropics, the uncertainties are generally ~ 1 DU/100$F_{10.7}$ and can be greater than 1.3 DU in the Northern Hemisphere. In the central Pacific, the minimum uncertainties can be as low as 0.4 DU/100$F_{10.7}$ for experiments A and C; they are slightly higher (~ 0.6 DU/100$F_{10.7}$) for experiments B and D. These clearly show the effects of ENSO. It also becomes obvious when one examines the spatial pattern of the regressed coefficients $\bar{\gamma}$ related to ENSO, shown in Fig. 2.6 only for experiments B, D, and E. The coefficients $\bar{\gamma}$ are negative all over the tropics. The strongest ENSO modulations of ~ 3 DU/MEI are found over the north- and south- eastern Pacific. The modulations are almost zero over the Warm Pool region, demonstrating the dipole structures of the ENSO effects. These spatial patterns are similar to the fourth EOF obtained by *Camp et al.* [2003].

As in previous sections, the regressed solar response of –0.3 DU/100$F_{10.7}$ in experiment E is insignificant compared to the regression uncertainty shown in Fig. 2.5, implying that the modulation due to the solar-cycle signal in the observed SST/ice is tiny. The regression uncertainty seems to be independent of the input solar flux and SST/ice. Rather, it depends largely on the internal variability of the model.

Vertical responses

Lower stratospheric O_3 response between 20–30 km is the main contributor to X_{O3} response. To further elucidate the sensitivity of WACCM to the UV perturbations, Fig. 2.7 shows the tropical vertical O_3 responses between 25°N–25°S in. These vertical profiles are derived from monthly averaged model outputs. The uncertainties of the

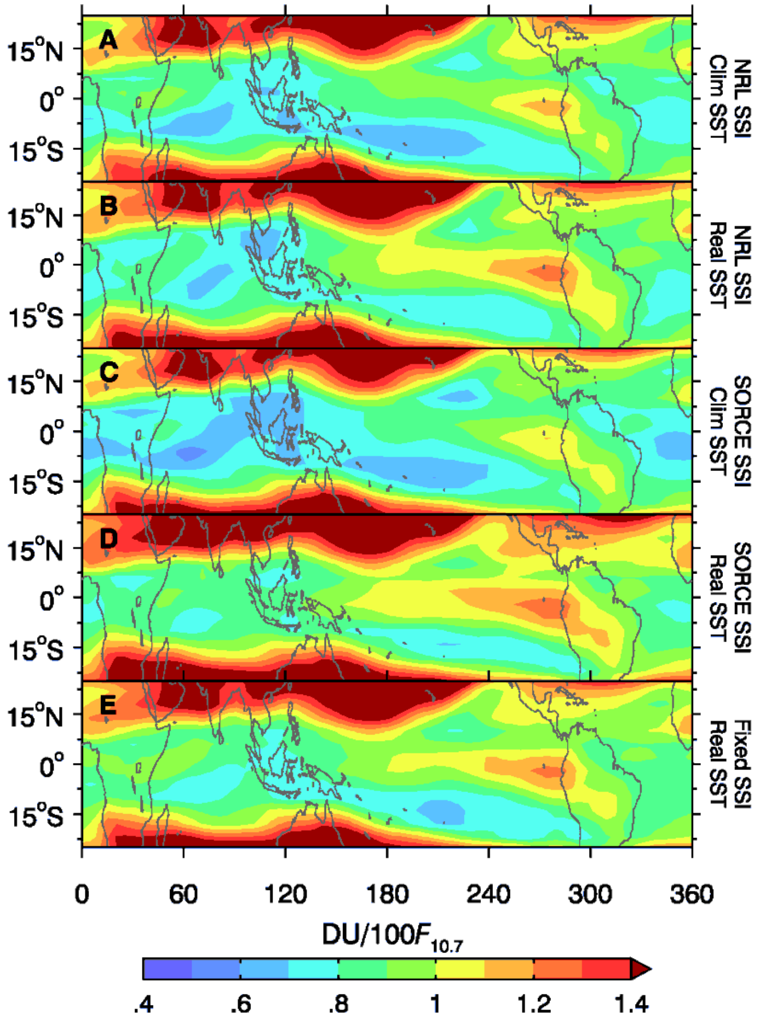

Fig. 2.5. Same as Fig. 2.4 except for the uncertainty (2σ) of the regressed coefficient, var$\bar{\beta}$, on individual model grid points

model responses are ~ 0.5 %/100$F_{10.7}$ above 20 km and ~ 2 %/100$F_{10.7}$ below 20 km. The averaged HALOE, SAGE, and SBUV observations reported by *Soukharev and Hood* [2006] are represented by the dots with error bars. Observationally, there is an upper stratospheric peak of 2% between 40–60 km and a lower stratospheric peak of 3% near 20 km. At 30 km, the observed middle stratospheric response is statistically insignificant.

For experiments A & B, where NRL SSI is used, a double-peak structure is apparent in the simulated O_3 response shown, although it is not as pronounced as the observed. The model O_3 response shows a primary peak of 2% at 40 km which is close to the observed response at those altitudes. The secondary peak of 1% at 20 km is much weaker than the observed response in the lower stratosphere. In contrast, in experiments C & D where SORCE SSI is used, the double-peak structure is absent and the upper stratospheric response between 40 km and 60 km is negative (~ 1%), disagreeing with the observed. However, in the lower stratosphere between 20–30 km, the simulated O_3 response agrees better with the observed; it is more than 3 times larger than that simulated using NRL SSI and ranges between 2–3%. In the middle stratosphere, both the use of NRL and SORCE SSI lead to significant enhancement of O_3, disagreeing with the observed insignificant response at those altitudes. Further investigations are required to understand the relative contributions to the simulated O_3 response from photolysis, O_3 catalytic chemistry, and dynamics due to UV perturbations.

Above 20 km, the model O_3 response is insensitive to the SST boundary conditions. On the other hand, the model responses show large spread below 20 km, likely due to aliasing with the ENSO effect. This assertion of the aliasing effect is supported by the

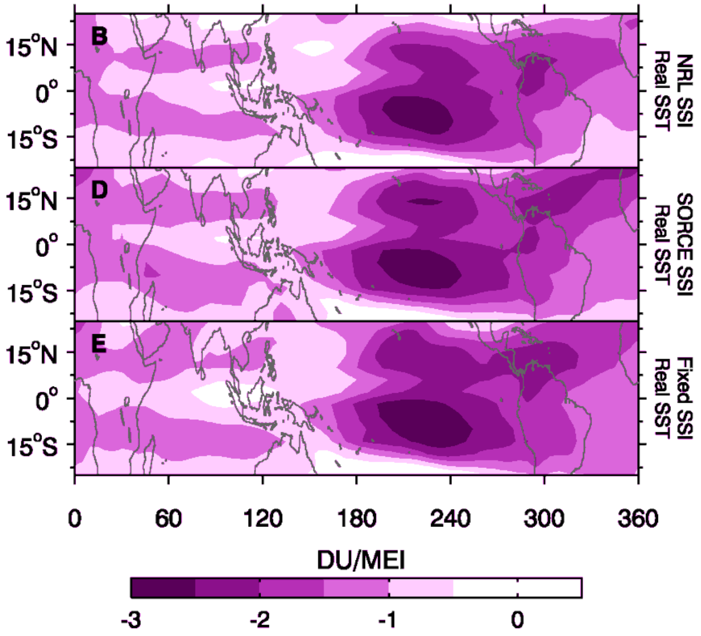

Fig. 2.6. The spatial pattern of the time-averaged regressed coefficients $\bar{\beta}$ related to ENSO for experiments B, D, and E.

control experiment (experiment E), where there is no significant solar signal above 20 km, but there is an artificial negative solar response below 20 km. However, since majority of tropical O_3 is located above 20 km, this aliasing does not impact on the X_{O3} response significantly.

2.5. Summary and Discussions

This work extends the modeling studies of *Haigh et al.* [2010] and *Merkel et al.* [2011] for middle atmospheric O_3 concentrations. Our simulations were done with much longer periods (1960–2009) in an attempt to minimize statistical uncertainties. The solar-cycle responses of total column ozone (X_{O3}) over the tropics in the WACCM model were simulated using spectral solar variability in UV derived from NRL and SORCE SSIs. For SORCE where the measurements cover only from 2004 to 2010, a full Solar Cycle 23 has been extrapolated based on the Mg-II c/w index.

Using the (extrapolated) SORCE spectral UV data, the stimulated solar-cycle modulation in tropical X_{O3} has a sensitivity ~ 5.4 DU/100$F_{10.7}$ or ~ 2%/100$F_{10.7}$. This agrees with the sensitivity observed by TOMS/SBUV, although TOMS/SBUV observations suggest a local minimum of ~ 4.5 ± 1.5 DU/100$F_{10.7}$ at the equator, which is not simulated in the model. However, this is ~ twice the sensitivity observed by SAGE and ground-based measurements. On the other hand, using NRL spectral UV data, the simulated tropical X_{O3} response is ~ 3 DU/100$F_{10.7}$ or ~ 1%/100$F_{10.7}$ and agrees well with the SAGE and ground-based measurements.

The difference in the simulated X_{O3} responses that were obtained using NRL and SORCE SSI mainly comes from the lower stratosphere. The SORCE simulation results in a lower stratospheric O_3 response ~ 3 times larger than the NRL simulation and agrees better with previous satellite observations. In contrast, the SORCE simulation suggests a negative response in the upper stratosphere which does not agree with the observed, whereas the NRL simulation agrees better with the observations in that region. This presents a dilemma to our current understanding on stratospheric O_3 sensitivity to UV

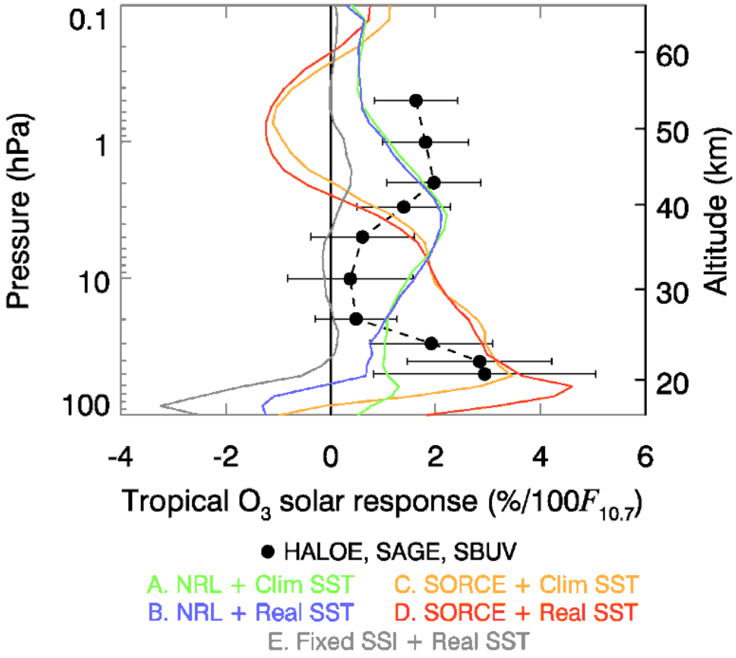

Fig. 2.7. Tropical average vertical O_3 response between 25°N–25°S. The color scheme follows that in Table 2.1. The satellite averages from HALOE, SAGE, and SBUV measurements and their uncertainties are extracted from *Soukharev and Hood* [2006]. The uncertainty of the regressed model responses are ~ 0.5 %/100$F_{10.7}$ above 20 km and ~ 2%/100$F_{10.7}$ below 20 km.

perturbations. However, note that recent studies [*DeLand and Cebula*, 2012; *Lean and Deland*, 2012] reveal that uncorrected instrumental drifts may have caused unexpectedly large UV variations during 2004–2007 as reported in *Haigh et al.* [2010]. Therefore, the simulated X_{O3} solar response may have been overestimated. The model runs performed in this work will be re-evaluated when corrected SORCE SSI are available.

Multiple linear regression has been frequently used for examining solar-cycle modulations and other forcings in global ozone data as well as other atmospheric variables [*Hood and Soukharev*, 2006; *Soukharev and Hood*, 2006; *Randel and Wu*, 2007; *Hood et al.*, 2010; *Zhou and Tung*, 2010]. It is easy to implement but it also has to assume that the forcings are independent of each other and that the responses are linear. However, in reality these assumptions may not always hold. For example, *Meehl et al.* [2009] suggests that the net effect of increased solar insolation during solar maximum conditions may result in stronger trade winds in the tropical Pacific, which may also impact the Walker circulation and hence ENSO. It is thus important to consider the regression uncertainties when interpreting the results. In this chapter, it is shown that the inclusion of ENSO in the model runs does not statistically modify the simulated solar sensitivity, which is consistent with the conclusion by *Dhomse et al.* [2011].

When studying the potential impacts in our regression coefficients due to the presence of ENSO, the same regression model have been used for different simulations with and without ENSO forcings. This is slightly different from the work of *Marsh and Garcia* [2007], where they applied two different regression models with and without the ENSO term on the same simulation. On the other hand, *Zhou and Tung* [2010] examined the solar-cycle modulation in a 150 yr record of global SST and found that the resultant solar response is neither La-Niña-like nor El-Niño-like. Their conclusion emphasizes the use of long-term records for establishing a statistically robust signal. Therefore, a longer simulation up to a centennial time scale may be required to clarify the interaction between the ENSO and the solar cycle in model O_3.

Unfortunately our model does not have a prescribed/simulated QBO to further investigate its effect (generic/statistical alias) on the extracted X_{O3} response [*Schmidt et al.*, 2010; *Dhomse et al.*, 2011]. *Kuai et al.* [2009] has shown that QBO may interact with the solar cycle nonlinearly through wave-semiannual oscillation. This effect must be considered in future modeling studies.

The difference in the X_{O3} solar-cycle sensitivity to UV found in this work is likely to be applicable to other CCMVal models, although there may be some nonlinearity due to dynamical changes. Analogous simulations using other CCMVal models help evaluate the robustness of these changes in solar-cycle sensitivities [*Swartz et al.*, 2012].

Chapter 3.

Mid-Latitude Atmospheric OH Response to the Most Recent 11-Year Solar Cycle[†]

Summary

The hydroxyl radical (OH) plays an important role in middle atmospheric photochemistry, in particular ozone (O_3) chemistry. Because it is mainly produced through photolysis and has a short chemical lifetime, OH is expected to show rapid responses to solar forcing (e.g., the 11-year solar cycle), resulting in variabilities in related middle atmospheric O_3 chemistry. Here we investigate such OH variability using long-term observations (from space and the surface) and model simulations. Ground-based measurements and data from the Microwave Limb Sounder (MLS) on NASA's Aura satellite suggest a ~ 7–10% decrease in OH column abundance from solar maximum to solar minimum that is highly correlated with changes in total solar irradiance (TSI), solar Mg II index, and Lyman-α during Solar Cycle 23. However, model simulations using a

---

[†] Part of the chapter has been submitted to *Proc. N. Acad. Sci. U. S. A.* in Wang, S., K.-F. Li, T. J. Pongetti, S. P. Sander, Y. L. Yung, M.-C. Liang, N. J. Livesey, M. L. Santee, J. W. Harder, M. Snow, and F. P. Mills (2012), Mid-latitude Atmospheric OH Response to the Most Recent 11-year Solar Cycle.

commonly accepted solar UV variability parameterization give much smaller OH variability (~ 3%). While this discrepancy could result partially from the limitations in our current understanding of middle atmospheric chemistry, recently published solar spectral irradiance data from the SORCE suggest a solar UV variability that is much larger than previously believed. With a solar forcing derived from the SORCE data, modeled OH variability (~ 6–7%) agrees much better with observations. Model simulations also reveal the detailed chemical mechanisms, suggesting that such OH variability and the corresponding catalytic chemistry may dominate the O_3 response to SC in the upper stratosphere. Continuing measurements through Solar Cycle 24 are required to further understand this OH variability and its impacts on O_3.

3.1. Motivation

As mentioned in previous chapters, accurate simulations of the O_3 response to SC is required for better understanding the sun-climate relation [*Hood et al.*, 2010; *Matthes et al.*, 2010]. However, the SC signal in O_3 simulated by different models show quantitative differences, which may be due to differences in model resolutions, model parameterizations related to dynamical processes, and/or photochemistry that has not yet been critically examined [*Brasseur*, 1993; *Austin et al.*, 2008]. Diagnostic studies must involve not only O_3 but also species that catalytically destroy O_3, such as odd-hydrogen ($HO_x = H + OH + HO_2$) [*McElroy and Salawitch*, 1989; *Osterman et al.*, 1997; *Sandor and Clancy*, 1998; *Canty and Minschwaner*, 2002; *Mills et al.*, 2003; *Salawitch et al.*, 2005].

The major catalytic loss terms for odd oxygen above 40 km are associated with the HO_x family [*Osterman et al.*, 1997; *Jucks et al.*, 1998]. The important rate-limiting steps in these catalytic cycles are the $OH + O_3$ (or O) and $HO_2 + O_3$ (or O) reactions.

Since HO_x is the controlling chemical family for O_3 in the upper stratosphere it is important to understand the reactions that produce and destroy HO_x there. Reactions which create HO_x are:

$$O_3 + h\nu \rightarrow O\left({}^1D\right) + O_2 \tag{R6}$$

$$O\left({}^1D\right) + H_2O \rightarrow 2OH \tag{R7}$$

and

$$H_2O + h\nu \rightarrow OH + H \,. \tag{R8}$$

while the removal processes are

$$OH + HO_2 \rightarrow H_2O + O_2 \tag{R9}$$

and

$$H + HO_2 \rightarrow H_2 + O_2 \,. \tag{R10}$$

The key reactions involved in HO_x partitioning are

$$O + HO_2 \rightarrow OH + O_2 \tag{R11}$$

and

$$O + OH \rightarrow H + O_2 \,. \tag{R12}$$

Many of the rate constants for the above reactions are highly uncertain at upper stratospheric temperatures, leading to significant uncertainties in model calculations of the OH vertical profile. Measurements of OH from FTUVS will help constrain the sources and sinks of ozone and contribute to the understanding of upper stratospheric ozone trends.

3.2 Forcing of HO_x by the 11-Year Solar Cycle

Because OH is mainly produced through photolysis (Reactions R6 and R7) and has a short chemical lifetime (~ hours), OH is expected to show rapid responses to solar forcing, e.g., the 11-year solar cycle. The resulting OH variability can serve as a good indicator of solar-induced changes in atmospheric composition and chemistry, in particular, middle atmospheric O_3 chemistry due to catalytic HO_x reaction cycles.

However, in the past, very few studies have been performed on the HO_x response to the solar cycle [*Canty and Minschwaner*, 2002; *Mills et al.*, 2003]. Moreover, little attention has been paid to the impacts of such OH changes on O_3, given the fact that significant differences exist among various studies on O_3 response to the solar cycle [*Brasseur*, 1993; *Soukharev and Hood*, 2006; *Randel and Wu*, 2007; *Austin et al.*, 2008; *Haigh et al.*, 2010; *Kyrölä et al.*, 2010; *Merkel et al.*, 2011; *Beig et al.*, 2012; *Li et al.*, 2012; *Swartz et al.*, 2012]. The lack of investigations on HO_x solar cycle variability is mainly due to the limited long-term systematic observations. Among the handful of available ground-based OH column measurements [*Burnett and Burnett*, 1996; *Iwagami et al.*, 1998; *Cageao et al.*, 2001; *Canty and Minschwaner*, 2002; *Mills et al.*, 2003] that show large discrepancies, two measurements are long term: our OH measurements at NASA Jet Propulsion Laboratory's (JPL) Table Mountain Facility (TMF) since 1997 [*Cageao et al.*, 2001; *Mills et al.*, 2003] and observations at NOAA Fritz Peak Observatory (FPO) in Colorado since 1977 [*Burnett and Burnett*, 1996; *Canty and Minschwaner*, 2002]. Based on the FPO OH record over 1977–2000, OH column variability of ±4.2% was derived and believed to be associated with the solar cycle [*Canty and Minschwaner*, 2002]. TMF OH data over 1997–2001 also implied a solar cycle signal [*Mills et al.*, 2003], while a more solid conclusion requires a longer data set to cover at least one complete solar cycle. We now have an extended FTUVS OH data record for nearly 15 years, covering the entire Solar Cycle 23 and the rising part of Solar Cycle 24. This long record, in combination with the unique satellite measurements of OH from MLS on board NASA's Aura satellite (2004–2011) [*Pickett*, 2006; *Pickett et al.*, 2008; *Wang et al.*, 2008], provides a great opportunity to investigate the solar cycle effect on HO_x chemistry.

The objectives of the present work include: (i) providing observational evidence of SC-related changes in OH column abundance (X_{OH}) from more than 15 years of ground-based measurement, augmented by 5-year satellite OH measurements by the Microwave Limb Sounder (MLS) aboard Aura; (ii) quantifying the impacts of using SORCE UV variability on X_{OH} SC variability with a three-dimensional (3-D) whole-atmosphere community climate model (WACCM) [*Marsh et al.*, 2007] and a one-dimensional (1-D) photochemical model [*Allen et al.*, 1984]; and (iii) estimating the sensitivity of stratospheric O_3 to the SC-related OH changes obtained in (ii). Note that previous studies on the O_3 response to SC investigate the overall O_3 variability due to chemistry and radiation. Our objective (iii) is to illustrate the role of OH in the SC modulations of O_3 chemistry.

This study is the first effort using long-term OH measurements from space and the surface to investigate the OH response to the SC, providing a basis for simulating long-term variability of HO_x chemistry in the middle atmosphere.

3.3. Data and Models

Ground-based FTUVS at TMF measures the total OH column under clear-to-lightly cloudy conditions. The major systematic error is the uncertainty in the OH line center absorption cross section (10%). The precision for a single data point (~ 15 minute interval) is generally within 10% and is substantially improved when using the daily max determined from the polynomial fit of the diurnal variation. The gaps (1–2 months in some cases) in the time series are due to weather, instrument adjustments or upgrades, and measurements for other species. When deriving the SC signal using regression, an index describing the vertical propagation of the quasi-biennial oscillation (QBO) in the stratosphere was also included in the analysis, but was found to be insignificant. The effect of ENSO (El Niño/La Niña-Southern Oscillation) was also found to be negligible.

MLS OH data used in this study are from v3.3 retrieval software. The systematic uncertainty is within 8% over 32–0.0032 hPa [*Pickett et al.*, 2008]. We use data at 21.5–0.0032 hPa to avoid the increasing noise due to H_2O absorption at higher pressures. The zonal mean around TMF [29.5°N, 39.5°N] is used. A similar analysis using data from a 10°×25° grid box at TMF was also performed. The results are similar to those presented here.

WACCM uses MOZART3 as the chemical mechanism [*Marsh et al.*, 2007]. Chemical species are all allowed to vary during model runs. For each UV setting, the

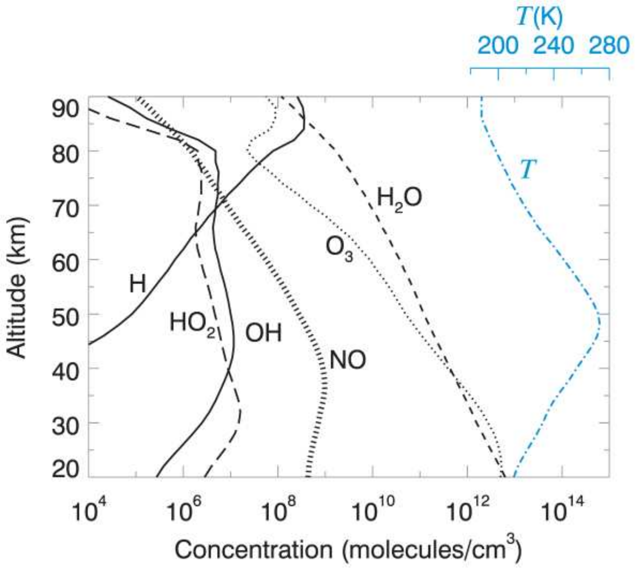

Fig. 3.1. Mean profiles in the 1-D model

model is run from 1960 to 2010. The first 4 years are ignored to allow the model to spin-up. We use the monthly mean output to derive the OH SC signal. We also generated daily max outputs during solar max year and solar min year to compare with results using monthly mean. The diurnal effect is found to be very small.

The 1-D Caltech/JPL photochemical model includes over 100 chemical species, over 460 thermal and photochemical reactions, vertical transport (eddy, molecular, and thermal diffusion), and coupled radiative transfer [*Allen et al.*, 1981]. The chemical kinetics have been updated to JPL06-2 [*Sander et al.*, 2006]. A more recent update of JPL10-6 [*Sander et al.*, 2011] does not introduce significant differences on major reactions related to HO_x chemistry. 65 layers are used to cover from the ground to 130 km. The OH fluxes at the surface and the top of the atmosphere are fixed as zero. During model runs, chemical species are not constrained unless otherwise stated. The temperature profile is fixed. The model has been applied to study the diurnal cycle of OH [*Pickett et al.*, 2006]. Typical model profiles of OH, O_3, and related species are shown in Fig. 3.1.

The SOLSTICE measurement has a spectral resolution of 0.1 nm and an absolute accuracy within 5%. The SIM measurement has varying spectral resolution (~ 1 nm in UV) and an absolute accuracy within 2%.

3.4. Observational Evidences

Studies on SC-modulations of OH had been limited in the past by the lack of long-term systematic observations. The only two long-term records are X_{OH} measurements at TMF in California [*Cageao et al.,* 2001] and at NOAA Fritz Peak Observatory (FPO) in Colorado [*Minschwaner et al.,* 2003]. Based on the FPO X_{OH} data during 1977–2000, an X_{OH} variability of ±4.2% (or 8.4% peak-to-valley), was derived and attributed to the 11-year SC [*Mills et al.*, 2002]. A trend suggestive of a similar SC response in TMF X_{OH} data during 1997–2001 was also reported [*Mills et al.*, 2003], but the robustness of such analysis was limited by the short period of the observations. In this study, we update TMF X_{OH} data to 1997–2011, covering most of the SC 23 and the rising portion of SC 24.

X_{OH} is measured by a high-resolution Fourier transform ultraviolet-visible spectrometer (FTUVS) at TMF at an altitude of ~ 2.3 km in Wrightwood, California (34.4°N, 117.7°W) [*Cageao et al.*, 2001]. FTUVS makes diurnal X_{OH} measurements during daytime. Two dominant natural variabilities of OH are the diurnal cycle due to the change of solar zenith angle (SZA) over the course of a day and the seasonal cycle which is a combined effect of varying SZA and sources of OH [*Li et al.*, 2005]. To focus on the SC signal, we first minimize the diurnal effect by using daily max (Fig. 3.2a) determined by a polynomial fit of the diurnal pattern [*Li et al.*, 2005]. The average time of daily max is close to 20:00 Universal Time (UT) (local noon). To minimize the seasonal effect, we applied a fast Fourier transform (FFT) low-pass filter to the X_{OH} daily max. The result of 2-year FFT (removing variations with frequencies higher than once every two years) is selected to best represent the long-term variability that is primarily due to the SC (Fig. 3.2a, red line). Further FFT filtering smears the SC signal, while less FFT filtering retains additional interannual features that are not related to SC (e.g., 1-year FFT shown in Fig. 3.2a, green line). We also applied a regression analysis using the long-term Lyman-α index as a proxy for SC. The results are consistent with FFT analysis. All results are normalized by the all-time-mean X_{OH} (Fig. 3.2c). The TMF X_{OH} SC variability is found to be 10±3%

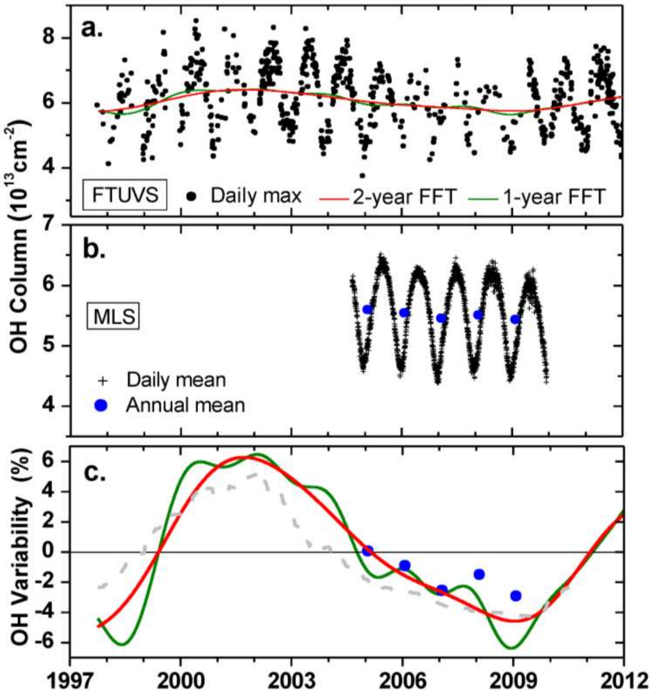

Fig. 3.2. Daily max OH column at TMF and its SC variability. (a) Daily max FTUVS X_{OH} (black) and its long-term variability based on FFT (red and green). (b) Daily zonal mean MLS X_{OH} around TMF latitude (black) and its annual mean (blue). (c) Long-term FTUVS X_{OH} variability normalized to all-time-mean (red and green: from FFT; gray: from regression) and the comparable variability in MLS X_{OH} (blue)

from peak to valley, where the uncertainty is estimated from regression described by Eq. (2.5). This 10% variability agrees with that observed over FPO [*Canty and Minschwaner*, 2002], although the absolute values of X_{OH} from FPO and TMF, both in mid-latitudes, have shown statistical differences of several tens of percent [*Mills et al.*, 2002].

Since the launch of Aura in July, 2004, daily global OH distribution has been measured by MLS [*Pickett*, 2006]. Excellent quality MLS OH data has been demonstrated through extensive validations with airborne and ground-based measurements and modeling [*Canty et al.*, 2006; *Pickett et al.*, 2008; *Wang et al.*, 2008]. Nearly continuous MLS OH data are available from 2004 (middle of the declining phase of SC 23) to the end of 2009

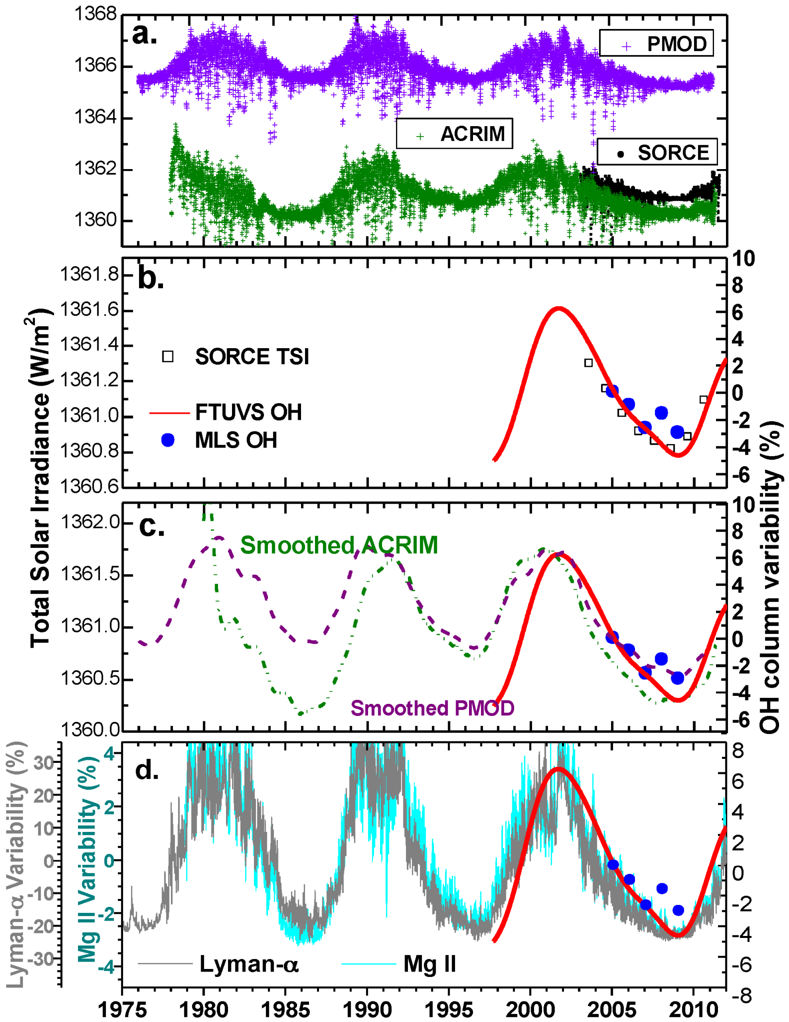

Fig. 3.3. OH SC variability correlates well with solar parameters. (a) Daily mean TSI from SORCE (black), PMOD composite (purple), and ACRIM composite (green). (b) FTUVS (red) and MLS (blue) X_{OH} variability (see Fig. 3.2) in comparison with variability in annual mean SORCE TSI (black). (c) Same as (b), but replacing SORCE TSI with smoothed ACRIM and PMOD composites. The PMOD TSI was adjusted by 4.7 W/m^2. (d) X_{OH} variability in comparison with variabilities in Lyman-α (gray) and Mg II (cyan)

(start of SC 24). To support TMF observations, we focus on MLS OH at TMF latitude (29.5°N–39.5°N). Data between 21.5–0.0032 hPa are integrated to give an estimate of X_{OH}, which covers ~ 90% of the total atmospheric OH [*Wang et al.*, 2008]. Therefore such

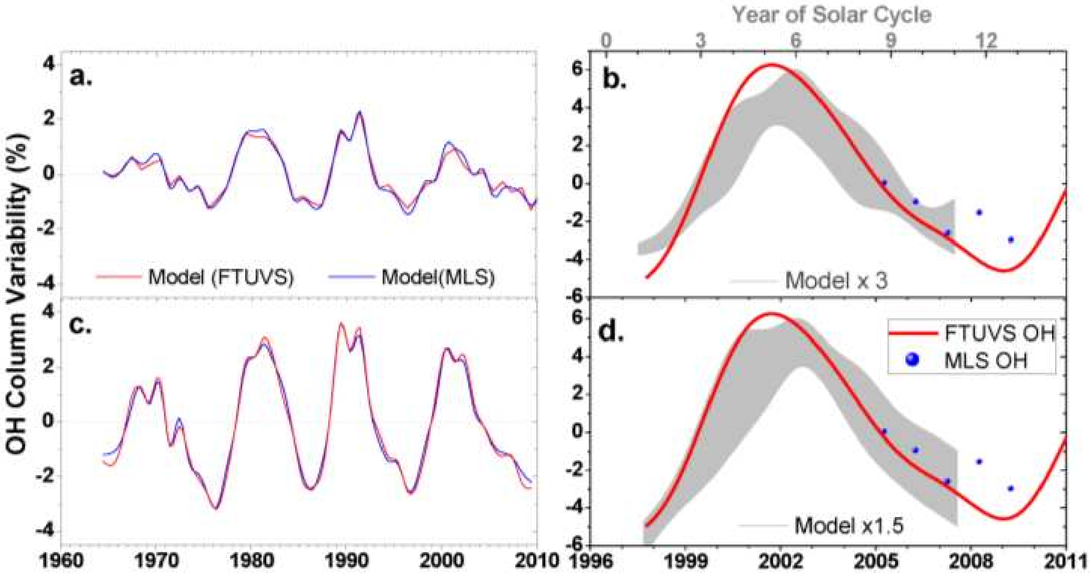

Fig. 3.4. Comparison of OH SC variabilities from WACCM and observations. (a) Modeled variability of annual mean X_{OH} (using NRL solar forcing) integrated over the altitude ranges for FTUVS (red) and MLS (blue) X_{OH}. (b) Model X_{OH} variability is increased by a factor of 3 (gray) to compare with observed X_{OH} SC signal (red and blue). The gray band indicates the scatter range of model X_{OH} variability over the simulated SCs. (c) and (d) are equivalent to (a) and (b) but for model results using SORCE SSI.

integration is expected to include most of the SC signal. Furthermore, the average MLS overpass time at TMF during daytime is ~ 21:00 UT [*Wang et al.*, 2008], making MLS X_{OH} close to TMF daily max X_{OH} (~ 20:00 UT). Fig. 3.2b shows the zonal mean daily MLS X_{OH} over TMF and the annual average (mid-August to mid-August) in which the seasonal variation is removed. The first-year mean (Aug 2004 to Aug 2005) is used to normalize the annual mean X_{OH} to obtain the relative variability (Fig. 3.2c, blue), which is primarily due to the SC, with small additional interannual variations. The resultant trend is in good agreement with that of TMF X_{OH}, although only five annual mean MLS data points are available and the slightly high MLS X_{OH} during 2007–2008 may require further investigation. Between 2004 and 2009, MLS annual mean X_{OH} decreased by over 3%. Based on the scale of TMF X_{OH} variability, we estimate the total SC signal in MLS X_{OH} to be ~ 7%.

As a robustness test, the X_{OH} SC signals obtained above are compared with observations of various solar parameters (Fig. 3.3). Independent TSI measurements have been provided by a number of satellite instruments since 1978. Due to calibration issues, TSI data from different instruments may show similar trends but different absolute values. Based on these observations, various versions of TSI composite have been constructed, e.g., ACRIM (primarily from measurements by 3 generations of Active Cavity Radiometer Irradiance Monitor) [*Scafetta and Willson*, 2009] and PMOD (from Physikalisch-Meteorologisches Observatorium Davos World Radiation Center) [*Froehlich*, 2006]. These composites, as well as the most recent TSI measurement (2003–2011) by the Total Irradiance Monitor (TIM) [*Kopp et al.*, 2005] aboard SORCE, are plotted in Fig. 3.3a. Despite quantitative differences between ACRIM and PMOD which may be due to uncorrected instrumental drifts [*Kopp and Lean*, 2011], both composites clearly demonstrate a prolonged solar min near the end of SC 23. SORCE TSI is annually averaged and the composites are smoothed to remove the short-term variability. The extracted SC signals in X_{OH} show excellent correlation with SORCE TSI (Fig. 3.3b) and generally follow the TSI composites (Fig. 3.3c), with some differences in the ascending phase of SC 23. While TSI is a good indicator of the integrated solar spectrum variability, short-wavelength UV radiation may vary differently from longer-wavelength radiation. Therefore, we also compare the observed X_{OH} variability with those in solar Lyman-α at 121.5 nm and the magnesium (Mg)-II index near 280 nm (composites from the Laboratory for Atmospheric and Space Physics and NOAA, respectively), which are proxies for solar UV variations. They both well correlate with the observed X_{OH} variability over SC 23 (Fig. 3.3d).

3.5. Model Results and Discussions

We simulated the SC modulation in X_{OH} with WACCM, a 3-D global atmospheric model extending from the surface to the lower thermosphere (2). The advantage of using WACCM is that chemistry, radiation, and dynamics are fully coupled, providing a comprehensive simulation of SC effects on X_{OH} at mid-latitudes. Four 50-year-long WACCM runs with different prescriptions of solar UV variability (to be described below) were carried out.

Most climate models with prescribed solar forcing use a parameterized solar spectral irradiance (SSI) variability developed at the Naval Research Laboratory (NRL), which is primarily based on space-borne UV measurements during 1991–2000 [*Lean et al.*, 1997]. Fig. 3.4a shows the simulated annual mean X_{OH} from 1964 to 2010 using this NRL solar forcing. TMF and MLS X_{OH} are represented by model OH integrated from the upper mesosphere down to 2.3 km and 25 km, respectively. The average SC signal in X_{OH} is only ~ 3% from max to min, suggesting differences of a factor of ~ 3 between model and observations (Fig. 3.4b). Note that another run with the standard WACCM SC setting (parameterized UV variability based on observations in previous solar cycles) shows similar results.

While the differences could be partially caused by limitations in our current understanding of middle atmospheric HO_x-O_3 chemistry, the uncertainty in solar UV variability could be a dominant source. Considering the significant difference between SOLSTICE and SIM SSI variability at 210–240 nm, we performed two WACCM runs using combined SSI variability from the two instruments, with cutoffs at 240 nm and 210 nm, respectively. Fig. 3.4c shows the annual mean model X_{OH} using SORCE SSI variability (SOLSTICE below 240 nm; SIM above 240 nm). The X_{OH} SC variability is ~ 6% (twice of that in Fig. 3.4b) and agrees much better with observations (10% for TMF; 7% for MLS); the difference between the WACCM result and TMF observations is reduced to a factor of ~ 1.5 (Fig. 3.4d). The other WACCM run using 240 nm as cutoff between SOLSTICE and SIM data gives a slightly larger X_{OH} variability of ~ 7%, reducing the difference between model and observations to a factor of ~ 1.3. Availability of longer

SORCE UV data covering the recent solar min (2008–2009) and the rising portion of SC 24 in the future are needed before we can draw more robust conclusions.

To better understand the detailed mechanism of OH response to SC, we use a 1-D photochemical model [*Allen et al.*, 1981; *Allen et al.*, 1984] to study the vertical and spectral distribution of OH sensitivity to SSI changes. It has the advantages of much higher computational efficiency and flexibility than WACCM, allowing for a wide range of sensitivity studies to elucidate the underlying mechanisms responsible for the OH response to SC. The spectral OH response, defined as the ratio of the relative change in model OH to the relative change in solar photon flux at the top of the atmosphere (%-[OH] / %-photon flux) highlights the important processes for OH photochemistry (Fig. 3.5a): (i) OH enhancements at 65–90 km and 50–80 km occur at Lyman-α and 170–200 nm, where direct H_2O photolysis is the major OH source. (ii) Positive OH responses at 210–320 nm correspond to enhanced O_3 photolysis followed by enhanced OH production through the reaction of $O(^1D)$ (from O_3 photolysis) with H_2O. (iii) Negative OH responses at above 80 km correspond to enhanced photolysis of O_2 (160–200 nm) and O_3 (255–290 nm), which produces atomic oxygen, a sink species for OH. This effect is insignificant in X_{OH} due to the very low OH abundance at these altitudes. (iv) Negative response at 190–220 nm below 40 km is caused by a shielding effect [*Mills et al.*, 2003] resulting from enhanced UV reduction by the enhanced overhead O_3 (O_3 at higher altitudes with a positive response to SC (5) absorbs more UV and diminishes the photolysis rates at lower altitudes). It mostly cancels out effect (ii) at these altitudes, leaving a small net negative response.

The vertical profile of model OH response to SC (Δ[OH]) (Fig. 3.5b) is obtained by convolving the spectral response in Fig. 3.5a with SSI variability (black line: using NRL; blue line: using SORCE). An earlier modeling work by *Canty and Minschwaner* [2002] (orange) using a solar forcing similar to that of NRL is close to our model result using NRL SSI. Such Δ[OH] is the overall OH change due to changes in photolysis and OH sources/sinks. Δ[OH] derived using SORCE SSI is generally larger than that using NRL, owing to the greater solar UV variability from SORCE. It is up to 18% at 70–80 km, near 5% at 40–60 km, and slightly negative at 30–40 km. In particular, by using SORCE SSI, OH SC signal increases by a factor of 2 at 40–60 km. The integrated X_{OH} response derived using NRL SSI is 3.7%; when SORCE SSI is used, the X_{OH} response increases to 6.4%. These values agree well with those from WACCM.

3.6 . Implications

Catalytic O_3 loss above ~ 40 km is primarily controlled by HO_x reactions [*McElroy and Salawitch*, 1989; *Osterman et al.*, 1997; *Salawitch et al.*, 2005]. O_3 in this region of the atmosphere is expected to show early signs of O_3 layer recovery [*Newchurch et al.*, 2003] and has a strong impact on global stratospheric temperatures, circulation, and thus climate [*Müller and Salawitch*, 1999]. Our findings of OH response to SC have important implications on the O_3 changes associated with HO_x variability. Previous studies on the O_3 response to SC [*Haigh et al.*, 2010; *Merkel et al.*, 2011; *Li et al.*, 2012; *Swartz et al.*, 2012] are for the overall O_3 change ($\Delta[O_3]$) including direct changes through photolysis, indirect changes through O_3-destroying catalysts (e.g., HO_x), and possible indirect changes through thermal structures and circulation. It is important to quantify the impact of each individual process. Here we discuss the component of $\Delta[O_3]$ that is solely due to $\Delta[OH]$ (denoted by $\partial[O_3]$). We made additional 1-D model runs by constraining $\Delta[OH]$ to values from the runs performed above using NRL and SORCE SSI and fixing UV flux (no other components of $\Delta[O_3]$). All species other than OH are allowed to vary until reaching steady state. The resultant O_3 change represents $\partial[O_3]$ (Fig. 3.5c). Above 60 km, $\partial[O_3] = \Delta[OH]$ holds approximately [*Canty and Minschwaner*, 2002]; The peak $\partial[O_3]$ at 75 km is –15% and–18% for the runs using $\Delta[OH]$ from NRL and SORCE SSI, respectively. Below 40 km, $\partial[O_3]$ is negligibly small. Between 40 and 60 km, using $\Delta[OH]$ from SORCE SSI instead of from NRL leads to nearly doubled $\partial[O_3]$. *Merkel et al.* [2011] showed that WACCM modeled $\Delta[O_3]$ at 40–60 km increases drastically from 0.5% to 1% when NRL SSI is replaced by SORCE SSI. Similar results are also obtained using other models [*Haigh et al.*, 2010; *Swartz et al.*, 2012]. These changes in $\Delta[O_3]$ at 40–60 km are close to that in $\partial[O_3]$ alone, suggesting that OH SC variability may be the dominant factor underlying the O_3

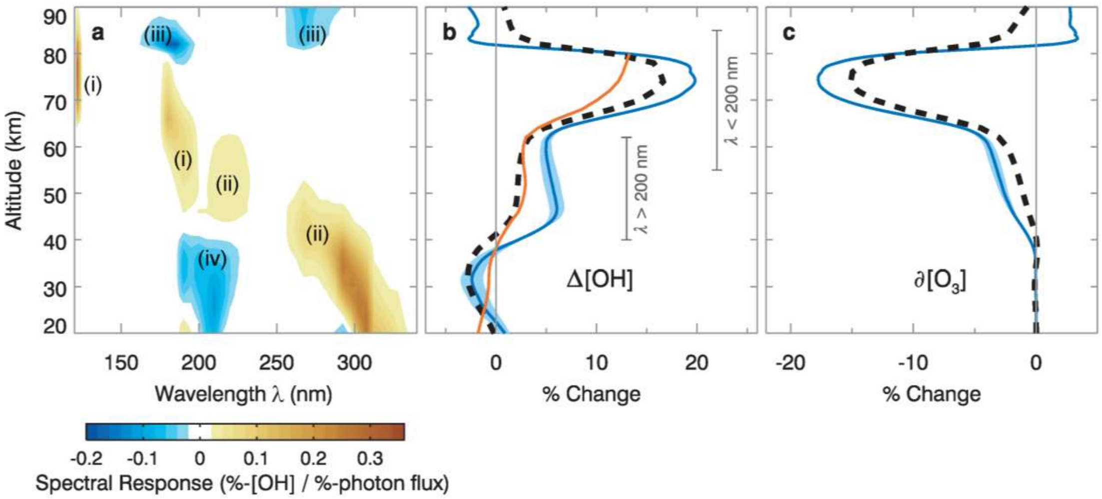

Fig. 3.5. Vertical profile of OH SC signal and its implications for O_3. (a) The spectral response of OH to changes in wavelength-resolved solar irradiance (the relative change in OH divided by the relative change in the photon flux) from the 1-D model. The reference UV spectrum for perturbation is constructed with SOLSTICE data below 210 nm, SIM data above 240 nm, and the mean of SOLSTICE and SIM at 210–240 nm where they disagree (see Fig. 3.4). (b) Vertical profiles of OH SC signal from the model run using NRL SSI (black), using SORCE SSI (blue; shade representing the upper and lower limits of results derived by using SOLSTICE or SIM data at 210–240 nm), and from *Canty and Minschwaner* [2002] (orange). (c) The corresponding O_3 variability [solely due to the changes in OH in panel (b)]

response to SC in the upper stratosphere. More quantitative diagnostic studies will help confirm it.

3.7. Concluding Remarks

Both 1-D and WACCM models using NRL SSI produce an X_{OH} response to SC that is much smaller than observed X_{OH} at TMF. The use of SORCE SSI gives results much closer to observations. Thus the uncertainty in SSI variability may be a primary limitation for accurate modeling of OH variability and the corresponding catalytic O_3 change. While the NRL model could have underestimated the solar forcing in SC 23, several other factors involving the trends in OH sources/sinks could have contributed to the larger observed OH variability.

One candidate is the trend in atmospheric H_2O [*Solomon et al.*, 2010]. Satellite and ground-based measurements revealed a decreasing trend of a few %/year in H_2O at 16–26 km during 2000–2005 [*Solomon et al.*, 2010; *Hurst et al.*, 2011]. Remsberg [2010] reported an increasing trend in mesospheric H_2O of ~ 1%/year at 60–80 km. We approximate the H_2O trend at 26–60 km by linear interpolation and simulated the impact of these trends on OH using the 1-D model (Fig. 3.6). The resultant change in X_{OH} is only –0.2%/year. The decreasing H_2O trend [*Hurst et al.*, 2011] has also stopped since 2005, suggesting little impact on the observed X_{OH} decrease during 2005–2009.

Similarly, a non-SC O_3 trend may also contribute to the observed X_{OH} change. A recent study using ground-based lidar measurement over TMF showed ~ 2%/decade O_3 trend at 35–45 km after 1997 [*Steinbrecht et al.*, 2006]. Unfortunately, there is no report of the trends at other altitudes. Assuming 2%/decade for all altitudes, our 1-D model suggests negligibly small change in X_{OH} of ~ 0.08%/decade.

Models using SORCE SSI variability produce an X_{OH} response (6~7%) that agrees much better with observed X_{OH} (~ 10% from FTUVS; ~ 7% from MLS). The remaining small difference is within the uncertainty range of TMF X_{OH}, and could also originate from the aforementioned small impacts of H_2O and O_3 trends. In addition, the SORCE SSI variability in this study is extrapolated from 2004–2007 back to the max of SC 23 in 2002, but the SSI in 2007 is expected to be slightly larger than the real SC min (2008–2009). This could also lead to a slightly underestimated OH SC signal from the model. Updated SORCE SSI data in the future could help to confirm this.

While models using SORCE SSI over SC 23 as solar forcing agree better with observations than those using NRL SSI, it is still too early to conclude that climate models should switch from NRL to SORCE SSI. Questions remain as to why previous SSI measurements during earlier SCs did not show such large variability, whether SORCE SSI variability is applicable to other SCs, and whether the difference is at least partially due to possible shortcomings in the NRL model and/or calibration issues of SORCE instruments.

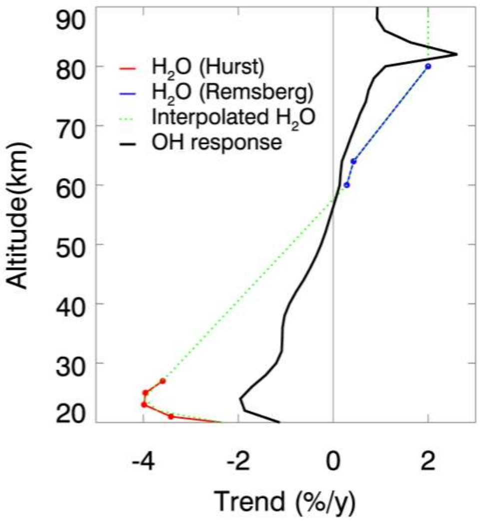

Fig. 3.6. Trend in H_2O and the corresponding OH change from 1-D model simulations. The color line shows the trend in H_2O, based on stratospheric trend during 2000–2005 from *Hurst* [2011], mesospheric trend from *Remsberg* [2010], and linear interpolation for other altitudes. The black line shows the 1-D model result of OH change in response to the H2O trend. Note that *Remsberg* [2010] also reported an SC-like decadal variability in mesospheric H2O, which we do not consider as a long-term trend to avoid counting the SC response twice. As a sanity check, our 1-D model can simulate such an SC-like decadal variability in mesospheric H_2O nicely.

In any case, continuous long-term observations of solar SSI, OH, O_3, and other related chemical species through the SC 24 are crucial for further investigations to solve the above puzzle. While MLS OH observations were temporarily suspended at the end of 2009 to prolong its remaining lifetime, a month-long measurement in each summer in the next few years is planned to cover the peak of SC 24. This unique dataset, in combination with the continuous ground-based FTUVS measurements, will provide valuable information about the global and vertical distribution of the SC signal in OH. The latter, with an accurately measured SSI variability, can rigorously test the photochemical mechanisms in current models.

PART II.

INTRASEASOANL VARIABILITY

Chapter 4. Review of MJO

Summary

The MJO is the most important mode of tropical intraseasonal variability and is a bridge between daily/weekly weather patterns and long-term climate variations. It is characterized by slow (~ 5 m/s) eastward propagation, and is strongest during boreal winters. Its evolution can be divided into eight phases described by the Real-time Multivariate MJO (RMM) index. Phase 1 represents an enhancement of convective anomalies over the Indian Ocean, which propagate eastward in the subsequent phases until they cross the International Dateline in Phase 8.

4.1. The Madden-Julian Oscillation (MJO)

Jon von Neumann wrote in 1955, on the extended range of weather predictions,

> "The approach is to try first short-range forecasts, then long-range forecasts of those properties of the circulation that can perpetuate themselves over arbitrarily long periods of time … finally to attempt forecast for medium-long time periods which are too long to treat by simple hydrodynamic theory and too short to treat by the general principle of equilibrium theory." [*von Neumann*, 1955]

Even after fifty years of advance in our knowledge in atmospheric science, von Neumann's assertion is still underway. Today, short-range forecasts would mean weather predictions extending out from days to about 1 week, and long-range forecasts would mean climate predictions extending from interannual (e.g., ENSO) to centennial time scales. In between are the medium-long time period forecasts, including tropical intraseasonal variability (TISV), which is less well understood. The most notable form of TISV is the Madden-Julian Oscillation (MJO; period 40–60 days).

Based on limited rawinsonde and surface station data in 1970s, *Madden and Julian* [1971; 1972] speculated that the MJO is characterized by slowly eastward-propagating (~ 5 m/s), large-scale oscillations in tropical convective cloudiness (and hence rainfall) over the equatorial Indian Ocean and western Pacific as the result of an eastward movement of large-scale atmospheric circulation cells oriented in the equatorial zonal plane. Evidence of such eastward propagating clouds in satellite data was first presented by *Gruber* [1974] and *Zangvil* [1975] who both found large-scale eastward propagating features with a period near 40–50 days at the equator in the cloud brightness data. The MJO is strongest over the warmest tropical waters in the equatorial Indian and western Pacific Oceans during boreal winter (November−April) when the Indo-Pacific warm pool is centered near the equator [*Madden and Julian*, 1971; 1972; *Zhang*, 2005; *Lau and Waliser*, 2011]. It impacts a wide range of phenomena and is predictable within 2–4 weeks. Numerous interactions between the MJO and other weather/climate processes have been described. These include the onsets and breaks of the Asian-Australian monsoon, the evolution of El Niño/La Niña and the character and strength of higher frequency tropical variability, the diurnal cycle, tropical cyclones, and extreme precipitation events. To date, our weather and climate models have a relatively poor representation of the MJO, and a comprehensive theory is still lacking [*Zhang*, 2005; *Waliser et al.*, 2009].

Schematic features of the MJO are illustrated in Fig. 4.1. In the equatorial Indian and western Pacific oceans an MJO event shows a large-scale, eastward-moving center of strong deep convection and precipitation (active phase), flanked by weak deep convection and precipitation in both east and west (suppressed phases). In association with the eastward-propagating equatorial convective cloud and rainfall system are strong variations in lower-level (typically at the 1.5 km or 850 hPa level) and upper-level (typically at the 13 km or 200 hPa level) large-scale atmospheric wind fields along the equator and in the subtropics. Unlike the convective cloudiness that is mostly confined

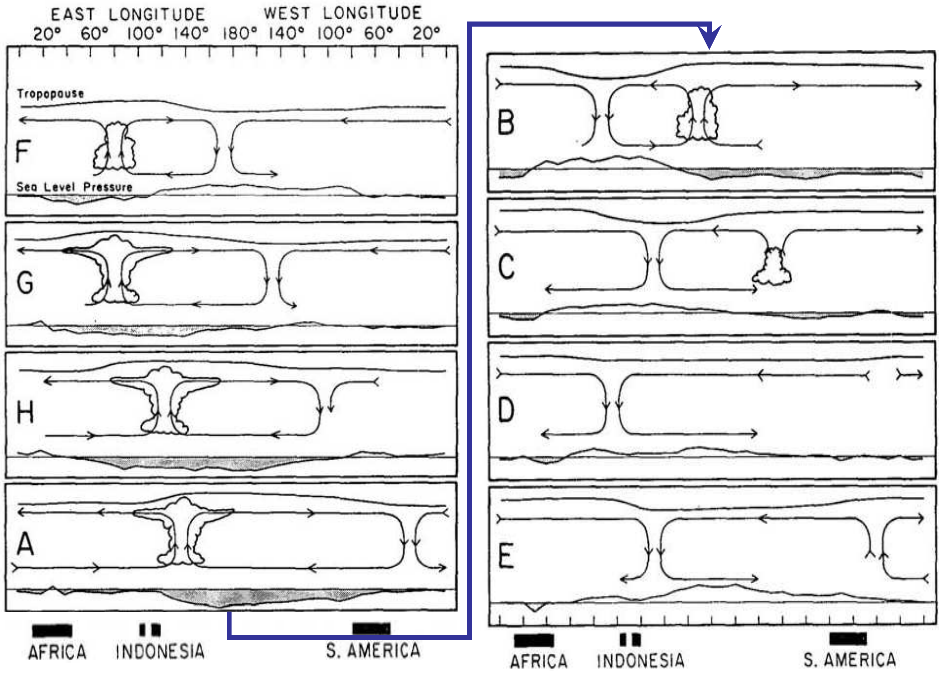

Fig. 4.1. Schematic propagation patterns of MJO. Adapted from *Madden and Julian* [1972].

over the equatorial Indian and western Pacific Oceans, the large-scale wind anomalies of the MJO extend globally along the equator and into the subtropics. For example, along the equator, low-level zonal winds converge into the convective center, while upper-level zonal winds diverge away from the convective center. These lower and upper-level zonal winds are interconnected through ascending (upward vertical movement) moist air within the convective center and descending dry air outside the convective center. These large-scale zonal winds propagate eastward together with the convective cloudiness along the equator and can reach into the western hemisphere (eastern Pacific, Atlantic, and Africa). In addition to these zonal winds along the equator are large-scale gyre circulations extending into the subtropics in both the lower- and upper- troposphere that are tied to the eastward-propagating convective cloudiness and zonal winds along the equator.

4.2. Mechanisms

During the MJO amplification (e.g., over the eastern Indian Ocean), convective heating anomalies are positively correlated with temperature anomalies. This implies production of eddy-available potential energy (EAPE), which can be used to drive atmospheric motion and sustain the MJO. When the MJO decays (e.g., over the eastern Pacific or east of the Date Line), temperature anomalies are nearly in quadrature with convective heating anomalies. As a result, the production of EAPE is small and no longer supplies energy for the MJO [*Hendon and Salby*, 1994]. For water vapor, the composite evolution of moisture shows markedly different vertical structures as a function of longitude. There is a clear westward tilt with the height of the moisture maximum associated with the MJO propagating eastward across the Indian Ocean. These disturbances evolve into nearly vertically uniform moist anomalies as they reach the western Pacific. Near-surface (below 850 hPa) positive water vapor anomalies were observed to lead the convection anomaly by 5 days over the Indian Ocean and western Pacific. Upper-level positive water vapor anomalies were observed to lag the peak in the convection anomaly by 5–10 days, as the upper troposphere is moistened following intense convection. In the eastern Pacific, the moisture variations then become confined to the lower levels (below 700 hPa), with upper-level water vapor nearly out of phase [*Tian et al.*, 2010].

In the Indo-Pacific warm pool, the temperature anomaly exhibits a tri-modal vertical structure: a warm anomaly in the free troposphere (800–250 hPa) and a cold anomaly near the tropopause (above 250 hPa) and in the lower troposphere (below 800 hPa) for the wet phase. The moisture anomaly also shows markedly different vertical structures as a function of longitude and the strength of the convection anomaly. Most significantly, over the Indian Ocean and western Pacific, enhanced convection and precipitation is generally preceded in both time and space by a low-level warm and moist anomaly and followed by a low-level cold and dry anomaly. This zonal asymmetry in the low-level moisture and temperature anomaly provides a favorable moist thermodynamic condition for the eastward propagation of the MJO [*Tian et al.*, 2010]. During the dry phase of the MJO, suppressed convection is associated with decreased cloud cover, increased surface insolation, and anomalous surface easterlies. These anomalous surface easterlies act to decrease the surface wind speed because the background surface winds are weak westerlies in the equatorial Indian/western Pacific Oceans, hence decreasing

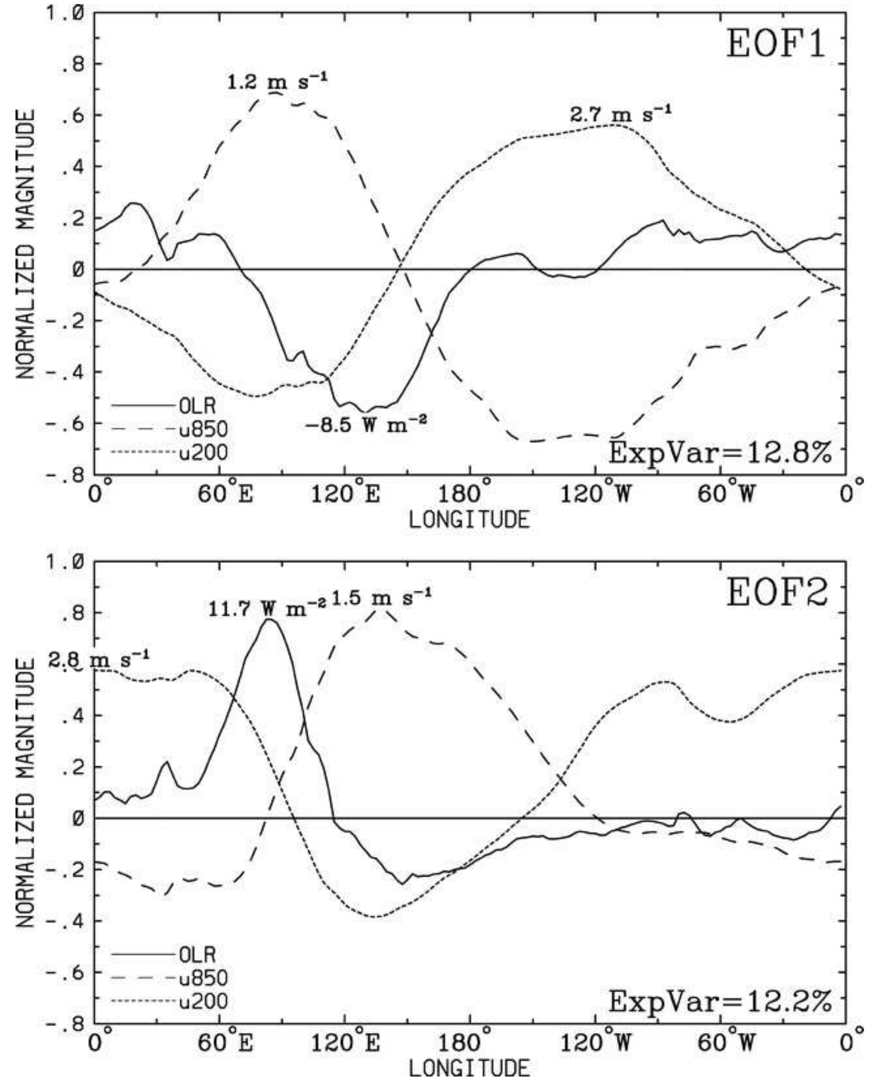

Fig. 4.2. The leading EOFs of the combined OLR, u_{850}, and u_{200}. Extracted from Fig. 1 of *Wheeler and Hendon* [2004].

the surface latent heat flux (or evaporation). Increased surface shortwave radiation and reduced surface evaporation contribute to the warming of SST for the dry phase. During the subsequent wet phase of the MJO, enhanced convection is associated with increased cloud cover and decreased surface insolation. As a result, the SST warming trend is arrested and a cooling trend is initiated. Subsequently, the continued cooling of the upper ocean is accelerated by increased westerly surface winds leading to enhanced surface evaporation and increased entrainment of cold water from below the thermocline. Then the wet phase is followed by another dry phase when SST warming occurs. Therefore, over the Indian Ocean and western Pacific, the enhanced convection is usually led by a warm SST anomaly to the east due to enhanced insolation and decreased evaporation, and followed by a cold SST anomaly to the west due to decreased insolation and enhanced evaporation. When the convective anomaly approaches the Date Line, the surface evaporation anomaly and surface solar radiation anomaly tend to cancel each other. Thus, the SST anomaly is rather small over the eastern Pacific, as is the convective anomaly. This convection-SST phase relationship leads many scientists to believe that the MJO is a coupled mode of the tropical ocean atmosphere system [*Hendon and Glick*, 1997; *Wang and Xie*, 1998].

4.3. The RMM Index

To study the evolution of MJO, a training index is needed to define different stages of the MJO development. The phases of MJO have been quantitatively defined through the All-season Real-time Multivariate MJO (RMM) Index [*Wheeler and Hendon*, 2004]. The RMM index consists of a pair of principle component time series, called RMM_1 and RMM_2, which are the projection of the daily observed NOAA outgoing longwave radiation (OLR) and NCEP/NCAR re-analysis and/or Australian Bureau of Meteorology Research Center Global Analysis and Prediction (GASP) analysis 850 and 200 hPa zonal winds, with the annual cycle and components of interannual variability removed, on a pair of multiple-variable EOFs. Two such EOFs are the leading pair of EOFs of the combined daily intraseasonal filtered fields of near-equatorially averaged (15°S−15°N) NOAA OLR and NCEP/NCAR 850 and 200 hPa zonal winds for all seasons from 1979 to 2001 (23 years) and describe the key features of MJO. The spatial structures of the two EOFs are shown in Fig. 4.2. The leading EOF structure accounts for 12.8% of the total variance of the three combined fields. It has a region of negative OLR anomalies, indicating enhanced atmospheric deep convection, between about 80°E and the date line. The 850-hPa level winds show westerly anomalies to the west of the main centre of convection, and

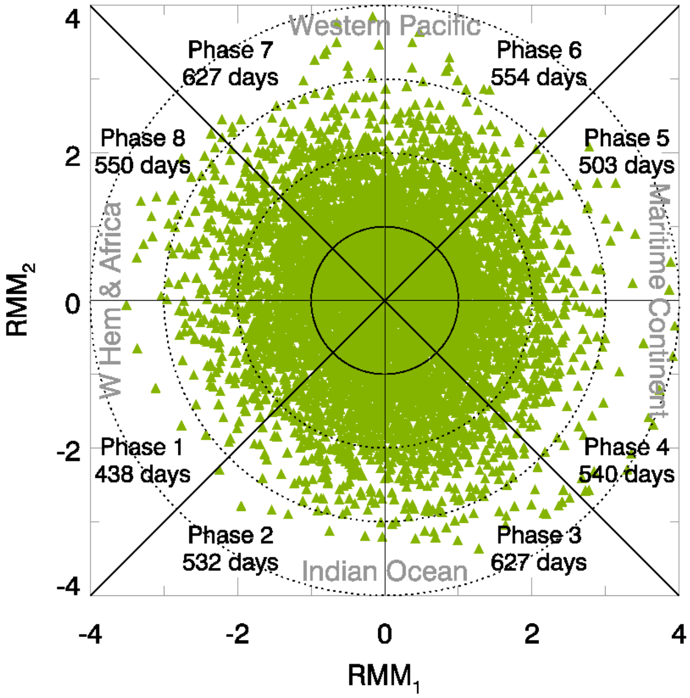

Fig. 4.3. The RMM index during boreal winters of November 1974–April 2012. Each phase is characterized by enhancement of convection at particular regions.

easterlies to the east, with the 200-hPa wind anomalies being close to the opposite. The pattern thus describes a large vertically-oriented circulation cell along the equator with upward motion being implied in the region of negative OLR anomalies, and downward motion outside that region. The second EOF structure, on the other hand, accounts for 12.2% of the total variance, with it being approximately in quadrature with the first. Together the EOFs form a degenerate pair, and they can represent the spatially propagating signal of the MJO.

Using the RMM index, the MJO lifecycle has been divided into eight phases. Phase 1 represents developing positive rainfall anomalies in the western Indian Ocean, with sequential progression to Phase 8 corresponding to the eastward propagation of positive rainfall anomalies across the eastern Indian Ocean, Maritime Continent, western Pacific, and onto the central/eastern Pacific Ocean [*Hendon and Salby*, 1994]. Fig. 4.3 shows the (RMM_1, RMM_2) phase space for all days in boreal winter from 2002 to 2010 and the number of days for each phase of the composite MJO cycle. The RMM index can be obtained from (http://www.cawcr.gov.au/bmrc/clfor/cfstaff/matw/maproom/RMM/).

Chapter 5.

Vertical Structure of MJO-Related Subtropical O_3 Variations[‡]

Summary

The vertical structure of MJO-related subtropical O_3 variations has been investigated using the vertical O_3 profiles from the Aura Microwave Limb Sounder (MLS) and Tropospheric Emission Spectrometer (TES), as well as *in situ* measurements by the Southern Hemisphere Additional Ozonesondes (SHADOZ) project. The subtropical O_3 anomalies maximize approximately in the lower stratosphere (60–100 hPa). The spatial-temporal patterns of the subtropical O_3 anomalies in the lower stratosphere are very similar to that of the total column. In particular, they are both dynamically driven by the vertical movement of subtropical tropopause. The subtropical partial O_3 column anomalies between 30–200 hPa account for more than 50% of the total O_3 column anomalies. TES measurements show that at most 30% of the total O_3 column anomalies are contributed by the tropospheric components. This indicates that the subtropical total column O_3 anomalies are mostly from the O_3 anomalies in the lower stratosphere, which supports the hypothesis of *Tian et al.* [2007]. The strong connection between the intraseasonal subtropical stratospheric O_3 variations and the MJO implies that the stratospheric O_3 variations may be predictable with similar lead times over the subtropics. Future work could involve a similar

---

[‡] Published in Li, K.-F., et al. (2012), Vertical structure of MJO-related subtropical ozone variations from MLS, TES, and SHADOZ data, *Atmos. Chem. Phys.*, *12*, 425−436, doi:10.5194/acp-12-425-2012.

study or an O_3 budget analysis using a sophisticated chemical transport model in the near-equatorial regions where the observed MJO signals of total column O_3 are weak.

5.1. Motivation

Tian et al. [2007] documented the spatial and temporal patterns of the tropical total column O_3 (TCO) in connection with large-scale MJO convection and circulation anomalies. It was found from the measurements of the Total Ozone Mapping Spectrometer (TOMS) [*Stolarski and Frith*, 2006] and the Atmospheric Infrared Sounder (AIRS) [*Chahine et al.*, 2006] that the total column O_3 anomalies of 5–10 DU are mainly evident over the subtropics in the Pacific Ocean and the eastern hemisphere. The subtropical positive (negative) total column O_3 anomalies flank or lie to the west of equatorial suppressed (enhanced) MJO convection and propagate slowly eastward (~ 5 m/s). The subtropical TCO anomalies are typically collocated with the subtropical upper-tropospheric cyclones/anticyclones and are anti-correlated with geopotential height anomalies near the tropopause. They therefore asserted that that the subtropical TCO are dynamically driven by the vertical movement of the subtropical tropopause layer and mainly associated with the O_3 variability in the stratosphere rather the troposphere. However, they were limited by the TCO observations. To verify their assertion, there is a need to investigate the vertical structure of O_3 variation.

A number of additional studies have examined vertical structure of O_3 variation in the upper troposphere and lower stratosphere that may be related to the MJO. Based on ozonesonde data in Indonesia, *Fujiwara et al.* [1998] suggested that the upper tropospheric ozone enhancement is tied to the passage of Kelvin waves and the MJO. In studying an “Ozone Mini-Hole” (OMH) event over the Tibetan Plateau during December 2003, *Liu et al.* [2009] found that the majority of ozone reduction of that OMH event was located in the upper troposphere and lower stratosphere, based on the Michelson Interferometer for Passive Atmospheric Sounding (MIPAS) [*Cortesi et al.*, 2007] and Global Ozone Monitoring by Occultation of Stars (GOMOS) [*Kyrölä et al.*, 2004] ozone profile data. Further analysis indicates that this ozone reduction in the upper troposphere and lower stratosphere is a result of the uplift of the tropopause by the upper-tropospheric anticyclone over the Tibetan Plateau induced by an MJO event over the equatorial Indian Ocean and western Pacific. A recent work of [*Weare*, 2010] also found significant stratospheric ozone variations associated with MJO using ERA-40 reanalysis ozone data. These results appear to be consistent with *Tian et al.*, [2007] that the subtropical intraseasonal total column O_3 anomalies are mainly associated with vertical movement of subtropical tropopause. To further understand the relative contribution of O_3 from different atmospheric layers, especially stratosphere versus troposphere, to the subtropical total column O_3 anomalies, we use contemporary satellite observations and *in situ* measurements to investigate the vertical structure of subtropical O_3 variations related to the MJO. In particular, we use vertical O_3 profiles derived from the Earth Observing System (EOS) Microwave Limb Sounder (MLS) and Tropospheric Emission Spectrometer (TES) on Aura satellite and measured *in situ* by the Southern Hemisphere Additional Ozonesondes (SHADOZ) project.

5.2. Data and Methods

The v2.2 O_3 product [*Livesey et al.*, 2008] from the EOS MLS measurement from November 1, 2004−February 6, 2010, will be used. The MLS instrument [*Waters et al.*, 2006] was launched in 2004 on the NASA Aura satellite into a sun-synchronous near-polar orbit with equatorial crossing times of 01:43 and 13:43 local solar time. The MLS O_3 product is retrieved from observations of atmospheric thermal emission near 240 GHz using a limb-viewing geometry. Profiles are retrieved every 165 km along the sub-orbital track on 6 levels per decade of pressure from 215 hPa through the stratosphere, with vertical resolution of ~ 3 km in the upper troposphere. These profiles have been screened per the MLS data quality document [*Livesey et al.*, 2007] and gridded by averaging data over 5° longitude × 4° latitude into daily values. With this gridding resolution the global coverage is completed in ~ 1 week. No criterion has been applied to select the line of sight angles or the solar zenith angles. Given the relatively long wavelengths of MLS observations, retrievals are negligibly perturbed by many clouds that strongly perturb

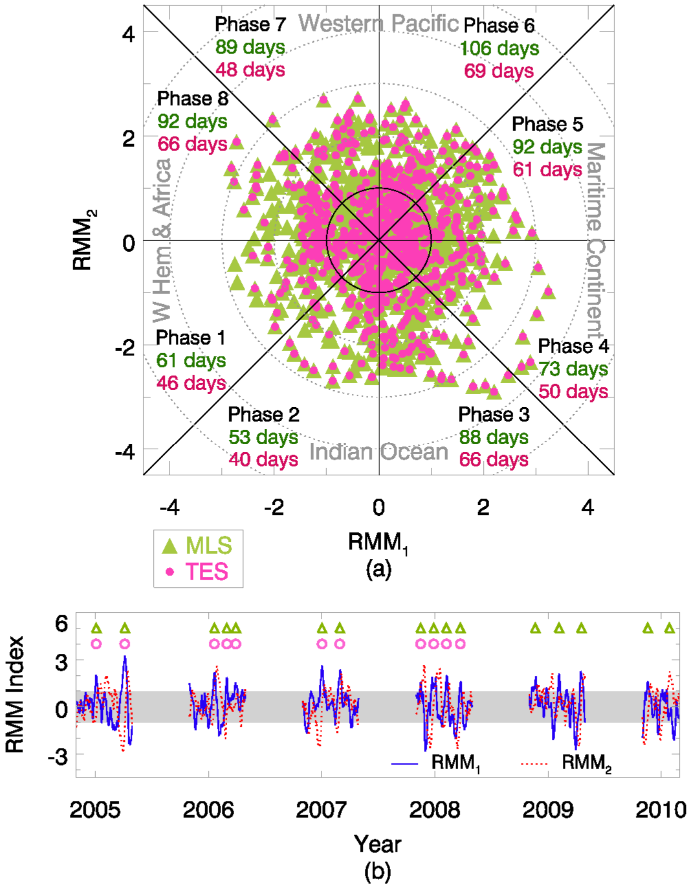

Fig. 5.1. (a) The number of days constituting each MJO phase during the observational periods of interest. Only days with strong MJO activity ($RMM_1^2 + RMM_2^2 \geq 1$) are considered. The green triangles represent days with MLS O_3 observations during the boreal winters (November – April) of November 2004–February 2010; the red dots represent days with TES O_3 observations during the boreal winters of September 2004–August 2008. (b) The time series of RMM indices. The strong MJO events during the observational periods are denoted by the triangles and circles for MLS and TES, respectively. The indices lying in the grey region are considered to be weak MJO events and are ignored in the analysis.

observations at infrared and visible wavelengths. Recommended screening is generally successful in removing v2.2 profiles that are significantly impacted by scattering from large ice particles in convective cores [*Schwartz et al.*, 2008].

The Level-2 (L2) O_3 profiles measured by TES from September 20, 2004, to August 18, 2008, [*Beer et al.*, 2001; *Jourdain et al.*, 2007; *Worden et al.*, 2007] are also used in this study. TES is an infrared Fourier-transform spectrometer also aboard the Aura satellite, covering the spectral range 650–3050 cm^{-1} (3.3–15.4 μm) [*Beer*, 2006]. It has a high spectral resolution at 0.025–0.1 cm^{-1} and a horizontal swath footprint of 5.3 km × 0.53 km. O_3 profiles are retrieved from the infrared channels covering the O_3 ν_3 band (1050 cm^{-1} or 9.6 μm) using a nonlinear optimal estimation algorithm [*Rodgers*, 2000; *Worden et al.*, 2004; *Bowman et al.*, 2006] on 67 pressure levels between the surface and 5 hPa, with a vertical spacing of ~ 0.7 km below 10 hPa. These infrared channels are most sensitive to O_3 at levels between 900 and 30 hPa with a vertical resolution of 6 km for clear sky scenes. The retrieved TES tropospheric O_3 profiles have been validated with SHADOZ

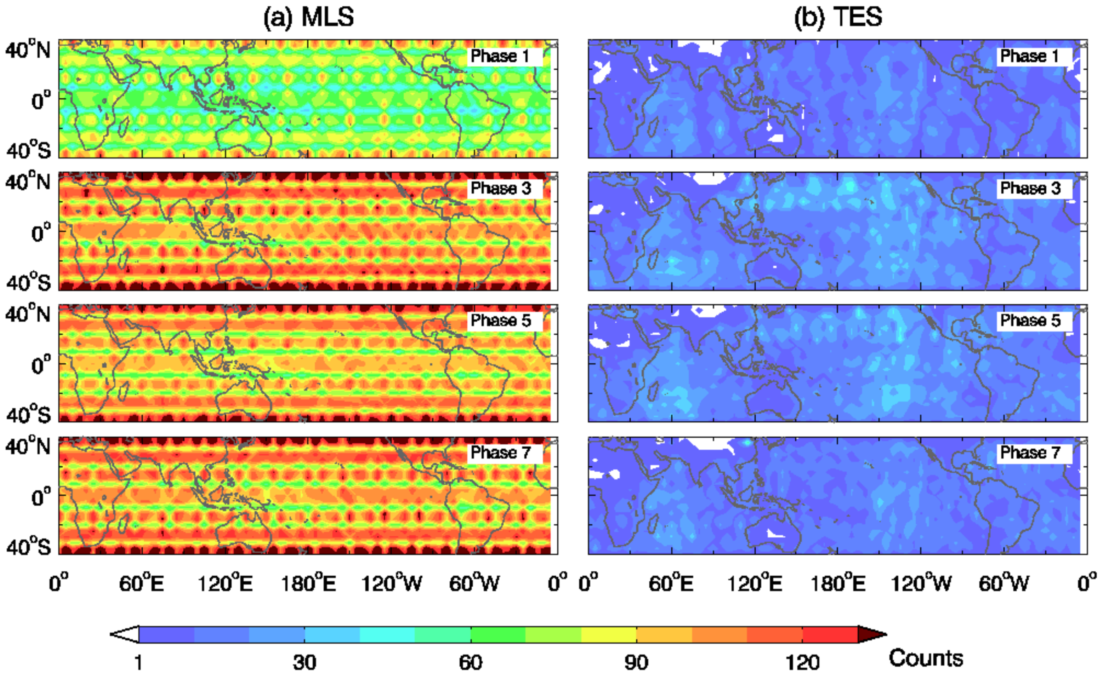

Fig. 5.2. Number of MLS/TES soundings in each MJO phase during the observational periods of interest. The patterns of MLS statistics in Panel (a) appear to be discretized in space because the MLS profiles are retrieved every 165 km along the sub-orbital track, which is approximately 1.5° latitude in the equatorial region.

ozonesonde measurements [*Worden et al.*, 2007]. When and where there are optically thick clouds, the TES-retrieved O_3 profiles below the optically thick clouds comes mainly from the a priori O_3 profile, because the retrieved O_3 information below the cloud tops can be very low [*Kulawik et al.*, 2006; *Eldering et al.*, 2008]. For this study, the TES swath O_3 data were binned into the same 5°-longitude × 4°-latitude grid boxes of MLS described above. The global coverage is completed also in ~ 1 week at this gridding resolution. The number of individual retrievals being averaged in each grid box is recorded and served as weighting in the MJO-composite averaging.

To compare the MJO modulations in O_3 as observed by MLS and TES, we also study the MJO modulations in the Level-3 (L3) total column O_3 data derived from the Ozone Monitoring Instrument (OMI) [*Levelt et al.*, 2006a] aboard Aura during November 1, 2004–February 28, 2010. OMI is an extension of the TOMS instrument. Total column O_3 are retrieved from OMI radiances in the spectral region 307–332 nm and 359–361 nm [*Levelt et al.*, 2006b]. The original OMI O_3 column has been averaged daily into 0.25° longitude × 0.25° latitude grid boxes. As for TES, we regridded the daily data into the same 5° longitude × 4° latitude grid boxes of MLS.

The SHADOZ project [*Thompson et al.*, 2004; *Thompson et al.*, 2007] has collected

Table 5.1. Datasets used in this work. MLS Level-2 (L2) v2.2 O_3 and TES L2 O_3 are swaths products. They have been regridded into 5°-longitude × 4°-latitude daily products in this work. OMI Level-3 (L3) O3 and TRMM 3B42 rainfall has also been regridded into 5°-longitude × 4°-latitude and 2.5°-longitude × 2°-latitude daily products, respectively, in this work (see text). Fiji is located at (178.40°E, 18.13°S).

Name	Time Span (DD/MM/YYYY)	Original Resolution	Reprocessed Resolution
MLS L2 O_3	01/11/2004–06/02/2010	Swath	Daily, 5° lon × 4° lat
TES L2 O_3	20/09/2004–18/08/2008	Swath	Daily, 5° lon × 4° lat
OMI L3 O_3	01/11/2004–28/02/2010	Gridded daily, 0.25° lon × 0.25° lat	Daily, 5° lon × 4° lat
SHADOZ O_3 over Fiji	01/01/1998–31/12/2008	Weekly/biweekly	–
TRMM 3B42 rainfall	01/11/2004–28/02/2010	Gridded 3-hourly, 0.25° lon × 0.25° lat	Daily, 2.5° lon × 2° lat
ERA-Interim GPH_{150}	01/11/2004–31/01/2010	Gridded 3-hourly, 1.25° lon × 1.25° lat	–

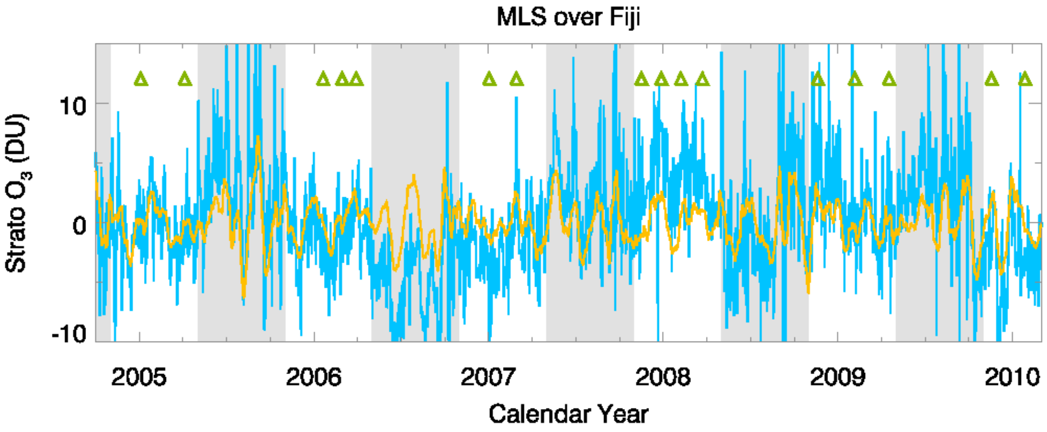

Fig. 5.3. The deseasonalized (cyan) and the bandpassed (orange) time series over Fiji observed by MLS. The grey shades are the boreal summer seasons (May–August), when data have been ignored in the MJO phase averages. The strong MJO events during the observational periods are denoted by the triangles for MLS as in Fig. 5.1(b).

over several thousand vertical O_3 profiles from the troposphere to the middle stratosphere since 1998 from 14 tropical and subtropical sites using balloon-borne electrochemical concentration cell (ECC) ozonesondes. Among all the SHADOZ sites, Fiji (178.40°E, 18.13°S) is the best site for this work because the data there are available from January 1998 to December 2008 between the surface and the mid-stratosphere (~ 20 hPa), and it lies in an area that was found to have strong MJO-driven total O_3 variability [*Tian et al.*, 2007].

To indicate the spatial patterns and propagation characteristics of the equatorial convective anomalies associated with the MJO, we use Tropical Rainfall Measuring Mission (TRMM) 3B42 rainfall data from November 1, 2004, to February 28, 2010. The TRMM 3B42 rainfall data are estimated from multiple satellites as well as gauge analyses, where feasible, at fine scales (0.25° × 0.25° and 3 hourly) [*Huffman et al.*, 2007]. For this work, the rainfall data are averaged daily on 2.5° longitude × 2.0° latitude grids. To indicate the vertical movements of the subtropical tropopause related to the MJO, the 150 hPa geopotential height (GPH_{150}) from the European Centre for Medium-range Weather Forecasting (ECMWF) Interim reanalysis product (ERA-Interim) [*Dee et al.*, 2011] from

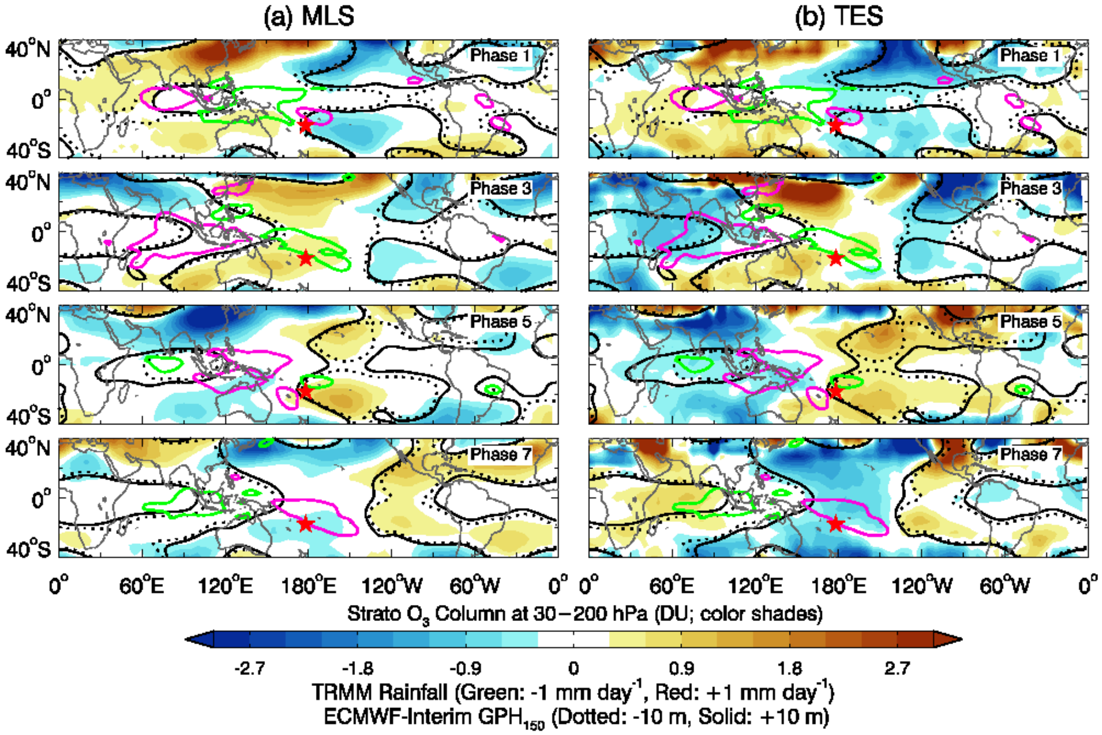

Fig. 5.4. MJO-related stratospheric O_3 anomalies integrated between 30--200 hPa in color shades derived from (a) MLS and (b) TES. For simplicity, only MJO phases 1, 3, 5, and 7 are plotted with a 1-2-1 running average applied (see text). Furthermore, a 20°-longitude × 10°-latitude spatial running average has been applied to remove high wavenumber fluctuations of O_3 anomalies. The MJO-related rainfall anomalies are overlaid as red (+1 mm day^{-1}) and green (−1 mm day^{-1}) solid contours with a 10°-longitude × 6°-latitude spatial running average applied. The MJO-related 150 hPa geopotential height (GPH_{150}) anomalies are shown as solid (+10 m) and dotted (−10 m) black contours with a 9°-longitude × 6°-latitude spatial running average applied. The location of Fiji (178.4°E, 18.13°S) is represented by (★).

November 1, 2004 to January 31, 2010, is used. No post-process has been applied to the GPH_{150} data. We summarize the properties of the above datasets in Table 5.1.

To capture the MJO signal in the O_3 data, a running-average band-pass filter for 15–90 days is first applied to the time series. Then, to identify MJO events for producing a composite analysis, the RMM daily index is used. Composite MJO cycles of interested quantities, such as rainfall, O_3, and geopotential height, are produced by separately averaging together all daily values of the given quantity for each phase of the MJO, considering only strong amplitude events where $RMM_1^2 + RMM_2^2 \geq 1$. This compositing procedure, or closely analogous ones, has become a common methodology for examining impacts associated with the MJO [*Tian et al.*, 2010, and references therein].

Since the MJO is strongest during boreal winters (November–April) when the influence from the Asian monsoon is minimal [*Zhang and Dong*, 2004], we are only interested in the MJO events during this season. During November 2004–February 2010 when the MLS O_3 measurements are used in this work, there are ~ 16 strong MJO events during boreal winters, which constitute 53–106 days in each of the 8 phases (Fig. 5.1, green triangles). As a result, a total of 50–120 MLS soundings are averaged in the grid boxes for each phase (Fig. 5.2a). Similarly, during November 2004–February 2008 when the TES O_3 measurements are used in this work, there are ~ 11 strong MJO events during boreal winters, which constitute 53–106 days in each of the 8 phases (Fig. 5.1, pink dots). Because TES has much lower horizontal resolution, only a total of 10–30 TES soundings are averaged in the grid boxes for each phase (Fig. 5.2b).

5.3. Results and Discussions

To examine the MJO variability of the stratospheric O_3, the O_3 anomalies associated with the MJO are integrated from 30–200 hPa to give the “stratospheric” column anomalies. It should be noted that for TES, the averaging kernels near 200 hPa might have a significant tropospheric component in the tropics and subtropics. This may give rise to some of the differences between TES and MLS. An alternative would be to use 100 ppb O_3 to determine the bottom level for the stratospheric column. For simplicity and a qualitative investigation, we adopt the former definition in this work.

The intraseasonal variability in stratospheric column O_3 can be seen from the seasonal anomalies. As an example, Fig. 5.3 shows the deseasonalized (cyan) time series over Fiji observed by MLS. The MLS O_3 anomalies are obtained by averaging the swath footprints that fall into the 10° longitude × 8° latitude box centered at Fiji. MLS has almost

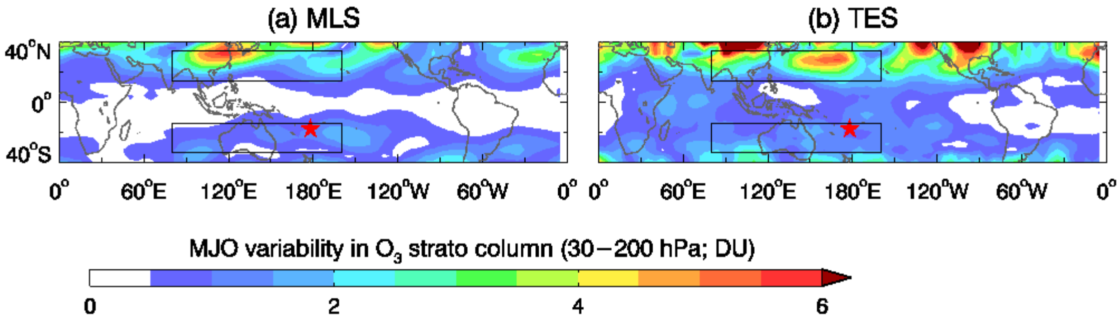

Fig. 5.5. The MJO variability in O_3 columns derived from MLS and TES observations. The variability is defined as 2 standard deviations of the MJO cycle (see text). The location of Fiji (178.4°E, 18.13°S) is represented by (★). The rectangular boxes enclose representative subtropical regions (80°E–200°E, 14°N/S–34°N/S) where the MJO modulations are largest.

daily coverage over the enclosed region. The orange line is the bandpassed time series, which resembles the intraseasonal variability in the raw time series.

By averaging over individual MJO phases during boreal winters, the spatial patterns of the MJO-modulation in the stratospheric O_3 columns for MLS and TES are obtained and they are shown in Fig. 5.4a and b, respectively (color shades). For brevity, only MJO phases 1, 3, 5, and 7 are plotted; and for clarity a 1-2-1 running average over MJO phase is applied. For example, the Phase 1 map shown is an average of phases 8, 1 (doubly counted), and 2. Furthermore, a 20° longitude × 10° latitude spatial running average has been applied to remove high wavenumber fluctuations of O_3 anomalies. To illustrate the convective activities, the MJO-composite rainfall anomalies are overlaid as red and green solid contours with a 10°longitude × 6°latitude spatial running average applied. The propagation pattern of rainfall is consistent with those delineated in previous studies using the extended empirical orthogonal functions (EEOF) [*Waliser et al.*, 2005; *Tian et al.*, 2007]. Therefore, we expect that the MJO patterns obtained from EEOF and MEOF will be similar [*Tian et al.*, 2010]. The MJO-composite GPH_{150} anomalies are shown as solid and dotted black contours with a 9° longitude × 6° latitude spatial running average applied.

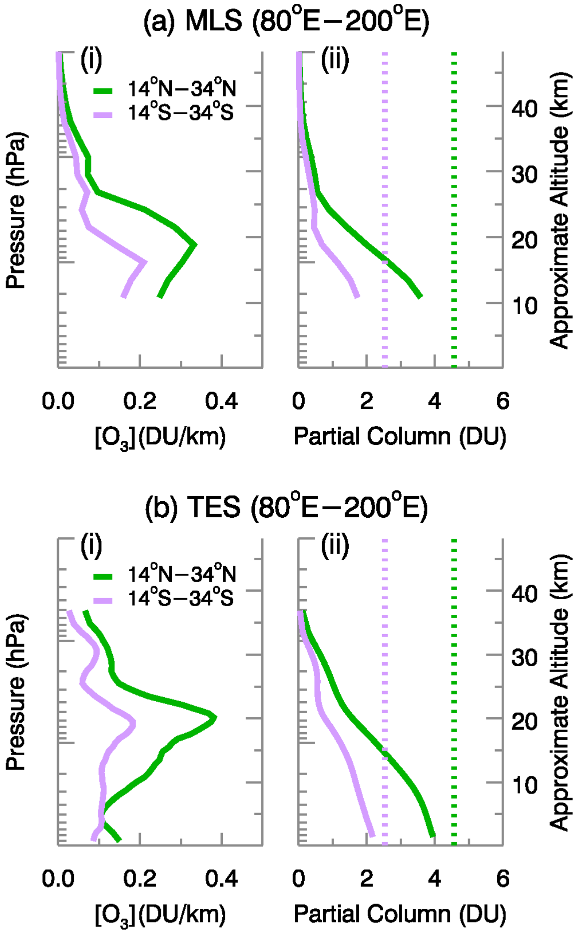

Fig. 5.6. (a)(i) Regional MJO variability of O_3 concentration (in unit of DU km^{-1}) derived from MLS measurements in regions (80°E–200°E, 14°N/S–30°N/S), which are enclosed by the rectangular boxes in Fig. 5.5. As in Fig. 5.5, the variability is defined as 2 standard deviations of the MJO cycle; (a)(ii) Regional MJO variability of partial O_3 columns integrated from 30 hPa to pressure levels below. (b) Same as (a) except for TES.

Tian et al. [2007] examined the MJO in TOMS and AIRS total O_3 columns using EEOF (see their Figs. 1 and 2). Their Lag –2 (+4) corresponds roughly to our Phase 1 (7). In general, the spatial-temporal patterns of the stratospheric O_3 column anomalies of the MJO composites for MLS and TES are similar to those in total O_3 of TOMS and AIRS. During Phase 1 (Lag –2), enhanced convection, as indicated by positive rainfall anomalies is found in the western equatorial Indian Ocean. In contrast, suppressed convection, as indicated by negative rainfall anomalies, resides over the equatorial Indo-Pacific Warm

Pool. As a result, upper-tropospheric cyclonic gyres are formed over Asia and the western Pacific on the northern subtropics as well as the eastern Indian Ocean and Australia on the southern subtropics, both on the west side of the equatorial suppressed convection [*Hendon and Salby*, 1994]. These subtropical cyclones induce downward movements of subtropical tropopause, as indicated by negative GPH_{150} anomalies. Thus, both MLS and TES show positive stratospheric O_3 column anomalies (a few Dobson units; c.f. Fig. 5.5) over these subtropical regions. During Phase 3 (Lag 0), the enhanced convection becomes stronger and wider and it moves to the eastern equatorial Indian Ocean and Maritime Continent, and the suppressed convection becomes weaker and narrower and it moves to the South Pacific Convergence Zone (SPCZ). As a result, upper-tropospheric anticyclonic gyres are formed over the Middle East on the northern subtropics as well as the southern subtropical Africa, both on the west side of the equatorial-enhanced convection. They induce upward movements of subtropical tropopause, as indicated by positive GPH_{150} anomalies and negative stratospheric O_3 column anomalies over these subtropical regions as shown by both MLS and TES. Phases 5 and 7 (Lag +2 and Lag +4) are very similar to Phases 1 and 3, respectively, except for an opposite sign. These spatial patterns of rainfall, GPH_{150} and O_3 anomalies move eastward with a speed of ~ 5 m/s from Phases 1 to 7. The subtropical stratospheric O_3 column anomalies for $14° \leq |\text{latitudes}| \leq 34°$ are moderately anti-correlated with the subtropical GPH_{150} anomalies in both MLS and TES with linear correlation coefficients of –0.75 for MLS and –0.60 for TES, respectively.

The MJO variability of stratospheric O_3 at the grid points derived from MLS and TES O_3 observations are shown in Fig. 5.5. It is defined as two standard deviations of the 8-phase MJO cycles in the enclosed regions, which roughly equates the amplitude of the MJO cycle. For both observations, the MJO variability at the subtropical regions ($|\text{latitudes}| > 15°$) is larger than those in the deep tropics ($|\text{latitudes}| \leq 15°$). In the northern subtropics, the MJO variability is generally 5–8 DU near the Indo-Pacific region, whereas in the southern subtropics, it is 1–2 DU. In other words, the MJO variability in the northern subtropics is generally a factor of 2–4 larger than those in the southern subtropics. This north-south gradient is also evident in the TOMS column O_3 data reported in *Tian et al.* [2007]. As will be discussed below, this gradient is also found in the recent OMI column

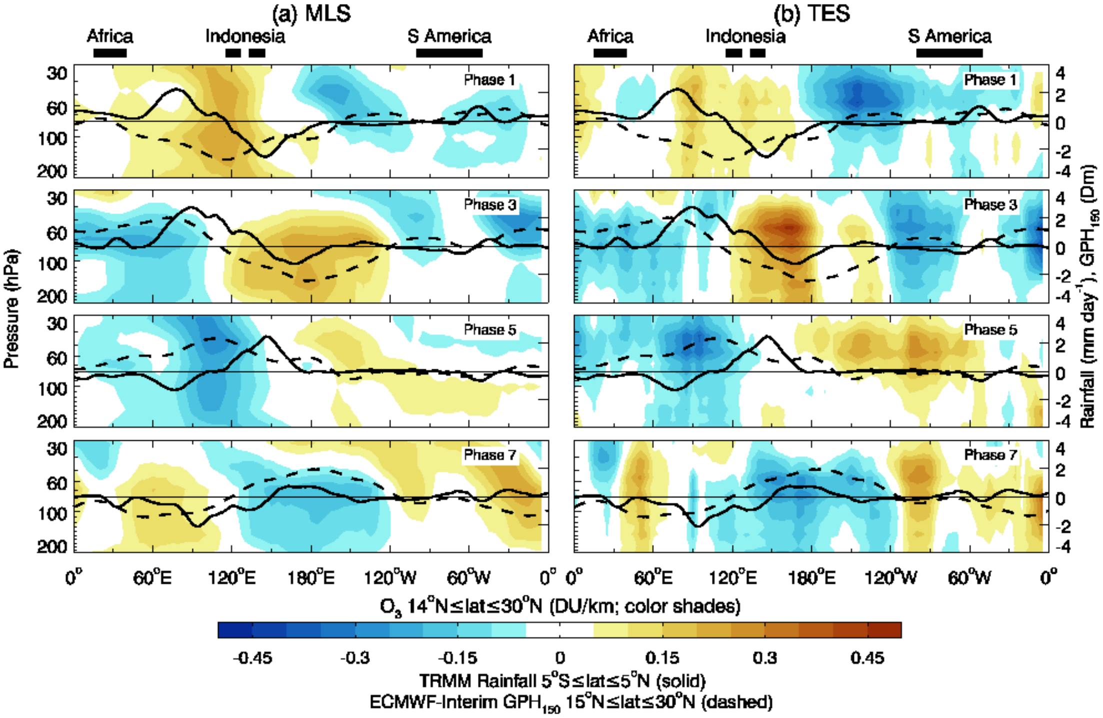

Fig. 5.7. Pressure-longitude cross sections of the MJO-related O_3 anomalies in the northern subtropics averaged between 14°N and 30°N from both MLS (a) and TES (b) . A 20°-longitude spatial running average has been applied to remove high-wavenumber fluctuations. Solid lines denote the MJO-related TRMM rainfall anomalies averaged between 5°S and 5°N. Dashed lines represent the MJO-related ERA-Interim GPH_{150} anomalies averaged between 15°N and 30°N in unit of decameters (1 Dm = 10 m).

O_3 data. The MJO variability in the deep tropics as observed by TES (~ 1 DU) is slightly larger than that as observed by MLS (< 0.5 DU). This may be partly due to the fact that TES O_3 concentration may have a significant tropospheric component, where the MJO modulations in the tropospheric O_3 may be due to different mechanisms that are out of the scope of this work.

To quantify the relative contributions of the stratospheric versus tropospheric O_3 to the observed MJO modulations in the total column O_3, representative subtropical regions where the MJO modulations are largest in the respective hemispheres are chosen. These regions are defined as 80°E–200°E, 14°N/S–34°N/S, which are enclosed in Fig. 5.5. The overall MJO variability in the vertical O_3 concentrations there is shown in Fig. 5.6a(i) and b(i). For both MLS and TES, the MJO modulations have a peak in the lower stratosphere near the tropopause at ~ 100 hPa. The maximum variations are ~ 0.4 DU km^{-1} and ~ 0.2 DU km^{-1} for the northern and southern subtropics, respectively. This supports the idea that the MJO modulations found in TOMS and AIRS total O_3 column are related to the vertical displacements of the tropopause. In the northern hemisphere, the altitude where the signal peaks at for MLS is the same as that for TES. But in the southern hemisphere, the altitude for MLS is slightly lower than that for TES by ~ 2 km. This difference is, however, within the vertical resolution, ~ 6 km, of TES near the tropopause.

Fig. 5.6 a(ii) and b(ii) show the MJO variability of the partially integrated O_3 column from 30 hPa to pressure levels below, including those in the troposphere. Both MLS and TES show variability of ~ 4 DU and ~ 2 DU at ~ 150 hPa in the northern and southern subtropical region, respectively. We compare the MJO modulations in O_3 as observed by MLS and TES with that in the total column O_3 data derived from OMI in Fig. 5.6a(ii) and b(ii). We applied the same band-pass filter and MJO compositing method to OMI O_3 column anomalies and obtained the MJO patterns. The variability in the regions defined above from OMI total O_3 column are 5.0 and 2.6 DU in the northern and southern subtropical regions, respectively, which are ~ 20% larger than those in the subtropical O_3 column derived from MLS and TES. Although there are quantitative differences between OMI, MLS and TES measurements, qualitatively the above comparison shows that the majority of the MJO variability in the total O_3 column comes from the lower stratosphere, and the factor-of-2 difference in the MJO-amplitudes between the northern and southern subtropics seems robust.

TES O_3 profiles also allow us to estimate the fractional MJO variability in the total O_3 column due to the tropospheric components. From Fig. 5.6b(ii), the total cumulative MJO variability of O_3 at the surface is 4.0 DU and 2.2 DU in the northern and southern subtropics, respectively. On the other hand, the corresponding cumulative MJO variability of O_3 from surface to 200 hPa is 1.1 DU and 0.6 DU, or 24% and 27%, in the northern and southern subtropics, respectively.

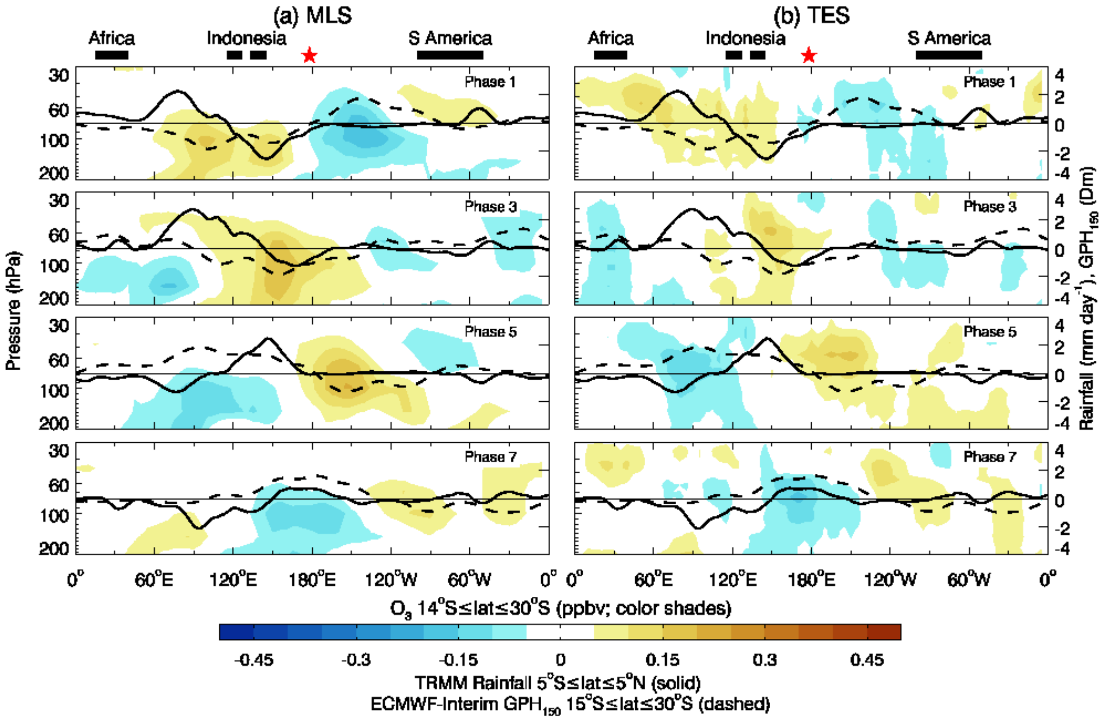

Fig. 5.8. As in Fig. 5.7 except for the southern subtropics. The O3 anomalies (color shades) are averaged between 14°S and 30°S; the GPH_{150} anomalies (dashed) are averaged between 15°S and 30°S. The location of Fiji (178.4°E, 18.13°S) is denoted by the star (★).

Fig. 5.7 shows the pressure-longitude cross sections of the MJO-related O_3 anomalies in the northern subtropics averaged between 14°N and 30°N from both MLS and TES. A 20° longitude spatial running average has been applied to remove high-wavenumber fluctuations. Overplotted are MJO-related equatorial rainfall anomalies averaged between 5°S and 5°N from TRMM (solid lines) and MJO-related subtropical GPH_{150} anomalies averaged between 15°N and 30°N from ERA-Interim (dotted lines). Eastward propagations are seen in the anomalies of O_3, rainfall, and GPH_{150}. The MJO-amplitude of the equatorial rainfall is ±2 mm day^{-1}. It has a positive anomaly in the western Indian Ocean in Phase 1, which then propagates to the central Pacific in Phase 8. The corresponding MJO-amplitude of the northern subtropical GPH_{150} is ±20 m. The upper-tropospheric subtropical cyclones (negative GPH_{150} anomalies at Phase 3) lead the equatorial enhanced convection (Phase

6) ,while the latter leads the upper-tropospheric subtropical anticyclones (positive GPH_{150} anomalies at Phase 7) by 5–10 days. This is consistent with the relationship between the equatorial rainfall anomalies and subtropical GPH_{150} anomalies shown in Fig. 5.4. In general, positive O_3 anomalies are found when GPH_{150} anomalies are negative in all phases, supporting the idea that the O_3 anomalies are mainly related to dynamical motions. Both MLS and TES data indicate that the same sign of subtropical O_3 anomalies at the same location can be found from 200 hPa to 30 hPa but the maximum O_3 anomalies are approximately in the lower stratosphere.

Similar result is also found in the southern subtropical O_3 anomalies between 14°S and 30°S, which are shown in Fig. 5.8. The same 20° longitude spatial running average has been applied and MJO-related subtropical GPH_{150} anomalies from ERA-Interim (dotted lines) averaged between 15°S and 30°S are overplotted. The equatorial rainfall anomalies are the same as those in Fig. 5.7. Overall the eastward propagations of O_3 and GPH_{150} are similar to those in the northern subtropics. The MJO-amplitude of southern subtropical GPH_{150} is comparable (±20 m) to that in the northern subtropics. The O_3 anomalies here, however, are only about half of those in the northern subtropics, as noted above.

As a form of validation, the vertical structures of the MJO-related O_3 anomalies over Fiji (178.40°E, 18.13°S) derived from MLS and TES are compared to those derived from SHADOZ. The MLS O_3 anomalies are obtained over the 10° longitude × 8° latitude box centered at Fiji, which is the same region that has been used to derive the time series in Fig. 5.3. There are in general 300–400 daily values being averaged in each MJO phase during the boreal winters (Fig. 5.9). The TES O_3 anomalies are similarly obtained in the enclosed region. There are only 20–80 daily values being averaged each phase due to lower horizontal resolutions than MLS. On average, TES provides about one daily observation or two per week over the box enclosing Fiji. On the other hand, for the SHADOZ project over Fiji, there is only one O_3 measurement or two biweekly over the site. As a result, roughly 10–20 daily values are averaged in each phase during the boreal winters. We applied the same band-pass filter to SHADOZ time series.

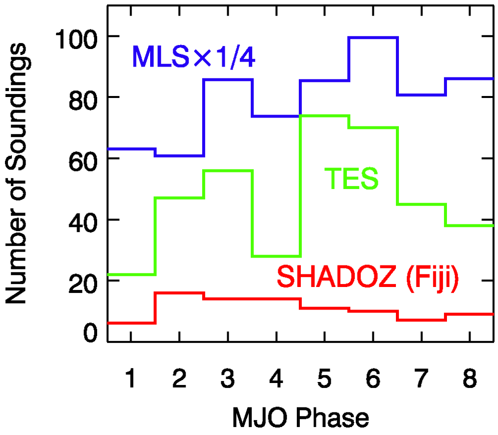

Fig. 5.9. The number of MLS (blue) and TES (green) swath footprints that fall into the 10° longitude × 8° latitude box centered at Fiji used in this study. The count of MLS has been scaled down by a factor of 4. The number of SHADOZ ozonesonde measurements used in this study is shown in red.

In Fig. 5.10, solid lines denote MJO-related rainfall anomalies from TRMM averaged between 5°S and 5°N at 178.5°E. Dashed lines represent GPH_{150} anomalies at (178.5°E, 18°S) from ERA-Interim. The equatorial rainfall anomalies at 178.5°E show a minimum in Phase 2 and a maximum in Phase 6. Meanwhile, the GPH_{150} anomalies have a minimum in Phase 4 and a maximum in Phase 7. The MJO anomalies of MLS and TES O_3 show a peak-to-trough amplitude of ~ 0.35 DU km^{-1} at ~ 100 hPa and ~ 80 hPa, respectively, and their maximum amplitudes both occur in Phase 4. On the other hand, the SHADOZ O_3 anomaly shows a peak-to-trough amplitude of ~ 0.3 DU km^{-1} at ~ 100 hPa. In general, the maximum MJO amplitudes in SHADOZ O_3 are attained in Phases 4–5. The quantitative differences between MLS/TES and SHADOZ may be due to the much lower sampling rates of SHADOZ. Moreover, there is a vertical tilt in the SHADOZ O_3 anomaly, which is formed by the extension of a positive anomaly in Phase 3 at 200 hPa to that in Phase 5 at 30 hPa. Qualitatively, there is also a hint of vertical tilt in the anomalies of both MLS and TES O_3 concentrations. These agreements among MLS, TES, and SHADOZ indicate that the vertical structures of the O_3 anomalies from MLS and TES, should be trustworthy to give insight into the objective posed by this study.

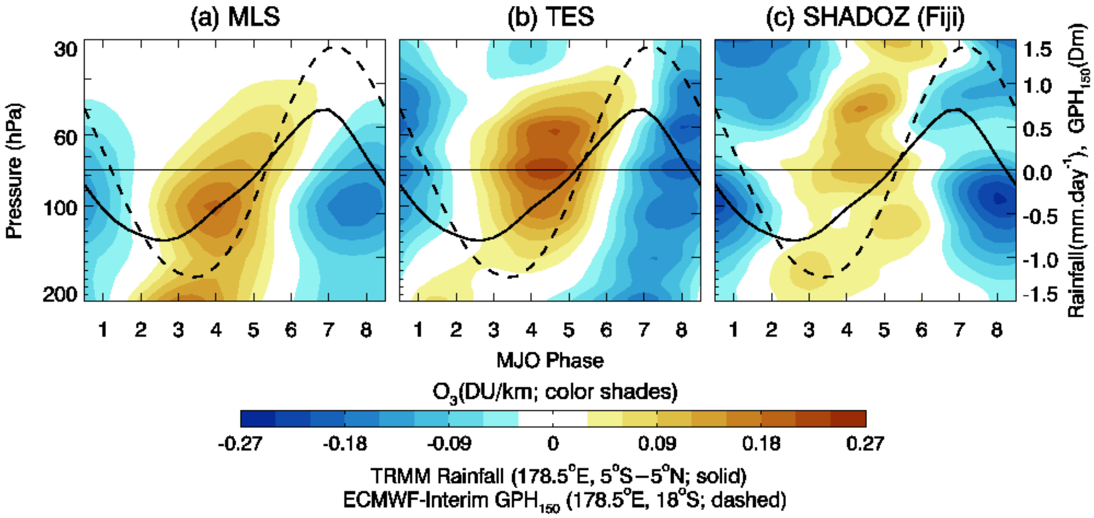

Fig. 5.10. Vertical structures of the O3 anomalies over Fiji (178.40°E, 18.13°S) from (a) MLS, (b) TES, and (c) SHADOZ as a function of MJO phase for the composite MJO life cycle. The MLS and TES O3 anomalies are obtained by averaging the swath footprints that fall into the 10°longitude × 8°latitude box centered at Fiji. Solid lines denote MJO-related rainfall anomalies from TRMM averaged between 5°S and 5°N at 178.5°E. Dashed lines represent GPH_{150} anomalies at (178.5°E, 18°S) from ERA-Interim.

5.4. Summary and Concluding Remarks

Tian et al. (2007) found that the MJO-related total column O_3 anomalies are mainly evident over the subtropics in the Pacific Ocean and the eastern hemisphere. The subtropical total column O_3 anomalies are typically collocated with the subtropical upper-tropospheric cyclones/anticyclones associated with the dynamics of the MJO and are anti-correlated with geopotential height anomalies near the tropopause. From these observational results, it was speculated that the subtropical total column O_3 anomalies are mainly associated with the O_3 variability in the stratosphere rather than the troposphere. Vertical O_3 profiles from MLS and TES provide a unique opportunity for examining this hypothesis and understanding the relative contribution of different atmospheric layers, especially stratosphere versus troposphere, to the subtropical total column O_3 anomalies. The composite MJO analysis above suggests that the spatial-temporal patterns of the subtropical stratospheric O_3 anomalies from MLS and TES are similar to those of the subtropical total column O_3 anomalies from TOMS and AIRS as reported previously (Tian et al., 2007). In particular, the anomalies in the subtropical stratospheric O_3 and those in the total column are both dynamically driven by the vertical movements of subtropical tropopause layer, characterized by the GPH_{150}. The MJO modulations in subtropical O_3 have peaks in the lower stratosphere in both MLS and TES data, but the peak of MLS O_3 is located at the pressure level 100 hPa, which is lower than that of TES $O_{3,}$ located at 80 hPa. Furthermore, TES measurements show that 20–30% of the total O_3 column anomalies are contributed by the tropospheric components. The strengths of the MJO modulations over Fiji derived from MLS and TES O_3 roughly agree with that derived from the *in situ* measurements by SHADOZ. This indicates that the subtropical total column O_3 anomalies are mostly from the O_3 anomalies in the lower stratosphere, which supports the hypothesis of Tian et al. (2007).

Currently O_3 vertical profiles have also been retrieved from the Huggins band observed by OMI but these products are under development and evaluation (Liu, 2010a, b). Future work could involve an O_3 budget analysis using a sophisticated chemical transport model and a similar study in the near-equatorial regions and/or tropospheric regions where the MJO signals in total O_3 are weak and other source and sink processes may be playing larger and possibly compensating roles. This study demonstrates the potential for the MLS and TES O_3 to improve our understanding of O_3 dynamics and chemistry, and its effects on climate change. Given that the potential predictability of the MJO extends to lead times of 2–4 weeks [*Waliser et al.*, 2003], the strong connection between the intraseasonal subtropical stratospheric O_3 variations and the MJO implies that the stratospheric O_3 variations may also be predictable with similar lead times over the subtropics.

Chapter 6.

A Link Between Tropical Intraseasonal Variability and Polar Stratospheric O_3[§]

Summary

In the last chapter, subtropical upper troposphere/lower stratosphere (UTLS) ozone (O_3) has been shown to be modulated by the MJO. This chapter further studies the teleconnection of MJO in the Arctic UTLS O_3. Dominant signals (13–20 Dobson units) are found over regions northwards of 30°N. Over the Arctic, the UTLS O_3 anomalies are dominated by wavenumber-2–3 structures and are anti-correlated with the geopotential height (GPH) anomalies at 250 hPa. The latter indicates that the O_3 anomalies are associated with dynamical motions near the tropopause, similar to those found in the tropics in the last chapter. Thus air quality over the Arctic can also be affected by tropical dynamics through teleconnection.

[§] To be submitted to *Atmos. Chem. Phys.* in Li, K.-F., B. Tian, K.-K. Tung, L. Kuai, J. R. Worden, and Y. L. Yung (2012), A link between tropical intraseasonal variability and polar stratospheric ozone.

6.1. Motivation

Intraseasonal anomalies of moist deep convection in the tropics evolve together with the global atmospheric circulation. It is well known that the MJO can influence the extratropical dynamics [*Kim et al.*, 2006; *Pan and Li*, 2008] and is the major source of predictability on intraseasonal time scales in the extratropics [*Jones et al.*, 2004; *Jung et al.*, 2010; *Lin et al.*, 2010; *Vitart and Molteni*, 2010]. Tropical convection and extratropical weather may be linked through redistribution of mass by convection associated with broad-scale overturning circulations, global and regional cycles of atmospheric angular momentum [*Egger and Weickmann*, 2007; *Weickmann and Berry*, 2009], and Rossby wavetrains that extend eastward and poleward across the midlatitudes [*Jin and Hoskins*, 1995]. Conversely, tropical convection may also be modified by extratropical waves [*Hoskins and Yang*, 2000]. The associations between the tropical and extratropical patterns frequently express themselves as global teleconnection patterns [*Ferranti et al.*, 1990; *Cassou*, 2008; *Roundy and Gribble-Verhagen*, 2010]. For a review of the MJO-teleconnection, please see Chapter 14 of *Lau and Waliser* [2011].

Both *Tian et al.* [2007] and the materials presented in the previous chapter limited their discussions to tropics and subtropics (±40°) only. However, possible effects of the MJO on the O_3 over extratropical or polar regions have not been investigated. Anomalous extratropical flows can be forced by tropical vorticity perturbations resulting from diabatic heating associated with the MJO cycle [*Ferranti et al.*, 1990; *Weare et al.*, 2012]. The extratropical response in the GPH during boreal winter is dominated by anomalous circulations at ~ 60°N. Some studies suggest that the circulation patterns of the GPH anomalies may correlate with the Pacific-North American pattern (PNA) [*Mori and Watanabe*, 2008] and North Atlantic oscillation (NAO) [*Cassou*, 2008; *Lin et al.*, 2009]. Thus, given the GPH-O_3 correlation reported in the previous chapter over the intraseasonal time scale, it is expected that MJO-teleconnection of polar O_3 may also be significant. The aim of the present work is to complement the study of *Tian et al.* [2007] and that of the previous chapter to provide a global picture of the MJO-related pattern of UTLS O_3 during boreal (northern) winter.

In the following, the same O_3 datasets from MLS, TES, and OMI will be studied. As in the previous chapter, all time series are first deseasonalized and a running-average band-pass filter for 15–90 days is applied to the time series. Then the anomalies are averaged over the eight MJO phases defined by the RMM index where $\mathrm{RMM}_1^2 + \mathrm{RMM}_2^2 \geq 1$. The MJO events during boreal winters (November–April) will be studied.

6.2. Results

Fig. 6.1 shows the boreal winter mean O_3 profiles in the subarctic region (60°N–80°N). The combination of MLS (blue) and TES (green) provides the whole O_3 profile from ground to upper stratosphere (only 1–1000 hPa is shown). Here, for ease of comparison with the partial columns, we adopt a unit DU/km for O_3 concentration (not to be confused with DU/kGPH to be defined later for the regression coefficient between O_3 and GPH), which is equivalent to 2.69×10^{11} molecules/cm^{-3}. In the subarctic region, the O_3

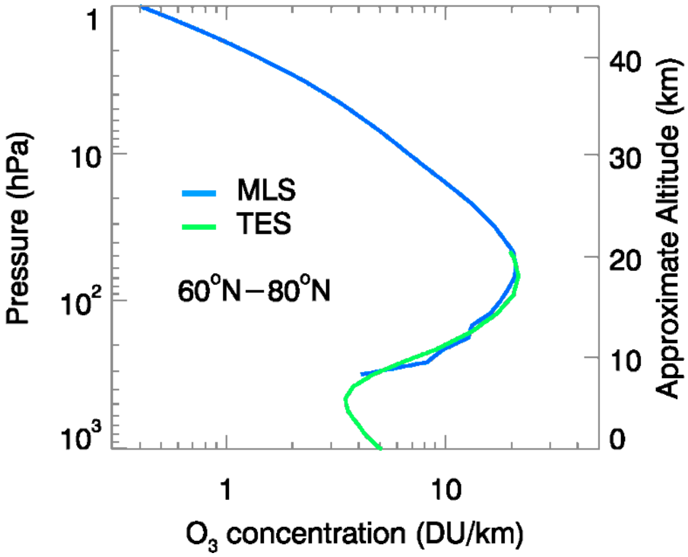

Fig. 6.1. The mean O_3 profile over subarctic (60°N–80°N) during boreal winter seasons (November–April) observed by MLS (blue) and TES (green). O_3 concentrations are expressed in unit of DU/km, which is equivalent to 2.69×10^{11} molecules/cm^{-3}.

concentration peaks at ~ 60 hPa (20 km), which has a peak value of ~ 20 DU/km. The O_3 concentration drops to less than 10 DU/km below 200 hPa and above 20 hPa.

Fig. 6.2a,b,c show the northern hemispheric spatiotemporal patterns in MJO-related UTLS partial column O_3 (PCO) anomalies derived from MLS (for 32–316 hPa) and TES (for 42–316 hPa), and total column O_3 (TCO) anomalies derived from TOMS. In the last chapter, the PCO and TCO anomalies have been compared with GPH at 150 hPa (hereafter GPH_p denotes the pressure level at p hPa), which is approximately the height of the tropical tropopause. However, for high latitudes, the tropopause is at ~ 250 hPa and GPH_{250} is therefore more appropriate [*Hoinka et al.*, 1996]. We overlay the GPH_{250} anomaly (black solid/dotted lines) in Fig. 6.2. Also shown are the rainfall anomalies (purple/green solid lines). Note that anticlockwise orientation is from west to east. Africa is located at the bottom of the azimuth projection (0°), south-eastern Asia is located in the upper-right-hand corner (120°E), and the eastern Pacific is located in the upper-left corner (120°W). For simplicity, the 8 typical phases defined by the RMM index have been reduced to four by summing Phases 8 and 1 (VIII+I), 2 and 3 (II+III), 4 and 5 (IV+V), and finally 6 and 7 (VI+VII). The propagation of MJO disturbances is represented by the rainfall anomalies. The overall MJO patterns of O_3 are dominated by wavenumber-2 and wavenumber-3 structure around the North Pole. The details in individual phases are described as follows.

During Phase VIII+I, positive equatorial rainfall anomalies related to the MJO are found in the western Indian Ocean. There are also negative equatorial rainfall anomalies extending from the east of the Maritime Continent to the western Pacific Ocean. For MLS (Fig. 6.2a), the UTLS PCO anomaly is dominated by a dumbbell-like negative pattern, which extends from Alaska (–8 DU), crossing the North Pole (–2 DU), to Russia (–4 DU). This negative pattern is surrounded by a positive anomaly, which extends from Europe (4 DU), going eastwards along the 30°N latitude circle (2 DU), to the center of action (COA) in the northern Pacific (8 DU). There is also a positive anomaly (4 DU) over the eastern United States. These MLS O_3 anomalies are well anti-correlated with the GPH_{250} anomalies. Note that while the rainfall anomalies are confined to the eastern hemisphere, the PCO and GPH anomalies are significant over both eastern and western hemispheres.In Phase II+III, the

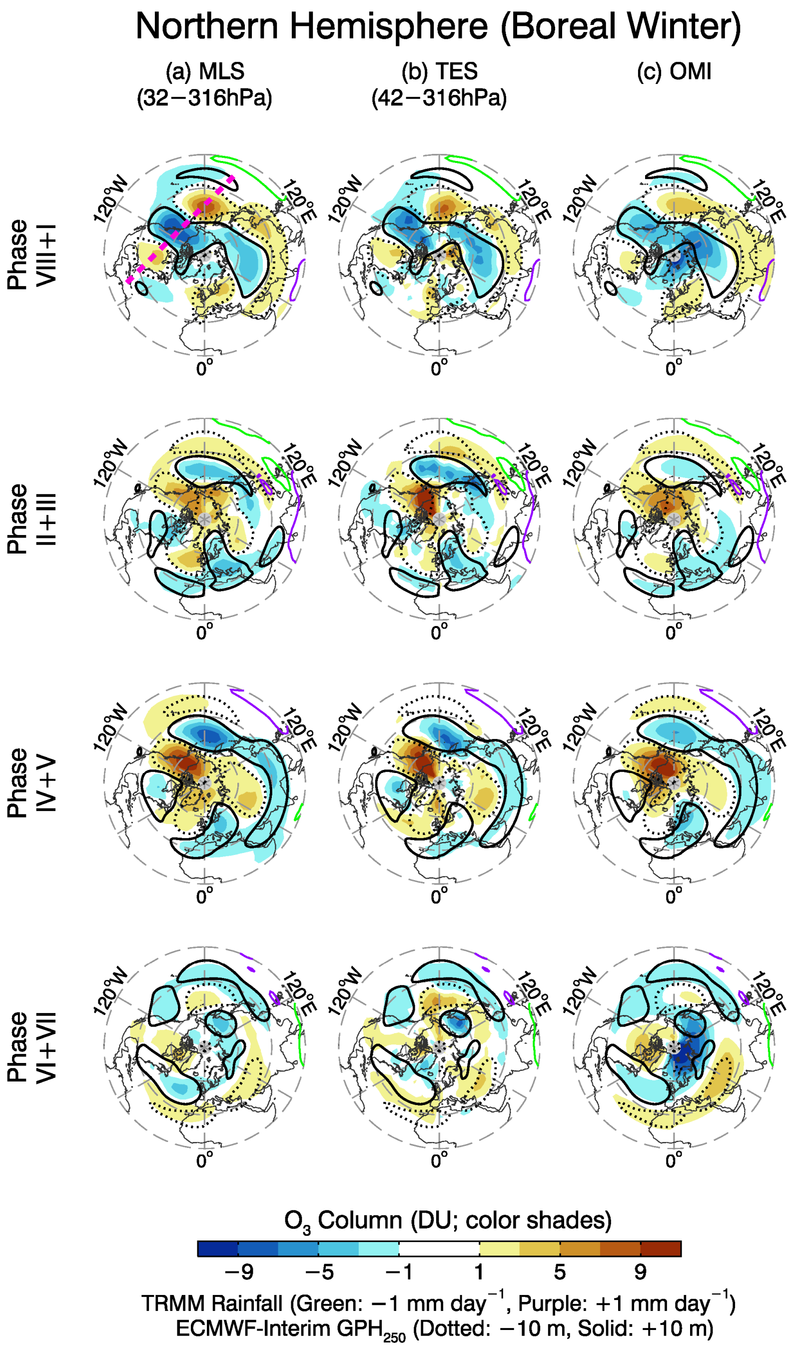

Fig. 6.2. MJO modulations in (a) MLS partial column ozone (PCO), (b) TES PCO, and (c) OMI total column ozone (TCO) for northern hemisphere. Also overlaid are rainfall anomalies from TRMM (green/purple) and geopotential height (GPH) anomalies at 250 hPa (GPH_{250}) from ECMWF interim reanalysis (dotted/solid). The shade represents O_3 column in Dobson unit (DU). The pink dashed line in the top-left panel highlights the Rossby wave train that may be associated with the Pacific-North America pattern.

rainfall anomalies have moved eastward by ~ 30°. The MLS PCO anomalies are dominated by a positive pattern (3 DU) that covers Alaska and Siberia, which further extends over the North Pole (2 DU), and covers part of the northern Atlantic and Russia. This positive anomaly is surrounded by a weak negative anomaly (2–4 DU) that extends from the eastern United States, going eastwards along the 30°N latitude circle, to the northern Pacific COA. Again, these O_3 anomalies are well anti-correlated with the GPH_{250} anomalies. Phase IV+V is simply characterized by reversed signs in rainfall, GPH_{150}, and MLS PCO anomalies with respect to Phase VIII+I. Finally, Phase VI+VII is characterized by a few weak positive and negative anomalies (< 2 DU) over the northern extratropics.

Overall, the correlation coefficient between the MLS PCO and GPH_{250} anomalies in all MJO phases for latitudes northwards of 45°N is –0.74 (Table 6.1). (Absolute values of correlation coefficients above 0.5 will be regarded as significant.) Therefore, the MJO-related PCO variability over the Arctic region is likely associated with the tropopause displacements caused by equatorial heating related to MJO [*Ferranti et al.*, 1990; *Tian et al.*, 2007].

The robustness of the anticorrelation between the MLS PCO and GPH_{250} anomalies is supported by independent O_3 measurements from TES. The MJO-related patterns for TES PCO (Fig. 6.2b) are very similar to those of MLS (Fig. 6.2a). The correlation coefficient between the TES PCO and GPH_{250} anomalies for latitudes north of 45°N is –0.62, which is less than that for MLS (Table 6.1).

Table 6.1. Correlation coefficients of geopotential heights (GPHs) with MLS partial column O_3 (PCO), TES PCO, and OMI total column O_3 (TCO) for latitudes polewards of 45°N. GPH at 250 hPa (GPH_{250}) is used for both Arctic regions.

Correlation	MLS PCO	TES PCO	OMI TCO
Arctic GPH_{250}	–0.75	–0.62	–0.41

Similar MJO patterns are also seen from OMI TCO measurements (Fig. 6.2c). The correlation coefficient between the OMI TCO and GPH_{250} anomalies for latitudes north of 45°N is –0.41 (Table 6.1), which is only marginal. There are also small signals (~ 1 DU) in the tropical regions observed by OMI that are absent from MLS and TES, which are likely from the troposphere [*Ziemke and Chandra*, 2003; *Tian et al.*, 2007].

In the last chapter, it has been shown that for the vertical structures of eastward-propagating O_3 anomalies in subtropical regions (14°N–34°N and 14°S–34°S) during the MJO life cycle derived from MLS and TES observations, the subtropical MJO signals are mainly from the UTLS layers. Such analysis turns out to be very useful for diagnosing possible dynamical causes. Here we replot their vertical structures in the sub-Arctic in Fig. 6.3 for 60°N–80°N. The equatorial rainfall anomalies (solid) averaged over ±5° latitudes

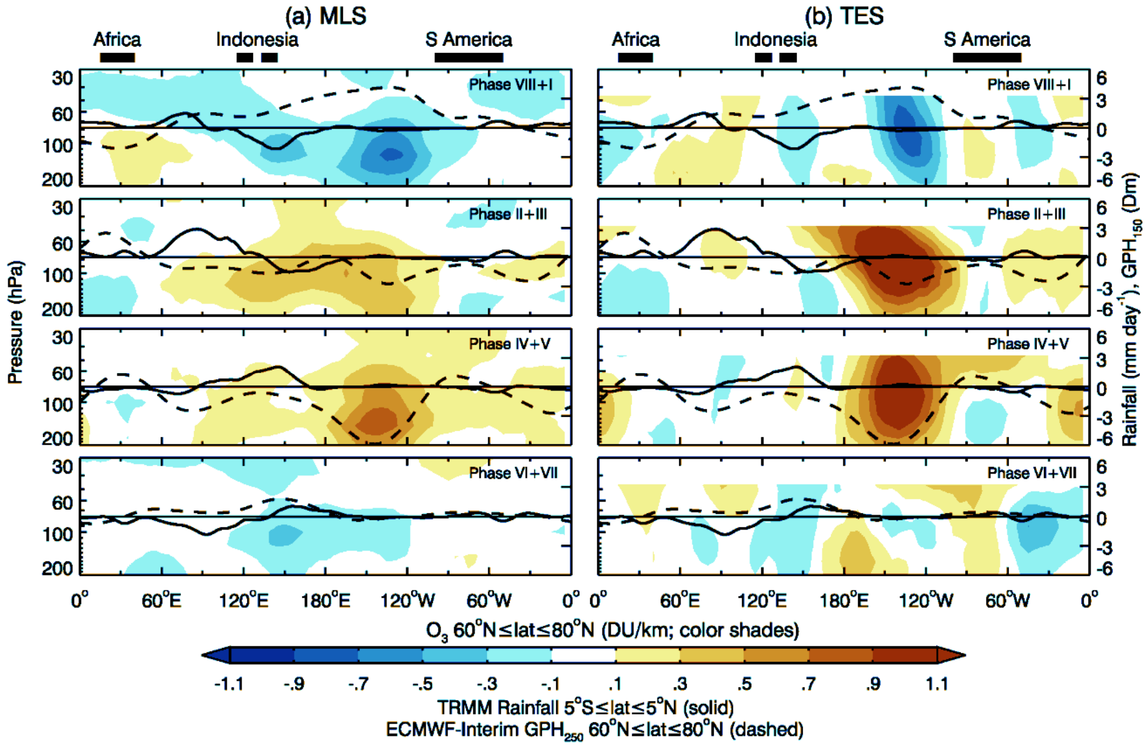

Fig. 6.3. The zonal propagation of the MJO signal in O_3 concentrations along the sub-Arctic latitude band 60°N–80°N. Also overlaid are the equatorial rainfall anomalies for latitudes within ±5° and GPH_{250} averaged over the same subarctic band. The GPH_{250} anomalies are expressed in units of decameters (Dm = 10 m).

Table 6.2. The regression coefficients between GPHs and the O_3 data used in Table 6.1. The unit is Dobson unit (DU) per 1000 meters change in GPH (kGPH).

DU/kGPH	MLS PCO	TES PCO	OMI TCO
Arctic GPH_{250}	–107	–99	–87

are used to illustrate the propagation of the MJO convective disturbances, which propagates from the Indo-Pacific region to the central Pacific throughout the MJO life cycle, as discussed previously. The GPH_{250} anomalies (dashed) averaged over 60°N–80°N are also overlaid.

In the subarctic region, the MLS O_3 anomalies (Fig. 6.3a) are the most prominent near the northern Pacific COA (130°W) at 130 hPa, with an amplitude ±1 DU/km. In Phase VIII+I, a negative MLS UTLS partial column O_3 anomaly (–0.8 DU/km) is developed near the northern Pacific COA, which becomes positive (0.8 DU/km) in the subsequent Phases II+III and IV+V. Finally in Phase VI+VII, the anomaly near the northern Pacific COA becomes negative again (–0.3 DU/km). The TES O_3 anomalies evolve similarly during the MJO life cycle (Fig. 6.3b), but we note that the MJO-related amplitude is larger (ranging from –0.8 to 1.6 DU/km). The pattern of the TES UTLS O_3 anomalies in Phase VI+VII is noisier than MLS in the same phase. The GPH_{150} anomalies exhibit the largest amplitude (±50 m) near the northern Pacific COA and are anti-correlated with the O_3 anomalies, as discussed above.

6.3. Discussions

It is well known that tropical diabatic heating associated with the MJO excites mid-latitude planetary waves via barotropic vorticity perturbations, which then move polewards [*Gill*, 1980; *Ferranti et al.*, 1990; *Kiladis et al.*, 2001; *Seo and Son*, 2012]. These wave perturbations are known to influence northern hemispheric weather patterns in both troposphere and stratosphere [*Zhou and Miller*, 2005; *Lin et al.*, 2009; *Lin et al.*, 2010; *Weare*, 2010].

A recent model study [*Seo and Son*, 2012] suggests that the anomalous tropical heating related to the MJO results in Rossby wave train of wavenumbers 2–3 in the northern hemispheric 200 hPa streamfunction, which travels from the Warm Pool northward to the northern Pacific and North America, then turns southward to the equatorial African Continent. The spatial structure of such a Rossby wave train is typical of the PNA [*Trenberth and Hurrell*, 1994; *Mori and Watanabe*, 2008]. In this way, energy from the Warm Pool can be deposited to higher latitudes along the wave train on an intraseasonal time scale. Such teleconnection through Rossby wave trains in GPH is also evident in the O_3 patterns (highlighted by a pink dashed line in Fig. 6.2, top-left panel).

Weare [2010] found two coexisting pathways through which the planetary waves may propagate into the northern polar stratosphere on an intraseasonal time scale: (1) The wave flux first moves polewards horizontally at lower altitudes near the tropopause (~ 200 hPa) and then injects vertically into the stratosphere in extratropical regions; (2) The wave flux first injects vertically into the lower/middle stratosphere (50–100 hPa) at lower latitudes and then moves polewards. Since there is good correlation between the O_3 and GPH_{250} anomalies in almost the whole northern hemisphere, our results suggest that Path 1 involving a barotropic propagation at 250 hPa is adequate for explaining the observed MJO modulations in extratropical O_3 in this hemisphere.

A correlation between the total column O_3 and GPH has been known as the ozone-weather relationship [*Meetham*, 1937; *Poulin and Evans*, 1994], where previous authors have derived a regression coefficient between these quantities from various meteorological processes, including daily, annual, and interannual variations. Below, we define the regression coefficient in unit of DU per 1000 meters change in GPH and denote it as DU/kGPH. (Previous studies used the notation DU/km in place of DU/kGPH. However, we have already used DU/km as a unit of O_3 concentration above.) We will also make clear by subscripting $DU/kGPH_p$, where p is the pressure level at which GPH is representing. The regression coefficient may strongly depend on locations, periods, and instrument characteristics. Older reported values can range from –10 $DU/kGPH_{250}$ [*Meetham*, 1937] to –100 $DU/kGPH_{250}$ [*Langlo*, 1952]. More recent analyses using multiple ground-based measurements suggest a typical value ranging between 13–18 $DU/kGPH_{250}$ [*Hoinka et al.*, 1996; *Steinbrecht et al.*, 1998]. The latter seems to be supported by a model simulation accounting for the ENSO effect in tropical O_3 for |latitude| ≤ 30° [*Wang et al.*, 2011], where the regression coefficient is found to be 15.5 DU/kGPH$_{p'}$, where *p*' is the tropopause pressure.

Our results append the previous values by (1) utilizing satellite observations and (2) making use of the intraseasonal variability. In the northern hemisphere, the regression coefficients derived from MLS PCO, TES PCO, and OMI TCO are –107, –99, and –87 DU/kGPH$_{250}$, respectively (Table 6.2). These three values seem to support the earlier finding by *Langlo* [1952] but are much higher than more−recent ground-based measurements and that modelled by *Wang et al.* [2011]. The large range of the observed values, including the ones found in this study related to the MJO and those from ground-based measurements from other studies [*Hoinka et al.*, 1996; *Steinbrecht et al.*, 1998] requires more quantitative modelling for further elucidation.

Tung and Yang [1988] theoretically derived a value of 7% change in column O_3 per 1% change in lower stratospheric temperature, assuming that any changes in the latter (and hence GPH) are adiabatic and are only related to planetary wave passages. This value is equivalent to –56 DU/kGPH$_{p''}$, where *p*" is the pressure level that O_3 concentration peaks at (a constant scale height of 7 km is assumed), given the total column O_3 is ~ 400 DU over polar regions. *Tung and Yang* [1988] also derived a lower value of –28 DU/kGPH by further assuming that the lower stratosphere is at radiative equilibrium. Therefore, the regression coefficient should range from –28 to –56 DU/kGPH over the Arctic region because part of the area is in polar night during boreal winters.

6.4. Summary and Concluding Remarks

Appending to the study of *Tian et al.* [2007] and that in the last chapter, a global picture of the MJO modulations in UTLS O_3 during boreal winters is presented. The RMM index has been used to divide an MJO cycle into phases that describe the propagation of the tropical MJO convective disturbances from the western Indian Ocean to the central Pacific. When MLS PCO, TES PCO, and TOMS TCO are averaged over these MJO phases, dominant anomalous signals are found over the Arctic. It has been shown that these O_3 anomalies are well anti-correlated with the GPH anomalies that are similarly composited using the RMM index. This suggests that these polar anomalies are mainly driven by dynamical motions of stratified atmospheric layers resulting from anomalous diabatic heating associated with the MJO, consistent with previous findings in the subtropics. The ozone-GPH correlation related to the MJO is –100 DU/kGPH for the northern hemisphere north of 45°N. This value is in general much higher than other reported values derived from ground-based measurements and model studies.

The peak-to-trough MJO modulations in lower stratospheric O_3 are typically ~ 20 DU over the Arctic. Such O_3 changes may modify the polar lower stratospheric temperature profile through radiative heating in the presence of sunlight, which may then change O_3 further given the O_3-GPH correlation described above, forming a positive feedback. A simple radiative transfer calculation [*Jiang et al.*, 2008c] suggests that temperature change induced by net O_3 heating (shortwave minus longwave) between 10 hPa and 100 hPa is ~ 0.1 K/DU. Therefore, the maximum changes in polar lower stratospheric temperature induced by the MJO-related O_3 net radiative heating are 2 K in the Arctic lower stratosphere.

Polar ozone changes may also be related to changes of the Brewer-Dobson circulation (BDC) in the winter hemisphere as a result of planetary wave perturbations [*Garcia-Herrera et al.*, 2006]. The typical turnover time for the BDC is 1–2 years. Therefore, while the BDC may play a role in the case of ENSO [*Wang et al.*, 2011], its effects on the observed intraseasonal variability, if any, may not be dominant.

We also noted a possible connection between the observed extratropical MJO modulations in O_3 with PNA. Detailed simulations with comprehensive feedback mechanisms would be essential for studying these subtle but important effects on polar O_3 dynamics and chemistry. Understanding these teleconnection patterns in chemical tracers like O_3 help monitor and predict air qualities and ultraviolet (UV) levels at higher latitudes as a result of tropical influences.

Chapter 7.

Tropical Mid-Tropospheric CO_2 Variability driven by MJO[**]

Summary

Carbon dioxide (CO_2) is the most important anthropogenic greenhouse gas in the present-day climate. Most of the community focuses on its long-term (decadal to centennial) behaviors that are relevant to climate change, but there are relatively few discussions of its higher-frequency forms of variability, and none regarding its subseasonal distribution. In this work, we report a large-scale intraseasonal variation in the Atmospheric Infrared Sounder (AIRS) CO_2 data in the global tropical region associated with the MJO. The peak-to-peak amplitude of the composite MJO modulation is ~ 1 ppmv, with a standard error of the composite mean < 0.1 ppmv. The correlation structure between CO_2 and rainfall and vertical velocity indicate that positive (negative) anomalies in CO_2 arise due to upward (downward) large-scale vertical motions in the lower troposphere associated with the MJO. These findings can help elucidate how faster processes can organize, transport, and mix $CO_{2,}$ and provide a robustness test for coupled carbon-climate models.

7.1. Motivation

CO_2 is the most important anthropogenic greenhouse gas in the present-day climate, contributing more than 50% of the total anthropogenic warming [*Quay et al.*, 1992;

[**] Published in Li, K.-F., B. Tian, D. E. Waliser, Y. L. Yung (2010), Tropical mid-tropospheric CO2 variability driven by the Madden-Julian oscillation, *Proc. Nat. Acad. Sci. U. S. A., 107*, 19171−19175, doi:10.1073/pnas.1008222107.

Francey et al., 1999; *IPCC*, 2007]. Recently, the CO_2 mixing ratios in the middle troposphere (~ 5–10 km) have been retrieved using data from the Atmospheric Infrared Sounder (AIRS) aboard NASA's Aqua satellite [*Chahine et al.*, 2005; *Chahine et al.*, 2006; *Chahine et al.*, 2008]. This 7-year global daily CO_2 dataset has shown rich variability with time scales from semiannual to interannual (e.g., ENSO) [*Chahine et al.*, 2008; *Jiang et al.*, 2010], which helps improve our understanding of major processes that control the carbon exchange among reservoirs.

The AIRS Level 2 mid-tropospheric CO_2 product is retrieved using as input the AIRS Level 2 temperature, water vapor and ozone geophysical products and selected channels of cloud-cleared radiances within the CO_2 absorption bands, i.e., 704–721 cm^{-1} [*Chahine et al.*, 2005; *Chahine et al.*, 2006; *Chahine et al.*, 2008]. The spatial resolution at nadir is 90 km × 90 km, and the product is a column-weighted average of the CO_2 volume mixing ratio profile. At tropical latitudes, the weighting function peak occurs at 400 hPa (~ 7.5 km) and decreases to half its value at 120 hPa (~ 15 km) and 515 hPa (~ 5.5 km) [see Fig. 1 of *Chahine et al.*, 2005]. Validation by comparison to *in situ* aircraft and ground-based measurements demonstrates that individual retrievals of AIRS CO_2 are accurate to better than 2 ppmv between latitudes 30°S and 80°N [*Chahine et al.*, 2008]. The CO_2 Level 3 daily product employed in our analysis is an average of the individual Level 2 CO_2 retrievals over a 24-hour span within a 2.5° longitude × 2° latitude grid. For latitudes between ±40°, the number of retrievals being averaged in each grid for each day ranges from zero to a maximum of 15, depending on the availability of at least three valid AIRS Level 2 retrievals in a 2 × 2 grouping of adjacent retrievals. This unprecedented AIRS mid-tropospheric CO_2 dataset provides new opportunities for climate studies and new constraints for climate models. For example, based on the AIRS mid-tropospheric CO_2 data, it has been shown that convection in some of the chemistry-climate models has to be strengthened in order to reproduce observed CO_2 latitudinal gradients [*Jiang et al.*, 2008a]. In addition, the impact of changes in the Walker circulation over the central and western Pacific Ocean as a result of ENSO have been detected in the AIRS mid-tropospheric CO_2 data [*Jiang et al.*, 2010]. For this reason, we expect that convection and large-scale vertical

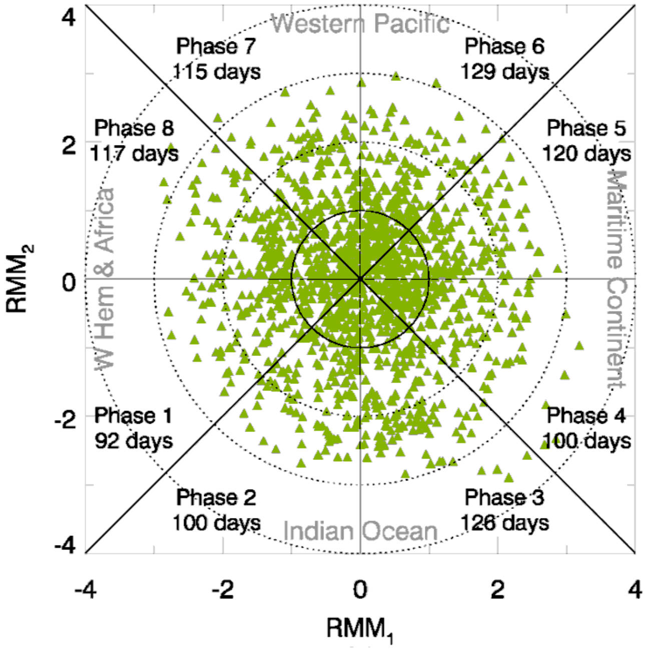

Fig. 7.1. (RMM_1, RMM_2) phase space for all days in boreal winter from November 2002 to February 2010 and the number of days for each phase of the composite MJO cycle. Each triangle represents one day. The solid circle defines the threshold $RMM_1^2 + RMM_2^2 \geq 1$ for strong MJO events. Only days outside the threshold were included in the MJO-composite average shown in Figs. 7.3 and 7.4.

motion may also regulate CO_2 on the intraseasonal scale and AIRS mid-tropospheric CO_2 data may be able to reveal the MJO signal in CO_2.

7.2. Data and Method Summary

AIRS Level 3 daily CO_2 products were obtained from AIRS Data Server (http://disc.sci.gsfc.nasa.gov/AIRS/data-holdings/by-data-product/AIRX3C2D). AIRS Level 3 daily H_2O products were obtained from AIRS Data Server (http://disc.sci.gsfc.nasa.gov/AIRS/data-holdings/by-data-product/airsL3_STD_AIRS_AMSU.shtml). NCEP/NCAR reanalysis data used in this study were provided by the NOAA/OAR/ESRL PSD Data Server (http://www.esrl.noaa.gov/psd/data/reanalysis/). ERA-Interim reanalysis data used in this study were obtained from the ECMWF Data Server (http://data.ecmwf.int/data/). The NOAA ESRL CO_2 data from the Carbon Cycle Cooperative Global Air Sampling Network, 1968−2008, Version 2009-07-15 were obtained from NOAA FTP Server (ftp://ftp.cmdl.noaa.gov/ccg/co2/flask/event/). CONTRAIL data were obtained from the WMO World Data Centre for Greenhouse Gases (http://gaw.kishou.go.jp/cgi-bin/wdcgg/accessdata.cgi). RMM indices were obtained from (http://www.cawcr.gov.au/bmrc/clfor/cfstaff/matw/maproom/RMM/).

As in previous chapters, the phases of the MJO will be defined using the RMM Index [*Wheeler and Hendon*, 2004]. Fig. 7.1 shows the (RMM_1, RMM_2) phase space for all days

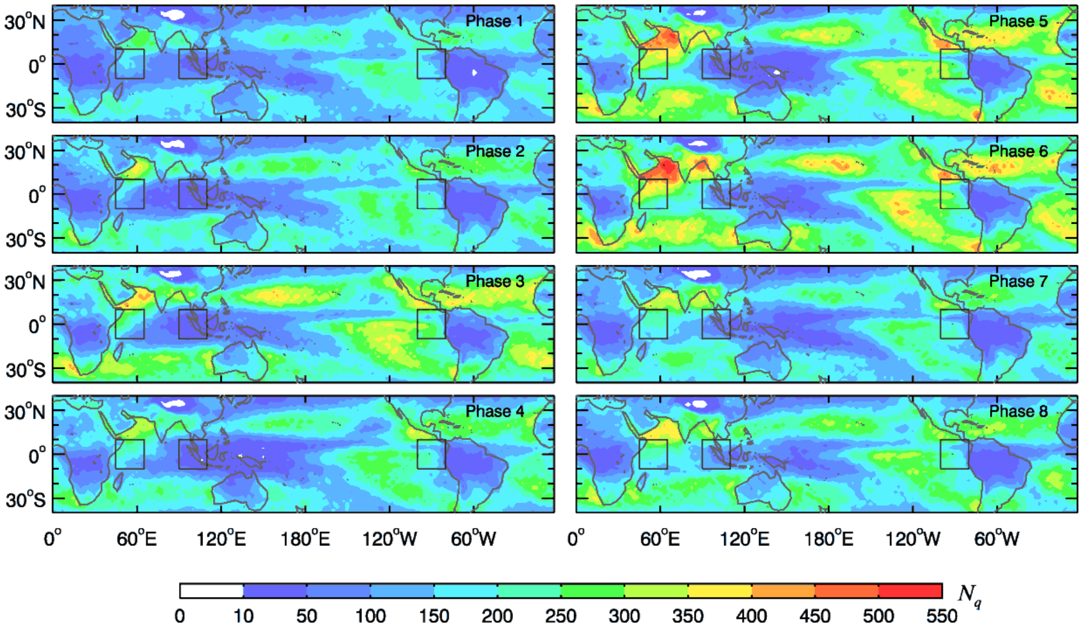

Fig. 7.2. Total number of AIRS CO_2 retrievals N_q being averaged for each phase of the composite MJO cycle on the 2.5° × 2° grid. No spatial smoothing has been applied. The spatial variations are due mainly to the local cloud conditions that affect the cloud-cleared radiances for AIRS CO_2 retrievals. Note that, depending on the local cloud conditions, there may be zero or multiple CO_2 retrievals at each grid point on each individual day. Hence N_q may be less or more than the number of days in each MJO phase of the composite MJO cycle shown in Fig. 7.1. N_q may range from ~ 10 for cloudy regions (e.g., eastern Indian Ocean) to ~ 500 for cloud-free regions (e.g., eastern Pacific). The 20° × 20° square boxes enclose the representative regions for Fig. 7.7. The total number of retrievals being averaged in each square box $\tilde{N}_q$ is the sum of N_q at individual grid points within that box.

in boreal winter from November 2002 to February 2010 and the number of days for each phase of the composite MJO cycle. Only days with strong MJO activity $\left(\mathrm{RMM}_1^2+\mathrm{RMM}_2^2 \geq 1\right)$ are considered. In general, the number of days in each phase of the composite MJO cycle ranges from 90 to 130 days. Noting that depending on the local cloud conditions, there may be zero or multiple CO_2 retrievals at each grid point on each individual day, the number of CO_2 retrievals being averaged in each phase of the composite MJO cycle (N_q) may range from ~ 10 for cloudy regions (e.g., eastern Indian Ocean) to ~ 500 for cloud-free regions (e.g., eastern Pacific; Fig. 7.2). The same method was applied to the time series shown in Fig. 7.7, except that the composite means were calculated using all daily data satisfying the above criteria in the 20° × 20° square boxes. The total number of CO_2 retrievals $\tilde{N}_q$ being averaged in each square box is thus the sum of N_q over all the individual grid points within that box: $\tilde{N}_q = \sum_{\substack{20^\circ\times 20^\circ \\ \text{grid box}}} N_q$. The critical value α for 99% confidence interval was derived from a two-tailed Student's *t*-statistics, where the degree of freedom was $\tilde{N}_q - 1$. The 99% confidence interval was given by $\left(\tilde{\mu}-\alpha\tilde{\sigma}\big/\sqrt{\tilde{N}_q}\,,\tilde{\mu}+\alpha\tilde{\sigma}\big/\sqrt{\tilde{N}_q}\right)$, where $\tilde{\mu}$ and $\tilde{\sigma}$ are the mean and the standard deviation of the data being averaged. Over the western Indian Ocean and the eastern Pacific Ocean, $\tilde{N}_q$ ranges from 5000 to 8000 and the standard errors of the sample means at 99% level, $\alpha\tilde{\sigma}\big/\sqrt{\tilde{N}_q}$, of the CO_2 composite means are thus ~ 0.02 ppmv. Since the region near Indonesia is relatively cloudy, $\tilde{N}_q$ drops to 2000–5000. Consequently, the standard errors of the sample means over Indonesia are ~ 0.05 ppmv.

7.3. Results

Fig. 7.3 shows the composite maps of the MJO-related mid-tropospheric CO_2 variation for eight commonly used phases of the MJO [*Wheeler and Hendon*, 2004;

Waliser et al., 2009] defined by the pair of All-season Real-time Multivariate MJO (RMM) Indices [*Wheeler and Hendon*, 2004]. These maps are created using AIRS 2.5° × 2° gridded Level 3 CO_2 data during the boreal winters in November 2002–February 2010. To indicate the eastward propagation of the convective anomaly associated with the MJO, we overlaid the rainfall MJO anomalies from the TRMM (solid/dotted contour lines) in Fig. 7.3. The TRMM rainfall data we used cover the same period as AIRS and are interpolated onto the same 2.5° × 2° grids as AIRS. For improved visualization, a 10° × 8° running average is applied to both CO_2 and rainfall anomalies to remove high-wavenumber spatial

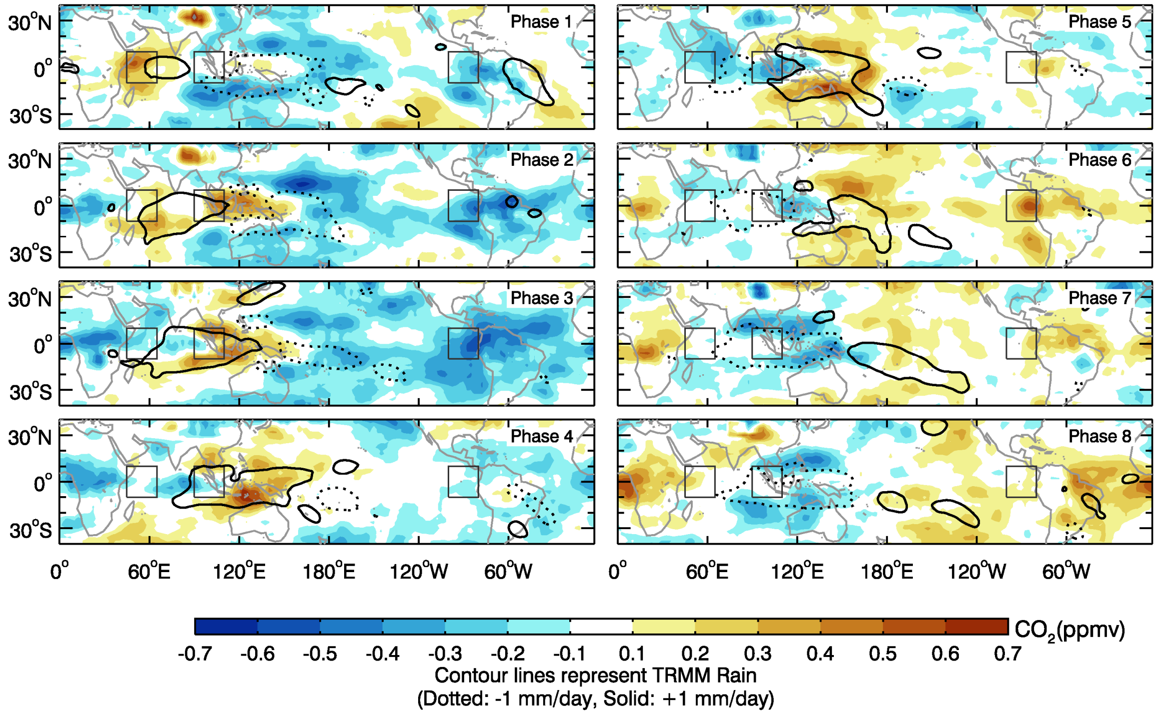

Fig. 7.3. MJO-related AIRS CO_2 anomalies. The MJO phase is defined using the All-season Real-time Multivariate MJO Index (RMM_1, RMM_2). Each phase represents a period of ~ 6 days. Only those days that satisfy $RMM_1^2 + RMM_2^2 \geq 1$ are included in the composite mean calculation. To indicate the propagation of the MJO, we overlaid the MJO-related rainfall anomaly using solid (dotted) contours for regions of values greater (lower) than +1 (–1) mm day^{-1}. The 20° × 20° square boxes enclose the representative regions for Fig. 7.5. For visualization, a 10° longitude × 8° latitude running average is applied to both CO_2 and rainfall anomalies to remove high-wavenumber spatial fluctuations.

fluctuations. In Phase 1, a positive rainfall anomaly is found in the western equatorial Indian Ocean, indicating the presence of enhanced convection and rising air motion in this area. A significant positive anomaly in CO_2 (~ +0.4 ppmv) is also apparent in this area. When the rising air mass reaches the upper troposphere, it diverges away from the cluster center and subsides in both east and west sides (e.g., Indonesia), where the air becomes relatively drier and the convection is suppressed, as indicated by a negative rainfall anomaly. These dry areas show a negative anomaly (~ –0.4 ppmv) in AIRS CO_2, which extends all the way to the Eastern Pacific and South America, where the rainfall anomaly is small. In Phases 2–4, the positive rainfall anomaly propagates eastward with a speed of ~ 5 m/s. The positive CO_2 anomaly also propagates eastward and the propagation pattern is consistent with that of the rainfall. Meanwhile, there is a significant drop in CO_2 (~ –0.6 ppmv) over South America and central Africa, where the rainfall anomaly is weak. In Phases 5–8, the enhanced convection moves from the Maritime Continent to the central Pacific, while the convection is suppressed in the Indian Ocean, as indicated by a negative rainfall anomaly there. Meanwhile, the enhanced CO_2 (~ +0.3 ppmv) propagates with the

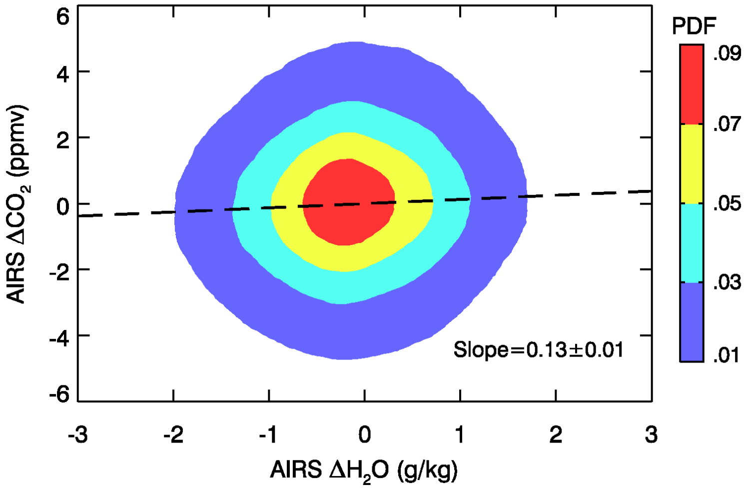

Fig. 7.4. Scatter plot of AIRS Level 3 CO_2 and H_2O daily anomalies during the winters of September 2002–November 2009 between 10°S and 10°N. Color contours represent the probability distribution function of the scattered points. The slope of the linear fit is 0.13±0.01 ppmv-CO_2 per g/kg-H_2O.

enhanced convection into the central Pacific. In addition, a positive CO_2 anomaly (~ +0.5 ppmv) develops over the eastern Pacific and South America and it travels across the Atlantic Ocean to the central Africa. The speed of propagation in this relatively convection-free region is much faster (~ 20 m/s), yet consistent with the observed dynamical life-cycle of the MJO [*Hendon and Salby,* 1996]. The anomaly continues to propagate into the Indian Ocean and the MJO cycle by inference repeats.

The main thermal infrared channels for CO_2 retrieval have some dependence on the presence of water vapor (H_2O), where a 10% error in water is estimated to cause a 1 ppmv bias in CO_2 [*Chahine et al.,* 2005]. To examine any residual effects of H_2O in the retrieved CO_2, we show in Fig. 7.4 a scatter plot of all daily CO_2 and AIRS 550 hPa H_2O anomalies between 10°S–10°N, where the seasonal cycles are removed. The color contours represent the probability distribution function (p.d.f.) of the scatter points. A least-square fit gives a slope of ~ 0.13 ± 0.01 ppmv-CO_2 per g/kg-H_2O. If we assume that the slope is completely due to the retrieval bias from the H_2O absorption bands and assume that the MJO amplitude in H_2O at that level is ~ 1.4 g/kg [*Tian et al.,* 2006], then the bias in CO_2 would be ~ 0.17 ppmv, which is much less than the signal we found above. Therefore, the MJO signal in AIRS CO_2 is unlikely an artifact of retrieval errors due to H_2O absorption.

7.4. Relations with vertical motions

The above comparison suggests that large-scale vertical motions may account for the MJO modulations in CO_2. Hence, to quantify their effects on the AIRS CO_2 variations, we compute the MJO-related pressure velocity anomalies at 700 hPa (ω_{700}) from the European Center for Medium-range Weather Forecasting Interim (ERA-Interim) re-analysis product, covering the same period as AIRS. Furthermore, the ERA-interim data have been interpolated on the same 2.5° × 2° spatial grids as AIRS. For later discussion, we define the negative pressure velocity $\tilde{\omega}_{700} = -\omega_{700}$ such that positive (negative) $\tilde{\omega}_{700}$ refers to rising (sinking) motions. The $\tilde{\omega}_{700}$ anomalies from ERA-Interim are shown in Fig. 7.5 (solid/dotted contours) and so are the CO_2 anomalies. For comparison, a 10° longitude × 8°

latitude running average has also been applied. Over the Indian Ocean and the western Pacific, the MJO modulation of $\tilde{\omega}_{700}$ resembles that of AIRS CO_2 and they are positively correlated. Over the eastern Pacific and the American Continents, the $\tilde{\omega}_{700}$ anomalies, though weak, show some variations that are also consistent with the CO_2 anomalies (c.f. Fig. 7.5).

To further study their correlation, one can compute the covariance of the MJO-modulated anomaly of CO_2 with that of $\tilde{\omega}_{700}$, which is shown in Fig. 7.6. It has been suggested that covariance or linear regression coefficients are more robust quantities than the correlation coefficients for filtered data [*Coughlin and Tung*, 2006]. A positive covariance is generally seen over the western hemispheric oceans. It extends eastwards from the equatorial western Indian Ocean, reaching a maximum (~ 2.5 ppmv mPa s^{-1}) over

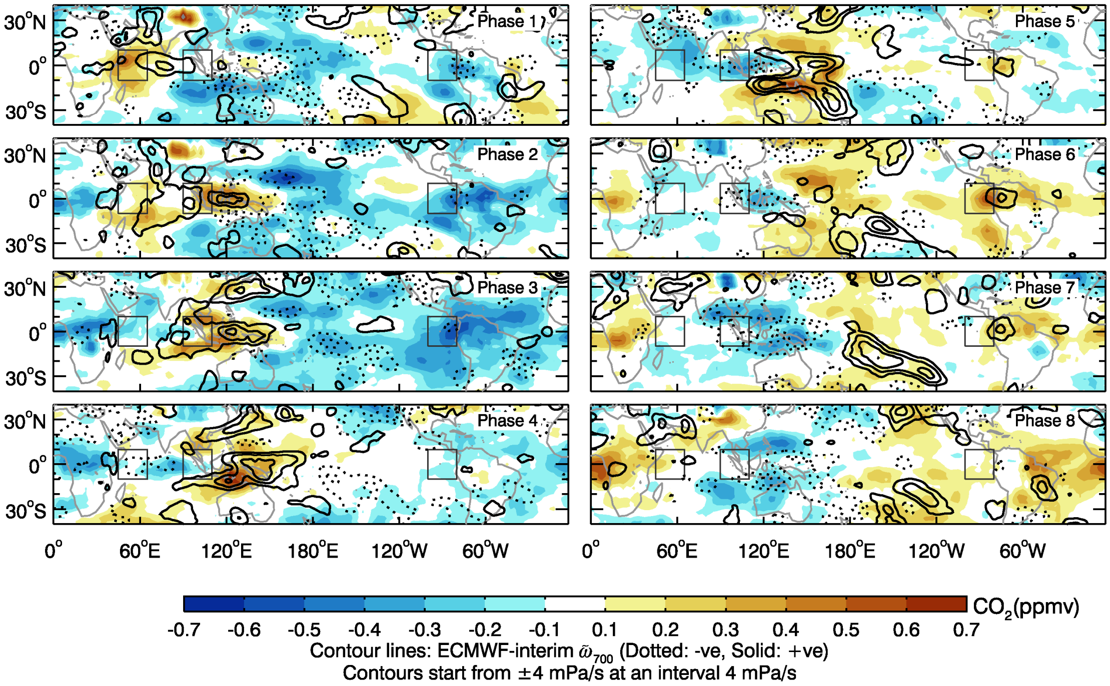

Fig. 7.5. Same as Fig. 7.3 except that ERA-Interim 700 hPa pressure velocity anomalies $\tilde{\omega}_{700}$ are overlaid. The pressure velocity data cover the same period and have been interpolated to the same spatial grid as AIRS. Note that we redefined the pressure velocity such that positive (negative) values indicate rising (sinking) motions.

Indonesia, to the central Pacific. The southward movement of the covariance in the central Pacific resembles the characteristics of the MJO during boreal winters. In the eastern Pacific, there is a positive covariance (~ 1.3 ppmv mPa s^{-1}) near the coastline of Peru (0° N, 80° W). Overall, large-scale vertical motions in the lower troposphere are positively correlated with the MJO-related CO_2 anomalies.

To highlight the temporal variations in the variability of CO_2 and vertical motions, we show in Fig. 7.7 the time series in three representative regions over the western Indian Ocean, Indonesia, and the eastern Pacific Ocean. These regions are enclosed by 20° × 20° square boxes shown in Figs. 7.3 and 7.4. The eastward movement of the convective anomaly associated with the MJO is referenced by the rainfall anomaly. In general, these time series suggest a reasonably coherent MJO evolution between the relevant variables. The standard errors of the mean CO_2 variations, shown in blue shades, are of order ~ 0.02–0.05 ppmv. It is evident that the CO_2 anomaly exhibits roughly the same magnitudes (~ 0.5 ppmv) over all of the selected locations and is significantly different from zero at the 99% level or better, clearly showing its global effects. Over all three locations, the CO_2 variation is positively correlated with ERA-Interim $\tilde{\omega}_{700}$. We note that the peak-to-peak amplitude of

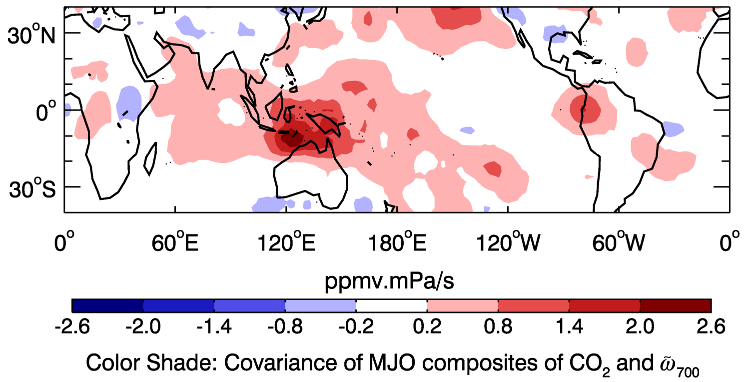

Fig. 7.6. The covariance between the MJO-related AIRS CO_2 and ERA-Interim 700 hPa vertical velocity anomalies. A 10° longitude × 8° latitude running average has been applied. Positive covariance suggests that positive CO_2 anomalies are associated with enhanced upward motions, and vice versa.

ERA-Interim $\tilde{\omega}_{700}$ over Indonesia (~ 13 mPa s^{-1}) is about four times as strong as that over the other locations, likely due to the warmer sea surface temperature. For comparison, the NCEP/NCAR $\tilde{\omega}_{700}$ anomalies are overlaid in Fig. 7.7. The $\tilde{\omega}_{700}$ variations from the two re-analyses are generally consistent with each other, although NCEP/NCAR $\tilde{\omega}_{700}$ is moderately stronger over the Indian Ocean and eastern Pacific. Moreover, there are some phase differences between NCEP/NCAR $\tilde{\omega}_{700}$ and CO_2 and between NCEP/NCAR $\tilde{\omega}_{700}$ and ERA-Interim $\tilde{\omega}_{700}$. Thus, $\tilde{\omega}_{700}$ from both ERA-Interim and NCEP/NCAR provide at least a qualitative picture that supports lower tropospheric vertical motions being an important driver of the MJO modulation on the mid-tropospheric CO_2.

7.5. Concluding remarks

We have presented the first observation of the MJO modulation in free-tropospheric CO_2. To date, there has been no attempt to simulate intraannual or interannual variability (e.g., ENSO) in atmospheric CO_2 [*Jiang et al.*, 2010]. Thus the above observation provides a unique constraint as well as a robustness test for coupled carbon-climate models. The peak-to-peak amplitude is of order ~ 1 ppmv, which will have important implications on satellite measurements, such as NASA's Orbiting Carbon Observatory II (OCO-II) and Japan Aerospace Exploration Agency (JAXA)'s Greenhouse Gases Observing Satellite (GOSAT), that are designed to measure tropospheric CO_2 column with a precision better than 1 ppmv for determining carbon fluxes [*Rayner and O'Brien*, 2001]. It is also noted that for processes like the MJO, the satellite instrument designs must account for cloud effects and the natural correlations between them and the moist processes and trace gases distributions that are so closely linked in order to accurately measure trace gas abundance in the lower atmosphere and under disturbed atmospheric conditions. This is likely to only be achieved through a multi-sensor framework that includes high spatial and spectral resolutions.

The above results also provide hints as to the vertical distribution of CO_2. Since large-scale upward motions effectively transport air from the boundary layer to the free troposphere on the time scale of about a day, the positive anomaly of AIRS CO_2 over regions with enhanced upward motion suggests that the surface CO_2 being brought up to the free troposphere has higher concentration than that in the free troposphere. Similarly, the negative anomaly over regions characterized by downward motion indicates that the sinking air from the free troposphere has lower CO_2. This seems to be generally true for the whole tropics. To verify this, the CO_2 averages of the NOAA ESRL ground-based measurements in Guam (13.45°N, 144.8°E; pink line) [*Conway et al.*, 1994] are compared with the CONTRAIL airborne flask measurements in the free troposphere near the region (blue line) [*Matsueda et al.*, 2002; *Machida et al.*, 2008] during boreal winters from 1994 to 2008 (Fig. 7.8). The CONTRAIL measurements are averaged between 5°N–20°N and 10–12 km. Guam is well-suited for this purpose because it is near the tropical warm pool region, where the MJO is active. Throughout the 15-year record, the ground CO_2 values are consistently higher by an average of 0.67 ± 0.26 ppmv (black dot with an error bar), which is of the same order of magnitude as the MJO anomalies shown in Fig. 7.3. The HIAPER Pole-to-Pole Observations (HIPPO) project, in which CO_2 concentrations and other trace gases at various latitudes in the Pacific Basin are sampled between 1 km−45 km, will provide another investigation of the CO_2 vertical profile in the Pacific regions.

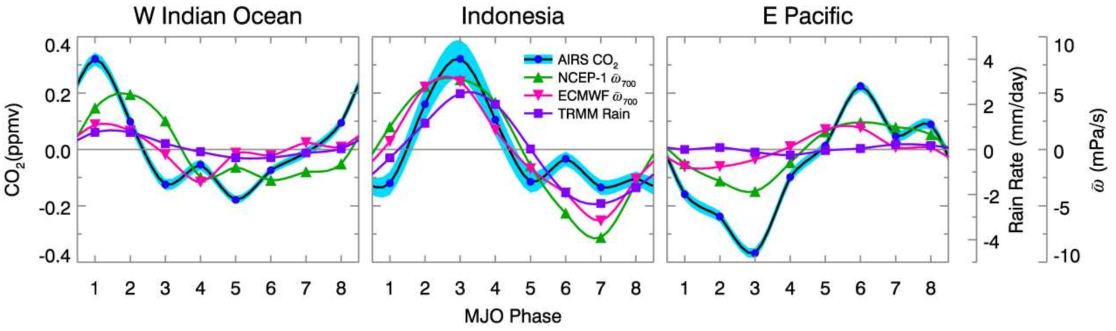

Fig. 7.7. Composite MJO time series of AIRS CO_2, reanalysis 700 hPa vertical velocity, and TRMM rainfall anomalies over the western Indian Ocean, Indonesia, and the eastern Pacific Ocean enclosed by the square boxes in Figs. 7.3 and 7.4. The blue bar overlaid on CO_2 shows the 99% confidence interval of the composite-mean uncertainty.

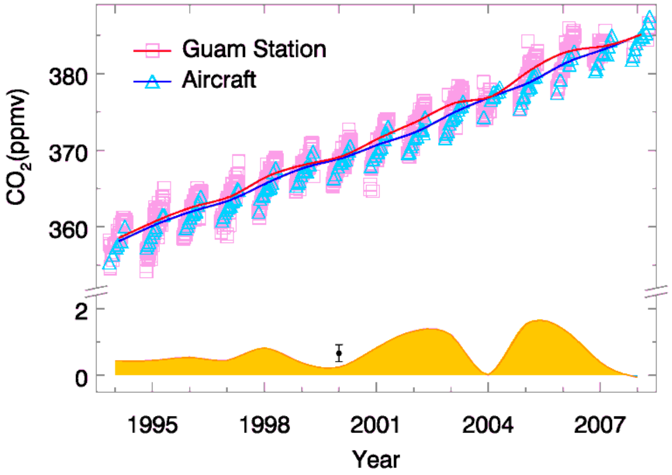

Fig. 7.8. Comparison of CO_2 winter-averages from 1994 to 2008 between NOAA ESRL ground-station (pink line) and CONTRAIL airborne flask measurements (blue line) over Guam (13.45°N, 144.8°E). Each square or triangle represents an individual measurement being used. During each flight, an individual airborne measurement shown in the figure is defined as an average of all flask measurements conducted between 5°N–20°N and 10–12 km. The yellow–filled area shows the ground-station values subtracted by the aircraft ones. The 15-year averaged difference is 0.67 ± 0.26 ppmv (black dot with an error bar).

Tropospheric CO_2 has also been measured by NASA's Tropospheric Emission Spectrometer (TES) and the European Space Agency (ESA)'s Infrared Atmospheric Sounding Interferometer (IASI) using thermal infrared channels similar to AIRS, ESA's Scanning Imaging Absorption Spectrometer for Atmospheric Cartography (SCIAMACHY), and GOSAT using the CO_2 absorption bands in near-infrared which characterize CO_2 at different altitudes. However, these data records are too short to provide a robust characterization of intraseasonal variability or have not been published yet. As these limitations are overcome, these independent data sets would combine to give collocated, vertical profiles of CO_2 and help confirm our findings.

BIBLIOGRAPHY

Allen, M., et al. (1981), Vertical Transport and Photochemistry in the Terrestrial Mesosphere and Lower Thermosphere (50−120 km), *J Geophys Res-Space Phys*, *86*, 3617−3627, doi:10.1029/JA086iA05p03617.

Allen, M., et al. (1984), The Vertical Distribution of Ozone in the Mesosphere and Lower Thermosphere, *J Geophys Res.—Atmos*, *89*, 4841−4872, doi:10.1029/JD089iD03p04841.

Austin, J., et al. (2008), Coupled chemistry climate model simulations of the solar cycle in ozone and temperature, *J. Geophys. Res.—Atmos.*, *113*, D11306, doi:10.1029/2007JD009391.

Bates, D. R., and M. Nicolet (1950), The Photochemistry Of Atmospheric Water Vapor, *J. Geophys. Res.*, *55*, 301−327, doi:10.1029/JZ055i003p00301.

Beer, R., et al. (2001), Tropospheric emission spectrometer for the Earth Observing System's Aura Satellite, *Appl. Optics*, *40*, 2356−2367.

Beer, R. (2006), TES on the Aura mission: Scientific objectives, measurements, and analysis overview, *IEEE T. Geosci. Remote*, *44*, 1102−1105, doi:10.1109/tgrs.2005.863716.

Beig, G., et al. (2012), Inter-comparison of 11-year solar cycle response in mesospheric ozone and temperature obtained by HALOE satellite data and HAMMONIA model, *J Geophys Res.—Atmos*, *117*, doi:10.1029/2011JD015697.

Bevington, P. R., and D. K. Robinson (1992), *Data Reduction and Error Analysis for the Physical Sciences*, 3rd ed., 336 pp., McGraw-Hill, New York.

Bond, G., et al. (2001), Persistent solar influence on north Atlantic climate during the Holocene, *Science*, *294*, 2130−2136, doi:10.1126/science.1065680.

Bowman, K. W., et al. (2006), Tropospheric emission spectrometer: Retrieval method and error analysis, *IEEE T. Geosci. Remote*, *44*, 1297−1307, doi:10.1109/tgrs.2006871234.

Brasseur, G., and S. Solomon (1984), *Aeronomy of the Middle Atmosphere: Chemistry and Physics of the Stratosphere and Mesosphere*, Springer, Dordrecht.

Brasseur, G. (1993), The Response of the Middle Atmosphere to Long-Term and Short-Term Solar Variability: a 2-Dimensional Model, *J. Geophys. Res.—Atmos.*, *98*, 23079−23090, doi:10.1029/93JD02406.

Burnett, C. R., and E. B. Burnett (1996), The regime of decreased OH vertical column abundances at Fritz Peak Observatory, CO: 1991−1995, *Geophys Res Lett*, *23*, 1925-1927, doi:10.1029/96GL01811.

Cageao, R. P., et al. (2001), High-Resolution Fourier-Transform Ultraviolet-Visible Spectrometer for the Measurement of Atmospheric Trace Species: Application to OH, *Appl Opt*, *40*, 2024-2030, doi:10.1364/AO.40.002024.

Cahalan, R. F., et al. (2010), Temperature responses to spectral solar variability on decadal time scales, *Geophys. Res. Lett.*, *37*, L07705, doi:10.1029/2009GL041898.

Camp, C. D., et al. (2002), Presence of a Madden-Julian Oscillation Signal in the TOMS Ozone, *Eos Trans. AGU*, *83*, Fall Meet. Suppl., Abstract #A52A-0100.

Camp, C. D., et al. (2003), Temporal and spatial patterns of the interannual variability of total ozone in the tropics, *J. Geophys. Res.—Atmos.*, *108*, 4643, doi:10.1029/2001JD001504.

Canty, T., and K. Minschwaner (2002), Seasonal and solar cycle variability of OH in the middle atmosphere, *J Geophys Res.—Atmos*, *107*, 4737, doi:10.1029/2002JD002278.

Canty, T., et al. (2006), Stratospheric and mesospheric HO_x: results from aura MLS and FIRS-2, *Geophys Res Lett*, *33*, L12802, doi:10.1029/2006GL025964.

Cassou, C. (2008), Intraseasonal interaction between the Madden-Julian Oscillation and the North Atlantic Oscillation, *Nature*, *455*, 523-527, doi:10.1038/nature07286.

Chahine, M., et al. (2005), On the determination of atmospheric minor gases by the method of vanishing partial derivatives with application to CO_2, *Geophys. Res. Lett.*, *32*, L22803, doi:10.1029/2005GL024165.

Chahine, M. T., et al. (2006), Improving weather forecasting and providing new data on greenhouse gases, *B. Am. Meteorol. Soc.*, *87*, 911−926, doi:10.1175/BAMS-87-7-911.

Chahine, M. T., et al. (2008), Satellite remote sounding of mid-tropospheric CO_2, *Geophys. Res. Lett.*, *35*, L17807, doi:10.1029/2008GL035022.

Chapman, S. (1930), On ozone and atomic oxygen in the upper atmosphere, *Philos. Mag.*, *10*, 369−383.

Conway, T. J., et al. (1994), Evidence for interannual variability of the carbon-cycle from the NOAA/CMDL Global-Air-Sampling-Network, *J. Geophys. Res.—Atmos.*, *99*, 22831−22855.

Cortesi, U., et al. (2007), Geophysical validation of MIPAS-ENVISAT operational ozone data, *Atmos. Chem. Phys.*, *7*, 4807−4867.

Coughlin, K. T., and K. K. Tung (2006), Misleading patterns in correlation maps, *J. Geophys. Res.—Atmos.*, *111*, D24102, doi:10.1029/2006JD007452.

Crutzen, P. J. (1970), Influence of Nitrogen Oxides on Atmospheric Ozone Content, *Q. J. R. Meteorol. Soc.*, *96*, 320−325, doi:10.1002/qj.49709640815.

Dee, D. P., et al. (2011), The ERA-Interim reanalysis: configuration and performance of the data assimilation system, *Q. J. Roy. Meteor. Soc.*, *137*, 553−597, doi:10.1002/qj.828.

DeLand, M. T., and R. P. Cebula (2012), Solar UV variations during the decline of Cycle 23, *J. Atmos. Sol.—Terr. Phys.*, *77*, 225-234, doi:10.1016/j.jastp.2012.01.007.

Dhomse, S., et al. (2011), Solar response in tropical stratospheric ozone: a 3-D chemical transport model study using ERA reanalyses, *Atmos. Chem. Phys.*, *11*, 12773−12786, doi:10.5194/acp-11-12773-2011.

Egger, J., and K. Weickmann (2007), Latitude-height structure of the atmospheric angular momentum cycle associated with the Madden-Julian oscillation, *Mon. Weather Rev.*, *135*, 1564−1575, doi:10.1175/MWR3363.1.

Egorova, T., et al. (2004), Chemical and dynamical response to the 11-year variability of the solar irradiance simulated with a chemistry-climate model, *Geophys. Res. Lett.*, *31*, L06119, doi:10.1029/2003GL019294.

Eldering, A., et al. (2008), Implementation of cloud retrievals for TES atmospheric retrievals: 2. Characterization of cloud top pressure and effective optical depth retrievals, *J. Geophys. Res. —Atmos.*, *113,* D16S37, doi:10.1029/2007JD008858.

Esper, J., et al. (2002), Low-frequency signals in long tree-ring chronologies for reconstructing past temperature variability, *Science*, *295*, 2250−2253, doi:10.1126/science.1066208.

Ferranti, L., et al. (1990), Tropical extratropical interaction associated with the 30-60 day oscillation and its impact on medium and extended range prediction, *J. Atmos. Sci.*, *47*, 2177−2199, doi:10.1175/1520-0469(1990)047<2177:TEIAWT>2.0.CO;2.

Fioletov, V. E., et al. (2002), Global and zonal total ozone variations estimated from ground-based and satellite measurements: 1964-2000, *J. Geophys. Res.—Atmos.*, *107*, 4647, doi:10.1029/2001JD001350.

Francey, R. J., et al. (1999), A 1000-year high precision record of δ^{13}C in atmospheric CO_2, *Tellus Series B—Chemical and Physical Meteorology*, *51*, 170−193.

Froehlich, C. (2006), Solar irradiance variability since 1978 — Revision of the PMOD composite during solar cycle 21, *Space Sci Rev*, *125*, 53−65, doi:10.1007/s11214-006-9046-5.

Fujiwara, M., et al. (1998), Stratosphere-troposphere exchange of ozone associated with the equatorial Kelvin wave as observed with ozonesondes and rawinsondes, *J. Geophys. Res.—Atmos.*, *103*, 19173−19182, doi:10.1029/98JD01419.

Garcia-Herrera, R., et al. (2006), Propagation of ENSO temperature signals into the middle atmosphere: A comparison of two general circulation models and ERA-40 reanalysis data, *J. Geophys. Res.—Atmos.*, *111*, D06101, doi:10.1029/2005JD006061.

Gill, A. E. (1980), Some simple solutions for heat-induced tropical circulation, *Q. J. Roy. Meteor. Soc.*, *106*, 447−462, doi:10.1002/qj.49710644905.

Gray, L. J., et al. (2010), Solar Influences on Climate, *Rev. Geophys.*, *48*, RG4001, doi:10.1029/2009rg000282.

Gruber, A. (1974), Wavenumber-frequency spectra of satellite-measured brightness in tropics, *J. Atmos. Sci.*, *31*, 1675−1680, doi:10.1175/1520-0469(1974)031<1675:TWFSOS>2.0.CO;2.

Haigh, J. D., et al. (2010), An influence of solar spectral variations on radiative forcing of climate, *Nature*, *467*, 696−699, doi:10.1038/nature09426.

Harder, J. W., et al. (2010), The SORCE SIM Solar Spectrum: Comparison with Recent Observations, *Sol Phys*, *263*, 3−24, doi:10.1007/s11207-010-9555-y.

Heath, D. F., and B. M. Schlesinger (1986), The Mg 280-nm Doublet as a Monitor of Changes in Solar Ultraviolet Irradiance, *J. Geophys. Res.—Atmos.*, *91*, 8672−8682, doi:10.1029/JD091iD08p08672.

Hendon, H. H., and M. L. Salby (1994), The life-cycle of the Madden-Julian Oscillation, *J. Atmos. Sci.*, *51*, 2225−2237.

Hendon, H. H., and M. L. Salby (1996), Planetary-scale circulations forced by intraseasonal variations of observed convection, *J. Atmos. Sci.*, *53*, 1751−1758.

Hendon, H. H., and J. Glick (1997), Intraseasonal air-sea interaction in the tropical Indian and Pacific Oceans, *J. Clim.*, *10*, 647−661, doi:10.1175/1520-0442(1997)010<0647:IASIIT>2.0.CO;2.

Herschel, F. W. (1801), Observations tending to investigate the Nature of the Sun, in order to find the Causes or Symptoms of its variable Emission of Light and Heat; with Remarks on the Use that may possibly be drawn from Solar Observations, *Phil. Trans. R. Soc. London*, *91*, 265−318.

Herzberg, L. (1965), Solar optical radiation and its role in upper atmospheric processes, in *Physics of the Earth's Upper Atmosphere*, edited by C. O. Hines, et al., pp. 31−45, Prentice Hall, New Jersey.

Hoinka, K. P., et al. (1996), On the correlation between tropopause pressure and ozone above Central Europe, *Geophys. Res. Lett.*, *23*, 1753−1756, doi:10.1029/96GL01722.

Hood, L. L., and J. P. McCormack (1992), Components of Interannual Ozone Change Based on Nimbus-7 TOMS Data, *Geophys. Res. Lett.*, *19*, 2309−2312, doi:10.1029/92GL02638.

Hood, L. L., et al. (1993), Quasi-Decadal Variability of the Stratosphere: Influence of Long-Term Solar Ultraviolet Variations, *J. Atmos. Sci.*, *50*, 3941−3958, doi:10.1175/1520-0469(1993)050<3941:qdvots>2.0.co;2.

Hood, L. L., and B. E. Soukharev (2003), Quasi-decadal variability of the tropical lower stratosphere: The role of extratropical wave forcing, *J. Atmos. Sci.*, *60*, 2389−2403, doi:10.1175/1520-0469(2003)060<2389:QVOTTL>2.0.CO;2.

Hood, L. L., and B. E. Soukharev (2006), Solar induced variations of odd nitrogen: Multiple regression analysis of UARS HALOE data, *Geophys. Res. Lett.*, *33*, L22805, doi:10.1029/2006GL028122.

Hood, L. L., et al. (2010), Decadal variability of the tropical stratosphere: Secondary influence of the El Nino-Southern Oscillation, *J. Geophys. Res.—Atmos.*, *115*, D11113, doi:10.1029/2009JD012291.

Hoskins, B. J., and G. Y. Yang (2000), The equatorial response to higher-latitude forcing, *J. Atmos. Sci.*, *57*, 1197−1213, doi:10.1175/1520-0469(2000)057<1197:TERTHL>2.0.CO;2.

Hoyt, D. V., and K. H. Schatten (1997), *The Role of the Sun in Climate Change*, 279 pp., Oxford, New York.

Hu, F. S., et al. (2003), Cyclic variation and solar forcing of Holocene climate in the Alaskan subarctic, *Science*, *301*, 1890−1893, doi:10.1126/science.1088568.

Huffman, G. J., et al. (2007), The TRMM multisatellite precipitation analysis (TMPA): Quasi-global, multiyear, combined-sensor precipitation estimates at fine scales, *J. Hydrometeorol.*, *8*, 38-55, doi:10.1175/jhm560.1.

Hurrell, J. W., et al. (2008), A new sea surface temperature and sea ice boundary dataset for the Community Atmosphere Model, *J. Clim.*, *21*, 5145−5153, doi:10.1175/2008jcli2292.1.

Hurst, D. F., et al. (2011), Stratospheric water vapor trends over Boulder, Colorado: Analysis of the 30 year Boulder record, *J Geophys Res.—Atmos*, *116*, D02306, doi:10.1029/2010JD015065.

Ineson, S., et al. (2011), Solar forcing of winter climate variability in the Northern Hemisphere, *Nature Geosci.*, *4*, 753−757, doi:10.1038/ngeo1282.

IPCC (2007), *Climate Change 2007: The Physical Science Basis. Contribution of Working Group I to the Fourth Assessment Report of the Intergovernmental Panel on Climate*

Change, 996 pp., Cambridge University Press, Cambridge, United Kingdom and New York, NY, USA.

Iwagami, N., et al. (1998), Doppler detection of hydroxyl column abundance in the middle atmosphere: 2. Measurement for three years and comparison with a 1D model, *J Atmos Chem*, *29*, 195−216, doi:10.1023/A:1005928612004.

Jiang, X., et al. (2008a), Simulation of upper tropospheric CO_2 from chemistry and transport models, *Glob. Biogeochem. Cycle*, *22*, GB4025, doi:10.1029/2007GB003049.

Jiang, X., et al. (2008b), Interannual variability and trends of extratropical ozone. Part II: Southern Hemisphere, *J. Atmos. Sci.*, *65*, 3030−3041, doi:10.1175/2008JAS2793.1.

Jiang, X., et al. (2008c), Interannual variability and trends of extratropical ozone. Part I: Northern Hemisphere, *J. Atmos. Sci.*, *65*, 3013−3029, doi:10.1175/2008JAS2665.1.

Jiang, X., et al. (2010), Interannual variability of mid-tropospheric CO_2 from Atmospheric Infrared Sounder, *Geophys. Res. Lett.*, *37*, L13801, doi:10.1029/2010GL042823.

Jin, F. F., and B. J. Hoskins (1995), The direct response to tropical heating in a baroclinic atmosphere, *J. Atmos. Sci.*, *52*, 307−319, doi:10.1175/1520-0469(1995)052<0307:TDRTTH>2.0.CO;2.

Jirikowic, J. L., and P. E. Damon (1994), The Medieval Solar-Activity Maximum

Clim. Change, *26*, 309−316, doi:10.1007/BF01092421.

Jones, C., et al. (2004), The Madden-Julian oscillation and its impact on Northern Hemisphere weather predictability, *Mon. Weather Rev.*, *132*, 1462−1471, doi:10.1175/1520-0493(2004)132<1462:TMOAII>2.0.CO;2.

Jourdain, L., et al. (2007), Tropospheric vertical distribution of tropical Atlantic ozone observed by TES during the northern African biomass burning season, *Geophys. Res. Lett.*, *34*, L04810, doi:10.1029/2006GL028284.

Jucks, K. W., et al. (1998), Observations of OH, HO_2, H_2O, and O_3 in the upper stratosphere: implications for HO_x photochemistry, *Geophys. Res. Lett.*, *25*, 3935−3938, doi:10.1029/1998GL900009.

Jung, T., et al. (2010), Diagnosing the Origin of Extended-Range Forecast Errors, *Mon. Weather Rev.*, *138*, 2434−2446, doi:10.1175/2010MWR3255.1.

Keihm, S., et al. (2009), Ocean water vapor and cloud liquid water trends from 1992 to 2005 TOPEX Microwave Radiometer data, *J. Geophys. Res.—Atmos.*, *114*, D18101, doi:10.1029/2009JD012145.

Kiladis, G. N., et al. (2001), Aspects of interannual and intraseasonal variability of the tropopause and lower stratosphere, *Q. J. Roy. Meteor. Soc.*, *127*, 1961−1983, doi:10.1002/qj.49712757606.

Kim, B. M., et al. (2006), A new look at the midlatitude-MJO teleconnection in the northern hemisphere winter, *Q. J. Roy. Meteor. Soc.*, *132*, 485−503, doi:10.1256/qj.04.87.

Kodera, K., and Y. Kuroda (2002), Dynamical response to the solar cycle, *J. Geophys. Res.—Atmos.*, *107*, 4749, doi:10.1029/2002JD002224.

Kopp, G., et al. (2005), The Total Irradiance Monitor (TIM): Science results, *Sol Phys*, *230*, 129−139, doi:10.1007/s11207-005-7433-9.

Kopp, G., and J. L. Lean (2011), A new, lower value of total solar irradiance: Evidence and climate significance, *Geophys Res Lett*, *38*, L01706, doi:10.1029/2010GL045777.

Kuai, L., et al. (2009), Nonstationary Synchronization of Equatorial QBO with SAO in Observations and a Model, *J. Atmos. Sci.*, *66*, 1654−1664, doi:10.1175/2008JAS2857.1.

Kulawik, S. S., et al. (2006), Implementation of cloud retrievals for Tropospheric Emission Spectrometer (TES) atmospheric retrievals: part 1. Description and characterization of errors on trace gas retrievals, *J. Geophys. Res.—Atmos.*, *111*, D24204, doi:10.1029/2005JD006733.

Kyrölä, E., et al. (2004), GOMOS on Envisat: an overview, in *Climate Change Processes in the Stratosphere, Earth-Atmosphere-Ocean Systems, and Oceanographic Processes from Satellite Data*, edited by P. Schlussel, et al., pp. 1020−1028.

Kyrölä, E., et al. (2010), GOMOS O_3, NO_2, and NO_3 observations in 2002−2008, *Atmos. Chem. Phys.*, *10*, 7723-7738, doi:10.5194/acp-10-7723-2010.

Langlo, K. (1952), On the amount of atmospheric ozone and its relation to meteorological conditions, *Geofys. Publ.*, *18*, 1−42.

Lau, W. K. M., and D. E. Waliser (2011), *Intraseasonal Variability in the Atmosphere-Ocean Climate System*, 2nd ed., 646 pp., Springer-Verlag.

Lean, J. (2000), Evolution of the sun's spectral irradiance since the Maunder Minimum, *Geophys. Res. Lett.*, *27*, 2425−2428, doi:10.1029/2000GL000043.

Lean, J., and D. Rind (2001), Earth's response to a variable sun, *Science*, *292*, 234−236, doi:10.1126/science.1060082.

Lean, J., et al. (2005), SORCE contributions to new understanding of global change and solar variability, *Sol. Phys.*, *230*, 27−53, doi:10.1007/s11207-005-1527-2.

Lean, J. L., et al. (1997), Detection and parameterization of variations in solar mid- and near-ultraviolet radiation (200-400 nm), *J. Geophys. Res.—Atmos.*, *102*, 29939-29956, doi:10.1029/97JD02092.

Lean, J. L., and M. T. Deland (2012), How Does the Sun's Spectrum Vary?, *J. Clim.*, *25*, 2555−2560, doi:10.1175/JCLI-D-11-00571.1.

Lee, H., and A. K. Smith (2003), Simulation of the combined effects of solar cycle, quasi-biennial oscillation, and volcanic forcing on stratospheric ozone changes in recent decades, *J. Geophys. Res.—Atmos.*, *108*, 4049, doi:10.1029/2001JD001503.

Levelt, P. F., et al. (2006a), Science objectives of the Ozone Monitoring Instrument, *IEEE T. Geosci. Remote*, *44*, 1199−1208, doi:10.1109/tgrs.2006.872336.

Levelt, P. F., et al. (2006b), The Ozone Monitoring Instrument, *IEEE T. Geosci. Remote*, *44*, 1093−1101, doi:10.1109/TGRS.2006.872333.

Li, K.-F., et al. (2005), OH column abundance over Table Mountain Facility, California: AM−PM diurnal asymmetry, *Geophys Res Lett*, *32*, L13813, doi:10.1029/2005GL022521.

Li, K.-F., et al. (2012), Simulation of solar-cycle response in tropical total column ozone using SORCE irradiance, *Atmos. Chem. Phys. Discuss.*, *12*, 1867−1893, doi:10.5194/acpd-12-1867-2012.

Li, T., et al. (2008), Interannual variations of middle atmospheric temperature as measured by the JPL lidar at Mauna Loa Observatory, Hawaii (19.5 degrees N, 155.6 degrees W), *J. Geophys. Res.—Atmos.*, *113*, D14109, doi:10.1029/2007JD009764.

Lin, H., et al. (2009), An Observed Connection between the North Atlantic Oscillation and the Madden-Julian Oscillation, *J. Clim.*, *22*, 364−380, doi:10.1175/2008JCLI2515.1.

Lin, H., et al. (2010), Impact of the Madden-Julian Oscillation on the intraseasonal forecast skill of the North Atlantic Oscillation, *Geophys. Res. Lett.*, *37*, L19803, doi:10.1029/2010GL044315.

Liu, C. X., et al. (2009), A Madden-Julian Oscillation-triggered record ozone minimum over the Tibetan Plateau in December 2003 and its association with stratospheric "low-ozone pockets", *Geophys. Res. Lett.*, *36*, L15830, doi:10.1029/2009GL039025.

Livesey, N. J., et al. (2007), *EOS Aura MLS Version 2.2 Level 2 data quality and description document, Technical Report JPL D-33509*, Jet Propulsion Laboratory, downloadable from http://mls.jpl.nasa.gov/data/v2-2_data_quality_document.pdf.

Livesey, N. J., et al. (2008), Validation of Aura Microwave Limb Sounder O_3 and CO observations in the upper troposphere and lower stratosphere, *J. Geophys. Res.—Atmos.*, *113*, D15S02, doi:10.1029/2007JD008805.

Lovelock, J. E. (1971), Atmospheric Fluorine Compounds as Indicators of Air Movements, *Nature*, *230*, 379.

Machida, T., et al. (2008), Worldwide Measurements of Atmospheric CO_2 and Other Trace Gas Species Using Commercial Airlines, *J. Atmos. Ocean. Technol.*, *25*, 1744−1754, doi:10.1175/2008jtecha1082.1.

Madden, R. A., and P. R. Julian (1971), Detection of a 40−50 Day Oscillation in Zonal Wind in Tropical Pacific, *J. Atmos. Sci.*, *28*, 702−708.

Madden, R. A., and P. R. Julian (1972), Description of global-scale circulation cells in tropics with a 40−50 day period, *J. Atmos. Sci.*, *29*, 1109−1123.

Marsh, D. R., and R. R. Garcia (2007), Attribution of decadal variability in lower-stratospheric tropical ozone, *Geophys. Res. Lett.*, *34*, L21807, doi:10.1029/2007GL030935.

Marsh, D. R., et al. (2007), Modeling the whole atmosphere response to solar cycle changes in radiative and geomagnetic forcing, *J. Geophys. Res.—Atmos.*, *112*, D23306, doi:10.1029/2006JD008306.

Matsueda, H., et al. (2002), Aircraft observation of carbon dioxide at 8−13 km altitude over the western Pacific from 1993 to 1999, *Tellus Series B—Chemical and Physical Meteorology*, *54*, 1-21.

Matthes, K., et al. (2010), Role of the QBO in modulating the influence of the 11 year solar cycle on the atmosphere using constant forcings, *J. Geophys. Res.—Atmos.*, *115*, D18110, doi:10.1029/2009JD013020.

McCormack, J. P., et al. (2007), Solar-QBO interaction and its impact on stratospheric ozone in a zonally averaged photochemical transport model of the middle atmosphere, *J. Geophys. Res.—Atmos.*, *112,* D16109, doi:10.1029/2006JD008369.

McElroy, M. B., and R. J. Salawitch (1989), Changing Composition of the Global Stratosphere, *Science*, *243*, 763−770, doi:10.1126/science.243.4892.763.

Meehl, G. A., et al. (2009), Amplifying the Pacific Climate System Response to a Small 11-Year Solar Cycle Forcing, *Science*, *325*, 1114−1118, doi:10.1126/science.1172872.

Meetham, A. R. (1937), Correlation of amount of ozone with other characteristics of the atmosphere, *Q. J. Roy. Meteor. Soc.*, *63*, 289−307, doi:10.1002/qj.49706327102.

Merkel, A. W., et al. (2011), The impact of solar spectral irradiance variability on middle atmospheric ozone, *Geophys. Res. Lett.*, *38,* L13802, doi:10.1029/2011GL047561.

Mills, F. P., et al. (2002), OH column abundance over Table Mountain Facility, California: Annual average 1997−2000, *Geophys. Res. Lett.*, *29*, 1742, doi:10.1029/2001GL014151.

Mills, F. P., et al. (2003), OH column abundance over Table Mountain Facility, California: Intra-annual variations and comparisons to model predictions for 1997−2001, *J. Geophys. Res.—Atmos.*, *108,* 4785, doi:10.1029/2003JD003481.

Minschwaner, K., et al. (2003), Hydroxyl column abundance measurements: PEPSIOS instrumentation at the Fritz Peak Observatory and data analysis techniques, *J. Atmos. Sol. Terr. Phys.*, *65*, 335−344, doi:10.1016/S1364-6826(02)00297-3.

Morgenstern, O., et al. (2010), Review of the formulation of present-generation stratospheric chemistry-climate models and associated external forcings, *J. Geophys. Res.—Atmos.*, *115*, D00M02, doi:10.1029/2009JD013728.

Mori, M., and M. Watanabe (2008), Growth and triggering mechanisms of the PNA: A MJO-PNA coherence, *J. Meteor. Soc. Japan, 86*, 213−236, doi:10.2151/JMSJ.86.213.

Müller, R., and R. J. Salawitch (1999), Upper stratospheric processes, in *Scientific Assessment of Ozone Depletion: 1998, WMO Global Ozone Research and Monitoring*

Project—Report No. 44, edited, pp. 6.1–6.44, World Meteorological Organization, Geneva.

Newchurch, M. J., et al. (2003), Evidence for slowdown in stratospheric ozone loss: First stage of ozone recovery, *J. Geophys. Res.—Atmos., 108*, 4507, doi:10.1029/2003JD003471.

Newman, P. A., et al. (2006), When will the Antarctic ozone hole recover?, *Geophys. Res. Lett., 33,* L12814, doi:10.1029/2005GL025232.

Oman, L. D., et al. (2010), Multimodel assessment of the factors driving stratospheric ozone evolution over the 21st century, *J. Geophys. Res.—Atmos.*, *115*, D24306, doi:10.1029/2010JD014362.

Osterman, G. B., et al. (1997), Balloon-borne measurements of stratospheric radicals and their precursors: Implications for the production and loss of ozone, *Geophys Res Lett*, *24,* 1107−1110, doi:10.1029/97GL00921.

Pan, L. L., and T. Li (2008), Interactions between the tropical ISO and midlatitude low-frequency flow, *Clim. Dyn., 31*, 375−388, doi:10.1007/s00382-007-0272-7.

Pfister, C. (Ed.) (1995), *Monthly temperature and precipitation in central Europe 1529−1979: quantifying documentary evidence on weather and its effects*, 118−142 pp., Routledge, New York.

Pickett, H. M., and D. B. Peterson (1996), Comparison of measured stratospheric OH with prediction, *J Geophys Res-Atmos*, *101*, 16789−16796, doi:10.1029/96JD01168.

Pickett, H. M. (2006), Microwave Limb Sounder THz module on Aura, *IEEE T Geosci Remote Sensing*, *44*, 1122−1130, doi:10.1109/TGRS.2005.862667.

Pickett, H. M., et al. (2006), Observation of night OH in the mesosphere, *Geophys Res Lett*, *33*, L19808, doi:10.1029/2006GL026910.

Pickett, H. M., et al. (2008), Validation of Aura Microwave Limb Sounder OH and HO_2 measurements, *J Geophys Res.—Atmos*, *113*, D16S30, doi:10.1029/2007JD008775.

Poulin, L., and W. F. J. Evans (1994), METOZ: Total ozone from meteorological parameters, *Atmos.—Ocean, 32*, 285−297, doi:10.1080/07055900.1994.9649499.

Quay, P. D., et al. (1992), Oceanic Uptake of Fossil Fuel CO_2: Carbon-13 Evidence, *Science*, *256*, 74−79.

Randel, W. J., and J. B. Cobb (1994), Coherent variations of monthly mean total ozone and lower stratospheric temperature, *J. Geophys. Res.—Atmos.*, *99*, 5433−5447.

Randel, W. J., and F. Wu (2007), A stratospheric ozone profile data set for 1979−2005: Variability, trends, and comparisons with column ozone data, *J. Geophys. Res.—Atmos.*, *112,* D06313, doi:10.1029/2006JD007339.

Rayner, P. J., and D. M. O'Brien (2001), The utility of remotely sensed CO_2 concentration data in surface source inversions, *Geophys. Res. Lett.*, *28*, 175−178.

Reinsel, G. C., et al. (2005), Trend analysis of total ozone data for turnaround and dynamical contributions, *J. Geophys. Res.—Atmos.*, *110*, D16306, doi:10.1029/2004JD004662.

Remsberg, E. (2010), Observed seasonal to decadal scale responses in mesospheric water vapor, *J Geophys Res.—Atmos*, *115*, D06306, doi:10.1029/2009JD012904.

Richter, J. H., et al. (2010), Toward a Physically Based Gravity Wave Source Parameterization in a General Circulation Model, *J. Atmos. Sci.*, *67*, 136−156, doi:10.1175/2009JAS3112.1.

Rind, D., and J. Overpeck (1993), Hypothesized Causes of Decade-to-Century-Scale Climate Variability: Climate Model Results, *Quat. Sci. Rev.*, *12*, 357−374, doi:10.1016/s0277-3791(05)80002-2.

Rodgers, C. D. (2000), *Inverse Methods of Atmospheric Sounding: Theory and Practice*, 240 pp., World Scientific Publishing Company, Singapore.

Roundy, P. E., and L. M. Gribble-Verhagen (2010), Variations in the Flow of the Global Atmosphere Associated with a Composite Convectively Coupled Oceanic Kelvin Wave, *J. Clim.*, *23*, 4192−4201, doi:10.1175/2010JCLI3630.1.

Salawitch, R. J., et al. (2005), Sensitivity of ozone to bromine in the lower stratosphere, *Geophys Res Lett*, *32,* L05811, doi:10.1029/2004GL021504.

Salby, M., et al. (2011), Rebound of Antarctic ozone, *Geophys. Res. Lett.*, *38*, L09702, doi:10.1029/2011GL047266.

Sander, S. P., et al. (2006), *Chemical Kinetics and Photochemical Data for Use in Atmospheric Studies Evaluation No. 15, Tech Report JPL Publ 06-2,* Jet Propulsion Laboratory.

Sander, S. P., et al. (2011), *Chemical Kinetics and Photochemical Data for Use in Atmospheric Studies Evaluation No. 17, Tech Report JPL Publ 10-6,* Jet Propulsion Laboratory.

Sandor, B. J., and R. T. Clancy (1998), Mesospheric HO_x chemistry from diurnal microwave observations of HO_2, O_3, and H_2O, *J Geophys Res.—Atmos*, *103*, 13337−13351, doi:10.1029/98JD00432.

Scafetta, N., and R. C. Willson (2009), ACRIM-gap and TSI trend issue resolved using a surface magnetic flux TSI proxy model, *Geophys Res Lett*, *36*, L05701, doi:10.1029/2008GL036307.

Schmidt, H., et al. (2010), Solar cycle signal in a general circulation and chemistry model with internally generated quasi-biennial oscillation, *J. Geophys. Res.—Atmos.*, *115*, D00I14, doi:10.1029/2009JD012542.

Schwartz, M. J., et al. (2008), Validation of the Aura Microwave Limb Sounder Temperature and Geopotential Height Measurements, *J. Geophys. Res.*, *113*, D15S11, doi:10.1029/2007JD008783.

Seo, K. H., and S. W. Son (2012), The Global Atmospheric Circulation Response to Tropical Diabatic Heating Associated with the Madden-Julian Oscillation during Northern Winter, *J. Atmos. Sci.*, *69,* 79−96, doi:10.1175/2011JAS3686.1.

Sheppard, P. A. (1963), Atmospheric tracers and the study of the general circulation of the atmosphere, *Rep. Prog. Phys.*, *26*, 213-267, doi:10.1088/0034-4885/26/1/307.

Shindell, D., et al. (1999), Solar cycle variability, ozone, and climate, *Science*, *284*, 305−308, doi:10.1126/science.284.5412.305.

Snow, M., et al. (2005a), Solar-Stellar Irradiance Comparison Experiment II (SOLSTICE II): Examination of the solar-stellar comparison technique, *Sol Phys*, *230*, 295−324, doi:10.1007/s11207-005-8763-3.

Snow, M., et al. (2005b), The Mg II index from SORCE, *Sol. Phys.*, *230*, 325−344, doi:10.1007/s11207-005-6879-0.

Solomon, S., et al. (2010), Contributions of Stratospheric Water Vapor to Decadal Changes in the Rate of Global Warming, *Science*, *327*, 1219−1223, doi:10.1126/science.1182488.

Soukharev, B. E., and L. L. Hood (2006), Solar cycle variation of stratospheric ozone: Multiple regression analysis of long-term satellite data sets and comparisons with models, *J. Geophys. Res.—Atmos.*, *111*, D20314, doi:10.1029/2006JD007107.

Steinbrecht, W., et al. (1998), Correlations between tropopause height and total ozone: Implications for long-term changes, *J. Geophys. Res.—Atmos.*, *103*, 19183−19192, doi:10.1029/98JD01929.

Steinbrecht, W., et al. (2006), Long-term evolution of upper stratospheric ozone at selected stations of the Network for the Detection of Stratospheric Change (NDSC), *J Geophys Res.—Atmos*, *111*, D10308, doi:10.1029/2005JD006454.

Stolarski, R. S., et al. (1991), Total Ozone Trends Deduced from Nimbus 7 TOMS Data, *Geophys. Res. Lett.*, *18*, 1015−1018, doi:10.1029/91GL01302.

Stolarski, R. S., et al. (2006), Trends in stratospheric ozone: Lessons learned from a 3D chemical transport model, *J. Atmos. Sci.*, *63*, 1028−1041, doi:10.1175/JAS3650.1.

Stolarski, R. S., and S. M. Frith (2006), Search for evidence of trend slow-down in the long-term TOMS/SBUV total ozone data record: the importance of instrument drift uncertainty, *Atmos. Chem. Phys.*, *6*, 4057−4065.

Swartz, W. H., et al. (2012), Middle atmosphere response to different descriptions of the 11-yr solar cycle in spectral irradiance in a chemistry-climate model, *Atmos. Chem. Phys.*, *12*, 5937−5948, doi:10.5194/acp-12-5937-2012.

Tapping, K. F., and B. Detracey (1990), The Origin of the 10.7 cm Flux, *Sol. Phys.*, *127*, 321−332, doi:10.1007/BF00152171.

Thompson, A. M., et al. (2004), SHADOZ — A tropical ozonesonde-radiosonde network for the atmospheric community, *B. Am. Meteorol. Soc.*, *85*, 1549−1564, doi:10.1175/BAMS-85-10-1549.

Thompson, A. M., et al. (2007), Southern Hemisphere Additional Ozonesondes (SHADOZ) 1998-2004 tropical ozone climatology: 3. Instrumentation, station-to-station variability, and evaluation with simulated flight profiles, *J. Geophys. Res.—Atmos.*, *112*, D03304, doi:10.1029/2005JD007042.

Tian, B., et al. (2007), Intraseasonal variations of the tropical total ozone and their connection to the Madden-Julian oscillation, *Geophys. Res. Lett.*, *34*, L08704, doi:10.1029/2007GL029451.

Tian, B., et al. (2008), Does the Madden-Julian oscillation influence aerosol variability?, *J. Geophys. Res.—Atmos.*, *113*, D12215, doi:10.1029/2007JD009372.

Tian, B., et al. (2010), Vertical Moist Thermodynamic Structure of the Madden-Julian Oscillation in Atmospheric Infrared Sounder Retrievals: An Update and a Comparison to ECMWF Interim Re-Analysis, *Mon. Weather Rev.*, *138*, 4576−4582, doi:10.1175/2010MWR3486.1.

Tian, B., and D. E. Waliser (2011), Chemical and biological impacts, Chapter 18, in *Intraseasonal Variability of the Atmosphere-Ocean System*, edited by K.-M. Lau and D. E. Waliser, Springer, Heidelberg, Germany.

Tian, B., et al. (2011), Modulation of Atlantic aerosols by the Madden-Julian oscillation, *J. Geophys. Res.*, *116*, D15108, doi:10.1029/2010JD015201.

Tian, B. J., et al. (2006), Vertical moist thermodynamic structure and spatial-temporal evolution of the MJO in AIRS observations, *J. Atmos. Sci.*, *63*, 2462−2485.

Tourpali, K., et al. (2003), Stratospheric and tropospheric response to enhanced solar UV radiation: A model study, *Geophys. Res. Lett.*, *30*, 1231, doi:10.1029/2002GL016650.

Trenberth, K. E., and J. W. Hurrell (1994), Decadal atmosphere-ocean variations in the Pacific, *Clim. Dyn.*, *9*, 303−319, doi:10.1007/BF00204745.

Tung, K. K., and H. Yang (1988), Dynamic variability of column ozone, *J. Geophys. Res.—Atmos.*, *93*, 11123−11128, doi:10.1029/JD093iD09p11123.

van Loon, H., and K. Labitzke (1999), The signal of the 11-year solar cycle in the global stratosphere, *J. Atmos. Sol.—Terr. Phys.*, *61*, 53−61, doi:10.1016/s1364-6826(98)00116-3.

van Loon, H., et al. (2007), Coupled air-sea response to solar forcing in the Pacific region during northern winter, *J. Geophys. Res.—Atmos.*, *112*, D02108, doi:10.1029/2006JD007378.

Viereck, R. A., et al. (2004), A composite Mg II index spanning from 1978 to 2003, *Space Weather*, *2*, S10005, doi:10.1029/2004SW000084.

Vitart, F., and F. Molteni (2010), Simulation of the Madden-Julian Oscillation and its teleconnections in the ECMWF forecast system, *Q. J. Roy. Meteor. Soc.*, *136*, 842−855, doi:10.1002/qj.623.

von Neumann, J. (1955), Some remarks on the problem of forecasting climate fluctuations, in *Dynamics of Climate: The Proceedings of a Conference on the Application of Numerical Integration Techniques to the Problem of the General Circulation*, edited by R. L. Pfeffer, pp. 9−12, Pergamon Press.

Waliser, D., et al. (2009), MJO Simulation Diagnostics, *J. Clim.*, *22*, 3006−3030, doi:10.1175/2008jcli2731.1.

Waliser, D. E., et al. (2003), Potential predictability of the Madden-Julian oscillation, *B. Am. Meteorol. Soc.*, *84*, 33−50, doi:10.1175/bams-84-1-33.

Waliser, D. E., et al. (2005), Subseasonal organization of ocean chlorophyll: Prospects for prediction based on the Madden-Julian Oscillation, *Geophys. Res. Lett.*, *32*, L23602, doi:10.1029/2005GL024300.

Wang, B., and X. S. Xie (1998), Coupled modes of the warm pool climate system. Part 1: The role of air-sea interaction in maintaining Madden-Julian oscillation, *J. Clim.*, *11*, 2116−2135, doi:10.1175/1520-0442-11.8.2116.

Wang, J., et al. (2011), El Nino-Southern Oscillation in Tropical and Midlatitude Column Ozone, *J. Atmos. Sci.*, *68*, 1911−1921, doi:10.1175/JAS-D-11-045.1.

Wang, S., et al. (2008), Validation of Aura Microwave Limb Sounder OH measurements with Fourier Transform Ultra-Violet Spectrometer total OH column measurements at Table Mountain, California, *J Geophys Res.—Atmos*, *113*, D22301, doi:10.1029/2008JD009883.

Wang, S., et al. (2012), Atmospheric OH Response to the 11-year Solar Cycle - Could the gap between model and observations be filled by SORCE measurements?, *Proc. Nat. Acad. Sci.—USA, under review*.

Waters, J. W., et al. (2006), The Earth Observing System Microwave Limb Sounder (EOS MLS) on the Aura satellite, *IEEE T. Geosci. Remote*, *44*, 1075−1092, doi:10.1109/tgrs.2006.873771.

Weare, B. C. (2010), Madden-Julian Oscillation in the tropical stratosphere, *J. Geophys. Res.—Atmos.*, *115,* D17113, doi:10.1029/2009JD013748.

Weare, B. C., et al. (2012), Madden-Julian Oscillation in a climate model with a well-resolved stratosphere, *J. Geophys. Res.—Atmos.*, *117,* D01103, doi:10.1029/2011JD016247.

Weickmann, K., and E. Berry (2009), The Tropical Madden-Julian Oscillation and the Global Wind Oscillation, *Mon. Weather Rev.*, *137,* 1601−1614, doi:10.1175/2008MWR2686.1.

Wheeler, M. C., and H. H. Hendon (2004), An all-season real-time multivariate MJO index: Development of an index for monitoring and prediction, *Mon. Weather Rev.*, *132*, 1917−1932.

WMO (2003), *Scientific Assessment of Ozone Depletion: 2002, Global Ozone Research and Monitoring Project — Report No. 47,* 498 pp., World Meteorological Organization, Geneva.

WMO (2007), *Scientific Assessment of Ozone Depletion: 2006, Global Ozone Research and Monitoring Project — Report No. 50,* 572 pp., World Meteorological Organization, Geneva.

Wolter, K., and M. S. Timlin (2011), El Niño/Southern Oscillation behaviour since 1871 as diagnosed in an extended multivariate ENSO index (MEI.ext), *Intl. J. Climatology, 31*, 1074−1087, doi:10.1002/joc.2336.

Wong, S., and A. E. Dessler (2007), Regulation of H_2O and CO in tropical tropopause layer by the Madden-Julian oscillation, *J. Geophys. Res.-Atmos.*, *112*, D14305, doi:10.1029/2006JD007940.

Worden, H. M., et al. (2007), Comparisons of Tropospheric Emission Spectrometer (TES) ozone profiles to ozonesondes: Methods and initial results, *J. Geophys. Res.—Atmos.*, *112*, D03309, doi:10.1029/2006JD007258.

Worden, J., et al. (2004), Predicted errors of tropospheric emission spectrometer nadir retrievals from spectral window selection, *J. Geophys. Res.—Atmos.*, *109*, D09308, doi:10.1029/2004JD004522.

Yau, K. K. C. (1988), Analysis of pre-telescopic and telescopic sunspot observations, in *Secular Solar and Geomagnetic Variations in the Last 10,000 Years,* edited by F. R. Stephenson and A. W. Wolfendale, pp. 161−185, Springer, New York.

Zangvil, A. (1975), Temporal and spatial behavior of large-scale disturbances in tropical cloudiness deduced from satellite brightness data, *Mon. Weather Rev.*, *103,* 904−920, doi:10.1175/1520-0493(1975)103<0904:TASBOL>2.0.CO;2.Zhang, C., and M. Dong (2004), Seasonality in the Madden-Julian oscillation, *J. Clim.*, *17*, 3169−3180.

Zhang, C. D. (2005), Madden-Julian oscillation, *Rev. Geophys.*, *43*, RG2003, doi:10.1029/2004RG000158.

Zhou, J., and K.-K. Tung (2010), Solar Cycles in 150 Years of Global Sea Surface Temperature Data, *J. Clim.*, *23,* 3234−3248, doi:10.1175/2010JCLI3232.1.

Zhou, S. T., and A. J. Miller (2005), The interaction of the Madden-Julian oscillation and the arctic oscillation, *J. Clim.*, *18*, 143−159, doi:10.1175/JCLI3251.1.

Ziemke, J. R., and S. Chandra (2003), A Madden-Julian Oscillation in tropospheric ozone, *Geophys. Res. Lett.*, *30*, 2182, doi:10.1029/2003GL018523.